In presenting the dissertation as a partial fulfillment of the requirements for an advanced degree from the Georgia Institute of Technology, I agree that the Library of the Institute shall make it available for inspection and circulation in accordance with its regulations governing materials of this type. I agree that permission to copy from, or to publish from, this dissertation may be granted by the professor under whose direction it was written, or, in his absence, by the Dean of the Graduate Division when such copying or publication is solely for scholarly purposes and does not involve potential financial gain. It is understood that any copying from, or publication of, this dissertation which involves potential financial gain will not be allowed without written permission.

7/25/68

SCATTERING OF He^+ IONS BY NOBLE GASES AT HIGH ENERGIES

A THESIS

Presented to

The Faculty of the Graduate Division

by

George Ormsbee Taylor, Jr.

In Partial Fulfillment

of the Requirements for the Degree

Doctor of Philosophy

in the School of Physics

Georgia Institute of Technology

September, 1969

SCATTERING OF He^+ IONS BY NOBLE GASES

AT HIGH ENERGIES

Approved:

Chairman

Date approved by Chairman: 9/26/69

To my wife Fay,

my daughter Martha,

and my son Douglas.

ACKNOWLEDGMENTS

It is a pleasure to acknowledge the assistance of at least some of the many people who have contributed to the work described in this thesis. It is a great pleasure to express my gratitude to my thesis advisor, Dr. D. W. Martin, for his continued guidance and encouragement throughout this research. Also, I would like to express my sincere appreciation to Dr. E. W. Thomas for his untiring assistance during this work. This manuscript benefitted greatly from the careful reading of Dr. T. F. Moran.

It is a pleasure to acknowledge the assistance of Mr. J. W. Martin, Mr. G. N. Howell, Mr. F. T. Richey, Mr. J. C. Ford, Mr. B. W. Griffiths, and Mr. D. E. Troyer during various portions of the construction and operation of the equipment. I wish to express appreciation to Mr. J. D. Dameron, Mr. T. E. Harden, and Mr. V. B. Raynolds of the Mechanical Services Branch of the Engineering Experiment Station for their interest and excellent workmanship in constructing crucial parts of the apparatus. Appreciation is extended to Mr. O. B. Francis for writing a computer program for the calculation of the present data.

This work was supported by the Controlled Thermonuclear Research Program, Division of Research, U. S. Atomic Energy Commission. Finally, I wish to express my gratitude to the National Science Foundation for their fellowship support during the last year of this research.

TABLE OF CONTENTS

TABLE OF CONTENTS (Concluded)

LIST OF TABLES

LIST OF ILLUSTRATIONS

LIST OF ILLUSTRATIONS (Continued)

LIST OF ILLUSTRATIONS (Concluded)

ABSTRACT

The scattering of He^+ projectiles by impact on the noble gases, He, Ne, and Ar, was investigated in the energy range 120 to 830 keV under single collision conditions. Specifically, the experiment measured as a function of angle in the range one to eight degrees the total differential scattering cross section as well as the differential scattering cross sections for scattering without change of charge, for scattering with charge transfer, and for scattering with electron stripping. Also, the fraction of particles in a particular charge state was measured as a function of energy at fixed scattering angle.

A Van de Graaff accelerator furnished a monoenergetic beam of ions from 120 to 1000 keV. Two circular holes of diameter 0.025 inch collimated the beam entering the collision region, where the target gas pressure was typically one micron. Particles scattered through an angle θ were collimated by a two-slit geometry, whose angular resolution was approximately 10 minutes of arc, passed through a parallel plate electrostatic deflector for charge sorting, and counted individually with a silicon surface barrier detector. At the energies of the present experiment, this detector has an efficiency of 100 percent. The primary projectile beam in the collision chamber was monitored continuously by detecting the collisionally induced photon emission from the target with a photomultiplier. The photon emission was calibrated in terms of beam current by a preliminary experiment in which a Faraday cup was temporarily placed in the incident beam path through the collision chamber.

The sum of the differential cross sections for scattering He^{o}, He^{+}, and He^{2+} through an angle θ was equal to the measured total differential cross section. The absolute error associated with the total differential cross section is ± 23 percent, the random error is estimated to be ± 10 percent. This total differential cross section was found to equal the theoretical differential scattering cross section based on a classical calculation using a screened Coulomb type potential. Thus, the scattering of the particles in these close encounters is determined by the mutual nuclear repulsion and may be adequately described by classical mechanics. The four differential scattering curves were parallel over the angular range investigated, indicating that P_n, the fraction of particles in a particular charge state n, was independent of the scattering angle. This result is consistent with theory and with experiments performed at slightly lower energies.

There was excellent agreement for the energy dependence of P_n in all three target gases with data at lower energies. The random error in P_n is estimated to be ± 10 percent. For the resonant case He^{+} + He, it was found that P_o, the fraction of scattered particles which had picked up an electron during the collision, could be fitted in the investigated energy range by a semi-empirical equation if a damping factor in the equation was properly adjusted. Also, good agreement was found when comparing P_n with the predictions of a statistical theory.

CHAPTER I

INTRODUCTION

The investigation of differential scattering in atom collisions offers an excellent means of studying the connection between the electronic states of a diatomic system and its collision properties. For many years both experiments and theory focused attention primarily on total cross sections and ignored the details of angular distributions. However, more recently studies of differential scattering have revealed a great deal of interesting structure in the cross sections for various collisional processes which were previously unexpected and unsought.[1] Such studies have shown that many inelastic processes remain important down to surprisingly low energies, even close to threshold energies. The result of these developments is the beginning of a collisional spectroscopy of diatomic systems quite comparable to optical spectroscopy in richness of structure and variety of features that can be observed with similar potentialities for revealing information about the electronic structure and interactions of the transient molecular system formed during the collision.[1]

A theoretical task in the following years will be to develop understanding of these features and of the underlying principles in order that empirical evidence obtained from experiments can be converted into reliable information about interatomic potentials and other interaction parameters which can be used for a variety of predictive purposes. This

development of an empirical and phenomenological framework will be closely connected with the development of methods for a purely theoretical explanation.

One of the most striking measurements of differential scattering is contained in the studies of elastic collisions for He^+ ions with He, Ne, and Ar atoms at low energies (10 to 600 eV).[2,3] These data contain a surprising wealth of information which appears in the form of structure superimposed on the smoothly varying differential scattering cross sections. Structure measurement has also been observed in the differential scattering as a function of angle of heavy noble gas ions by noble gas atoms at an energy of 50 keV.[4] Other workers have reported structure in differential scattering cross section curves, but these studies have been primarily at low energies.[5,6,7]

The one feature which distinguishes the measurements just mentioned from earlier measurements of differential scattering cross sections (prior to 1960) is the fine angular resolution. This improvement was possible because of more sensitive and more stable detection systems.

The present measurements were undertaken to closely examine the scattering of a relatively simple system, the He^+ ion, in a high energy region. This work complements the low energy work of Lorents and Aberth,[2,3] and the two sets of data are linked through intermediate energies (10 to 200 keV) by the work of the group at the University of Connecticut.[8,9] The following reactions were investigated

$$\begin{aligned} He^+ + X &\rightarrow He^+ + [X] \\ &\rightarrow He^{2+} + [X + e] \\ &\rightarrow He^{\circ} + [X^+] \end{aligned}$$

where the target X was the noble gases He, Ne, and Ar. The charge state and the angle of scatter of the projectile were measured (in the range one to eight degrees) over the energy range from approximately 150 to 830 keV. The state of the target atom after the collision was unknown; thus, it was impossible to distinguish elastic from inelastic collisions even when the projectile did not change its charge state. The analysis of experimental data is complicated by contributions of inelastic processes; however, Firsov[10] has shown that classical ideas can be used to analyze inelastic scattering of primary ions whose energies are in the keV region if the ratio of the inelastic energy loss to the kinetic energy of the particle is small. Data from other laboratories[11,12] indicate this condition is clearly met in the present experiment.

The present work was undertaken to measure the differential scattering cross sections for He^+ ions in an energy and angular range hitherto not examined. The data show that, within the investigated range, the interaction potential can be approximated very well by a screened Coulomb potential of the form

$$U(r) = U_{coul}(r)\, e^{-r/c_B} \tag{1}$$

where $U_{coul}(r)$ is the Coulomb potential, r is the separation of the two nuclei, and c_B is the screening length.

$$c_B = \frac{a_o}{[Z_1^{2/3} + Z_2^{2/3}]^{\frac{1}{2}}} \tag{2}$$

where a_o is the Bohr radius. This potential, equation (1), has been dis-

cussed by Bohr,[13] who suggested the screening length, c_B. For the present experiment

$$c_B = 2.975 \times 10^{-9} \text{ cm for an He target}$$

$$c_B = 2.124 \times 10^{-9} \text{ cm for an Ne target}$$

$$c_B = 1.823 \times 10^{-9} \text{ cm for an Ar target}$$

The differential scattering curves were closely examined for structure superimposed on the smoothly varying cross section curves. Structure was not observed in the measured cross sections, and an upper bound was placed on the magnitude of any structure existing in the investigated range.

In the present experiment the fraction P_n of the total scattered projectiles in each particular charge state + ne, where e is the electron charge, was measured as a function of energy and scattering angle. These fractions were found to be independent of the scattering angle over the entire energy range investigated, a result which is consistent with earlier work at lower energies of Fuls, et al.[8] Ziemba, et al.,[9] have measured the charge state fractions as a function of energy to 150 keV at fixed angle for the same projectile-target combinations as investigated in the present experiment. The present data agree very well with these earlier measurements.

The fraction of the total beam undergoing charge transfer (the charge transfer probability) has shown a very interesting oscillation for the resonant case $He^+ + He$ when plotted as a function of energy (between approximately 10 and 200 keV) at fixed scattering angle.[8] This oscillatory behavior has been explained, in part, by the theoretical work of Bates and McCarroll.[14] The present measurements agree very well

in the investigated energy region with a semi-empirical relation suggested by Everhart[15] if the damping factor is appropriately chosen. The physical origin of such a damping effect is discussed both by Lichten[16] and by Marchi and Smith.[17]

Other general features for all target gases in the P_n versus energy curves are discussed in terms of the statistical theory advanced by Russek.[18,19] This phenomenological theory gives good agreement with experiment even though the theory is based on assumptions of doubtful validity.

In this thesis the fundamental concepts of a two body collision at high energies are discussed. The true differential scattering cross section is defined and its relation with the measured differential scattering cross section developed. Relevant portions of classical and quantum mechanical scattering theory are also presented.

A brief resumé of other closely related experiments is given. Here the practical limitations of the other experiments are considered, thus providing a basis for comparison of the apparatus and techniques of the present experiment.

The mechanical construction of the apparatus, the tests which were performed to evaluate this equipment, and the methods and techniques used to accumulate the data are then discussed. Also, the errors associated with this work are considered.

The results of these measurements are presented in graphical form, in comparison with other experiments and with available theories.

CHAPTER II

BASIC CONCEPTS OF HIGH ENERGY TWO BODY COLLISIONS

Heavy particle collisions in which the projectile has an energy of hundreds of keV and where the scattering is through an angle of one degree or more have very small impact parameters. The deflection of the projectile is dominated primarily by the interaction between the two nuclei. The potential energy function of this interaction closely approximates a shielded Coulomb form. The final charge state of the scattered particle, on the other hand, depends largely on the interaction of the electrons and is reasonably independent of forces which control the nuclear scattering.[20]

Differential scattering cross sections measured in the hundreds of keV energy region can be compared with theoretical differential scattering cross sections evaluated from classical theory with the Coulomb force between the nuclei modified by a factor due to the electron screening. Classical theories, however, are unable to make predictions about the effect of charge changing processes on the scattered beam. Predictions concerning the fractions of the scattered beam in particular charge states employ either quantum mechanical approximations or use a statistical approach.

Recently, structure has been observed on the smoothly varying differential scattering cross section[2,3,4] (as predicted by a Coulomb type potential) when plotted as a function of angle. One explanation

of this structure presents a molecular complex picture of the collision,[1] while an alternate explanation that has been advanced is the concept of collective oscillations in the electron shells.[21] The molecular complex picture has been much more successful in explaining experimental data and will be considered below.

This chapter gives a background for the comparison of the experimental results with theory. A true differential scattering cross section will be defined and its relation to the measured differential scattering cross section developed. The measured differential scattering cross section is measured in the laboratory-fixed reference frame, whereas theoretical treatments are always developed in the center-of-mass reference frame. To connect these two different reference frames, the kinematical transformations between them are given. Then classical scattering theory will be discussed. The validity of the classical approach is considered, followed by a brief description of classical scattering where the question of extracting information about interaction potentials will be discussed. The final section of this chapter will outline the theoretical approaches which have been advanced to explain the distribution of charge states of the scattered particles.

Definition of Differential Scattering Cross Section

The discussion of this section follows the work of Thomas[22] and of Filippenko.[23] Begin by considering a single particle traveling along the x axis incident on a target of density N_t. Assume that there are sufficiently few targets, so that the projectile is scattered only once.

The probability of scatter into the infinitesimal solid angle

$d\omega = \sin\theta\, d\theta\, d\chi$, while traversing the infinitesimal path length dx is

$$P = \frac{d\sigma}{d\omega}(\theta,\chi)\, N_t\, d\omega\, dx \ . \tag{3}$$

$\frac{d\sigma}{d\omega}(\theta,\chi)$ is a proportionality constant having the dimensions of area per particle steradian and is defined to be the true differential scattering cross section. It depends on the scattering angles (θ,χ) illustrated in Figure 1.

Let the beam of projectiles have a volume density N_p, and each particle a velocity v. The infinitesimal cross sectional area of the projectile beam is dA. The number of projectiles scattered per unit time into the infinitesimal solid angle, $d\omega$, from the "point volume," dxdA will be

$$d\eta(\theta,\chi) = (vN_p dA)\, P = vN_p N_t \frac{d\sigma}{d\omega}(\theta,\chi)\, d\omega dA dx \ . \tag{4}$$

Experiments measure the particles scattered into a finite solid angle. Let dN be the number of particles per second scattered into the finite solid angle, ω, from the infinitesimal "point volume element," dxdA

$$dN(\theta,\chi) = \int_\omega d\eta(\theta,\chi) = vN_p N_t dA dx \int_\omega \frac{d\sigma}{d\omega}(\theta,\chi)\, d\omega \ . \tag{5}$$

To proceed further assume that $\frac{d\sigma}{d\omega}$ varies smoothly and slowly over the finite solid angle ω. Make the approximation

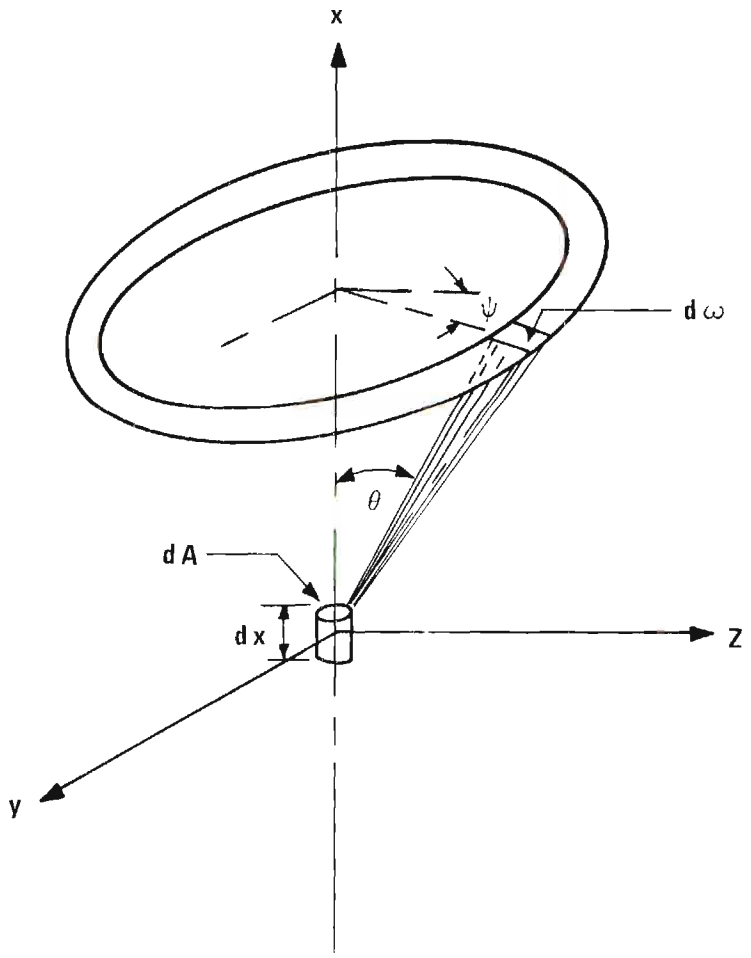

Figure 1. Scattering Geometry for Infinitesimal Element of Incident Beam.

$$\int \frac{d\sigma}{d\omega}\, d\omega \approx \overline{\frac{d\sigma}{d\omega}}\,(\theta,\chi)\ \omega\ . \tag{6}$$

$\overline{\frac{d\sigma}{d\omega}}\,(\theta,\chi)$ is the mean differential scattering cross section over the solid angle ω. This approximation has the effect of smearing the scattering angle (θ,χ); contributions to $\overline{\frac{d\sigma}{d\omega}}$ now are received from θ to $\theta+\Delta\theta$, χ to $\chi+\Delta\chi$. This gives not only an average differential scattering cross section but also an average scattering angle which will be observed by the notation $(\bar{\theta},\bar{\chi})$.

This assumption (henceforth referred to as Approximation I) is the fundamental limit in attempting to deduce differential scattering cross sections from experimental data. It is especially bad at very small scattering angles where there is quite rapid variation of the scattering cross section with angle. (The scattering here is still from a "point volume.")

Using this approximation, equation (5) becomes

$$dN(\bar{\theta},\bar{\chi}) = vN_pN_t\,dAdx\ \overline{\frac{d\sigma}{d\omega}}\,(\bar{\theta},\bar{\chi})\ \omega\ . \tag{7}$$

In reality the detection system views a finite volume of beam, $\iint dAdx$, and the particles actually entering the detection system per second are

$$N(\bar{\theta},\bar{\chi}) = \iint dN = vN_pN_t \iint \overline{\frac{d\sigma}{d\omega}}\,(\bar{\theta},\bar{\chi})\ \omega\, dAdx\ . \tag{8}$$

Next, make the approximation (Approximation II)

$$\iint \overline{\frac{d\sigma}{d\omega}}\,(\bar{\theta},\bar{\chi})\;\omega\,dA\,dx \approx \overline{\overline{\frac{d\sigma}{d\omega}\,(\bar{\theta},\bar{\chi})}} \iint \omega\,dA\,dx \quad . \tag{9}$$

The effect of this approximation is twofold. It tends to smooth out variations in the cross section and also to smear (to a greater extent than the first approximation) the definition of the angle $(\bar{\theta},\bar{\chi})$. Both approximations become particularly bad at small angles.

To consider the effect of these approximations, take two points along the beam axis, $x=x_1$ and $x=x_2$, so located with respect to the slits defining the scattered beam that these points satisfy the requirement $\omega(x_1) = \omega(x_2)$. Such a pair of points is shown in Figure 2. Then, from equation (5) (dropping both Approximations I and II for the moment)

$$dN_{x=x_1}(\theta,\chi) = \text{const.} \int_{\omega} \frac{d\sigma}{d\omega}\,(\theta,\chi)\;d\omega \quad , \tag{10a}$$

and

$$dN_{x=x_2}(\theta,\chi) = \text{const.} \int_{\omega} \frac{d\sigma}{d\omega}\,(\theta,\chi)\;d\omega \quad . \tag{10b}$$

Although the regions of integration are of identical size in these cases, the integrands are different; θ for point x_1 is smaller than θ for point x_2. Hence, contributions to the scattered beam from a "point volume," and thus contributions to the total scattered beam $N = \iint dN$, depend not only on the magnitude of the solid angle but also on the point on the axis from which the scattering takes place.

Actually,

$$N = \iint dN = \text{const.} \iiint \frac{d\sigma}{d\omega}\,d\omega\,dA\,dx \quad .$$

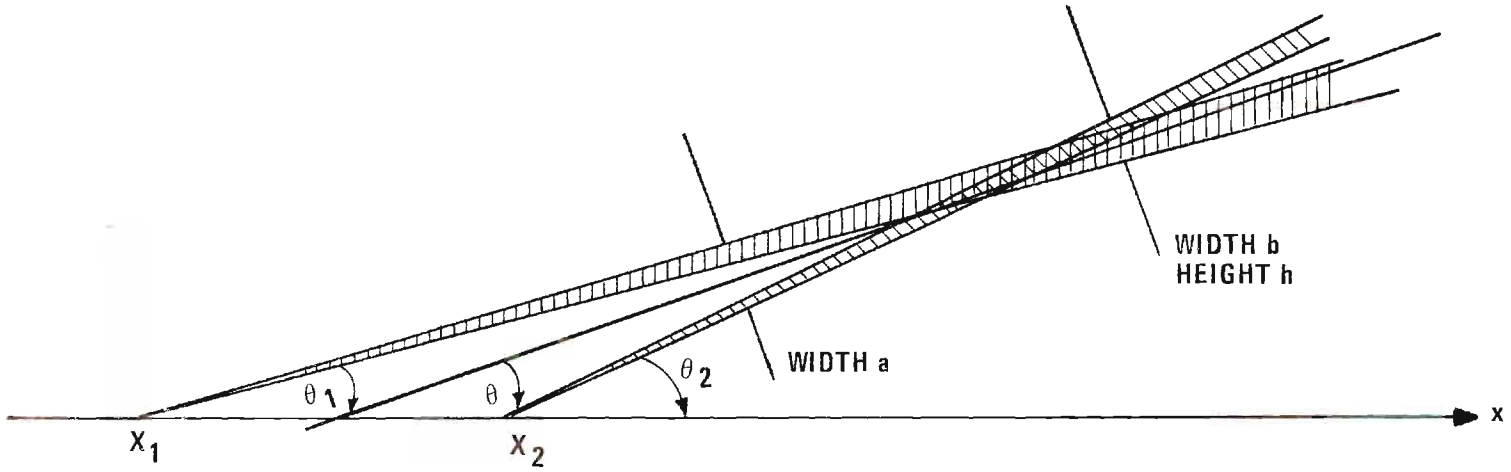

Figure 2. Two Points Which Satisfy the Condition $\omega(x_1) = \omega(x_2)$.

Approximation I relaxes the first integration giving

$$N = \text{const.} \iint \overline{\frac{d\sigma}{d\omega}}\, \omega dA dx \ ,$$

while the second approximation allows the scattering cross section to be taken outside the volume integral.

Applying these approximations, equation (8) becomes

$$N(\bar{\theta},\bar{\chi}) = vN_p N_t \overline{\overline{\frac{d\sigma}{d\omega}}\,(\bar{\theta},\bar{\chi})} \iint \omega dA dx \ . \tag{11}$$

$N(\bar{\theta},\bar{\chi})$ is the number of particles per unit time scattered into the angle $(\bar{\theta},\bar{\chi})$. vN_pA represents the number of projectiles per unit time. Let $N_o = vN_pA$ be the total intensity of the incident beam.

$$N(\bar{\theta},\bar{\chi}) = \frac{N_o}{A} N_t \overline{\overline{\frac{d\sigma}{d\omega}}\,(\bar{\theta},\bar{\chi})} \int \omega dA dx \ . \tag{12}$$

Rearranging equation (12)

$$\overline{\overline{\frac{d\sigma}{d\omega}}\,(\bar{\theta},\bar{\chi})} = \frac{N(\bar{\theta},\bar{\chi})}{N_o} \frac{1}{N_t} \frac{1}{\frac{1}{A}\int \omega dA dx} \ . \tag{13}$$

In Appendix A it is shown that, under most circumstances,

$$\int \omega dA dx \approx A \int \omega dx$$

is a very good approximation. Thus,

$$\overline{\frac{d\sigma}{d\omega}(\bar{\theta},\bar{\chi})} = \frac{N(\bar{\theta},\bar{\chi})}{N_o}\,\frac{1}{N_t}\,\frac{1}{\int \omega dx}\,. \tag{14}$$

This is the equation which is used to evaluate an experimental value for the differential scattering cross section.

In a scattering experiment a beam of projectiles (the beam having a finite, but small, cross sectional area) is scattered by a target gas of low density at room temperature. If these particles have an axis, they are randomly oriented, and the experiment averages over any resulting azimuthal dependence, producing axial symmetry (see Figure 1). This experiment, as do most scattering experiments, moves the detector only in the x-o-z plane which holds χ constant, $\chi=0$ (ignoring the uncertainty in χ due to previous approximations). Therefore, the χ dependence will no longer be explicitly shown.

To simplify the notation which is used, the following changes will be made:

$$\overline{\frac{d\sigma}{d\omega}(\bar{\theta},\bar{\chi})} = \frac{d\sigma}{d\omega}(\theta)\ ;$$

$$N(\bar{\theta},\bar{\chi}) = N(\theta)\ .$$

Hereafter, $\frac{d\sigma}{d\omega}(\theta)$ will refer to the measured differential scattering cross section. Thus,

$$\frac{d\sigma^n}{d\omega}(\theta) = \frac{N^n(\theta)}{N_o}\,\frac{1}{N_t}\,\frac{1}{G(\theta)} \tag{15}$$

where

$$G(\theta) = \int \omega dx$$

is the geometrical factor discussed in Appendix A.

The superscript n denotes the charge state of the scattered particles and also the corresponding differential scattering cross section.

Equation (15) is a quantity that may be measured experimentally. $\frac{d\sigma}{d\omega}(\theta)$ is the measured differential scattering cross section and is dependent upon the scattering apparatus; the relation of this measured to true differential scattering cross section is primarily dependent on two approximations stated in equations (6) and (9). Without exception the errors associated with making these approximations become large at small θ, so that it is in this region that the largest discrepancy between the measured and the true differential scattering cross sections are to be found. The present measurements are in the angular range from approximately one to eight degrees, and in this range the approximations are not bad. Therefore, the measured is essentially equal to the true differential scattering cross section.

The total differential scattering cross section, $\frac{d\sigma^T}{d\omega}(\theta)$ is the sum of the differential scattering cross section for electron capture, $\frac{d\sigma^0}{d\omega}(\theta)$, for electron stripping, $\frac{d\sigma^{2+}}{d\omega}(\theta)$, and for scattering without change of charge, $\frac{d\sigma^+}{d\omega}(\theta)$.

$$\frac{d\sigma^T}{d\omega}(\theta) = \frac{d\sigma^0}{d\omega}(\theta) + \frac{d\sigma^{2+}}{d\omega}(\theta) + \frac{d\sigma^+}{d\omega}(\theta) \qquad (16)$$

Another important quantity in the present experiment is the fraction of the scattered beam in a particular charge state. P_n represents the fraction of the scattered particles in charge state n.

$$P_n = \frac{\frac{d\sigma^n}{d\omega}(\theta)}{\frac{d\sigma^T}{d\omega}(\theta)} = \frac{N^n(\theta)}{N^T(\theta)} \tag{17}$$

Coordinate Transformation

The experimental value for the differential scattering cross section as measured in laboratory coordinates is given by equation (15). The theoretically predicted differential scattering cross section, $\frac{d\sigma}{d\Omega}(\Theta)$, is in the center of mass (C.M.) reference frame. Θ is the scattering angle, and $d\Omega$ is the element of solid angle in the center of mass frame. The reasons for using the C.M. reference frame will be discussed in the next section of this chapter.

The same number of projectiles must be scattered into a given element of solid angle $d\omega$ in the laboratory as are scattered into the corresponding element of solid angle $d\Omega$ in the C.M. system.

$$\frac{d\sigma}{d\omega}(\theta)\, d\omega = \frac{d\sigma}{d\Omega}(\Theta)\, d\Omega$$

or

$$\frac{d\sigma}{d\omega}(\theta) = \frac{d\Omega}{d\omega}\frac{d\sigma}{d\Omega}(\Theta) \ . \tag{18}$$

The ratio of corresponding solid angles is given by[24]

$$\frac{d\Omega}{d\omega} = \frac{[\gamma'^2 + 2\gamma' \cos\Theta + 1]^{3/2}}{1 + \gamma' \cos\Theta} \ , \tag{19}$$

where

$$\gamma' = \gamma\sqrt{\frac{E_{cm}}{E_{cm} - Q}} \tag{20}$$

and

$\gamma = m/M$. m is the mass of the projectile; M is the mass of the target. E_{cm} is the energy associated with the relative motion in the center of mass reference frame.

$$E_{cm} = \frac{E_{lab}}{1 + \gamma} \tag{21}$$

Q is the inelastic energy loss.

Equation (18) transforms the cross sections, but it is also necessary to transform the angle appropriate for the transformed cross section. This transformation equation is given by

$$\tan\theta = \frac{\sin \Theta}{\gamma' + \cos \Theta} . \tag{22}$$

The ratio Q/E is very small, so that $\gamma' \simeq \gamma$ is a very good approximation. The value of Q/E is discussed below. Hence, using this approximation, equations (18) and (22) perform the necessary transformation to compare theoretical and experimental differential scattering cross sections.

Equations (18) and (19) are correct only for infinitesimal solid angles $d\omega$ and $d\Omega$. No difficulty arises in the use of these equations if the theoretical differential scattering cross section, $\frac{d\sigma}{d\Omega}(\Theta)$ is transformed into the laboratory frame of reference and comparisons between theory and experiment are made in laboratory coordinates. However, additional errors, much like those discussed in the previous section, are introduced if this transformation is used to take the experimentally measured cross section $\frac{d\sigma}{d\omega}(\theta)$ to the C.M. frame for comparison. All com-

parisons of the present measurements are made in laboratory coordinates.

Validity of Classical Scattering

The interaction between two atoms during a collision can be approximately represented by the potential energy function,

$$U(r) = \frac{Z_1 Z_2 e^2}{r} e^{-r/c_B} . \tag{23}$$

The first factor is the Coulomb potential energy function between two nuclei of charges $Z_1 e$ and $Z_2 e$. The exponential factor modifies the Coulomb potential function to allow for the electron screening. (This equation, as well as all equations presented will utilize the c.g.s. system of units.) Bohr[13] has discussed this potential function in detail and suggested a screening length (based on an estimate of the charge distribution within the atom by an appropriate statistical procedure such as developed by Thomas[28] and Fermi[29]).

$$c_B = \frac{a_o}{[Z_1^{2/3} + Z_2^{2/3}]^{\frac{1}{2}}} \tag{2}$$

where a_o is the radius of the first orbit in hydrogen, 0.53×10^{-8} cm. The potential function, equation (23), will henceforth be referred to as the Bohr potential.

Many authors[25,26,27] have discussed the validity of classical theory in describing the differential scattering cross section. The general results of these considerations give two conditions that must be satisfied for classical theory to adequately describe the differential

scattering cross section. These conditions are (1) the de Broglie wavelength, λ, of the projectile must be negligible when compared with any significant dimension of the scattering center, and (2) the collision must be well defined within the limits of the uncertainty principle.

The first condition requires that

$$\lambda \ll c$$

or

$$\lambda \ll D$$

where c is the screening length and D the collision diameter.

The collision diameter is the distance of closest approach which is energetically possible and is given by

$$D = \frac{Z_1 Z_2 e^2}{\frac{1}{2} m_r v^2} \tag{24}$$

where m_r is the reduced mass. ($m_r = \frac{mM}{m + M}$, m is the mass of the projectile, and M is the mass of the target.) D is considered to be a good measure of the effective size of the scattering center if D/c is small.

The second condition may be restated in a different form, namely, that the deflection of the projectile must not be obscured by the spread of the wave packet. Bohr[13] has shown that, for the screened potential, equation (23), the lower limit of the scattering angle for the validity of classical mechanics is

$$\Theta^* \simeq \frac{\lambda}{2\pi c_B}$$

Applied to the circumstances of the present experiment (He^+ + Ar at 400 keV); $\lambda = 2.3 \times 10^{-12}$ cm, $c_B = 1.8 \times 10^{-9}$ cm, $D = 13.6 \times 10^{-12}$ cm,

and $D/c_B = 0.0075$. $\Theta^* = 0.12$ degrees while the smallest angle in the measurements was approximately 0.8 degrees. Thus, these conditions are satisfied, and it is reasonable to expect classical theory to adequately describe the scattering. This expectation is verified by the data of this experiment.

Although no general quantum mechanical solution has been worked out for the potential function of equation (23), the solution in the Born approximation for this potential is known.[13,30] When the appropriate validity criteria are examined,[13,25] a very interesting fact emerges;[26] namely, the solution for particles heavier than electrons is valid only for angles less than Θ^*. Since the classical solution is valid for angles greater than this limit, the two methods are valid in mutually exclusive angular ranges.[26]

Classical Scattering

The following resumé of classical scattering theory follows the discussion found in many texts.[27,31,32] Consider a narrow beam of particles (each of mass m and traveling with a velocity v in the x direction) incident on a single target of mass M which is initially stationary. It is well known[31] that, if this problem is formulated in the center of mass (C.M.) reference frame, the relative motion of the projectile-target combination is equivalent to the motion of a single particle of reduced mass, m_r, acted on by a fixed scattering center. Furthermore, so long as only a central force field is considered, the scattering lies in a plane.[32]

The angle of scatter for each projectile is determined uniquely by energy and angular momentum of the particle.[31] The impact parameter,

b, defined as the perpendicular distance between the scattering center and the incident velocity (see Figure 3) is directly related to the angular momentum. Thus, the scattering angle, Θ, is determined once the energy and the impact parameter of the particle are known. The scattering angle is given by the equation[32]

$$\Theta = \pi - 2 \int_{r_o}^{\infty} \frac{dr}{\Phi(r)} \tag{25}$$

where

$$\Phi(r) = \sqrt{\frac{r^2}{b^2}\left[1 - \frac{U(r)}{E_{cm}}\right] - 1} \quad . \tag{26}$$

r is the magnitude of the vector describing the position of the projectile relative to the scattering center; r_o is the distance of closest approach (the largest real root of $\Phi(r) = 0$); $U(r)$ is the interaction potential (assumed to be a central potential only); and E_{cm} is the C.M. energy of the collision. Θ is the scattering angle of both m and M in the center of mass reference frame.

If N_o' is the number of projectiles per cm^2 per second, then $N_o'(2\pi bdb)$ will be the number of projectiles that are incident on the scattering center with impact parameter in the range b to b + db. After scattering, these particles will travel in the angular range Θ to $\Theta + d\Theta$ with respect to the direction of the incident beam; the number scattered per second into this angular ring will be

$$N_o'(2\pi \sin \Theta \, d\Theta) \frac{d\sigma}{d\Omega}(\Theta) \quad .$$

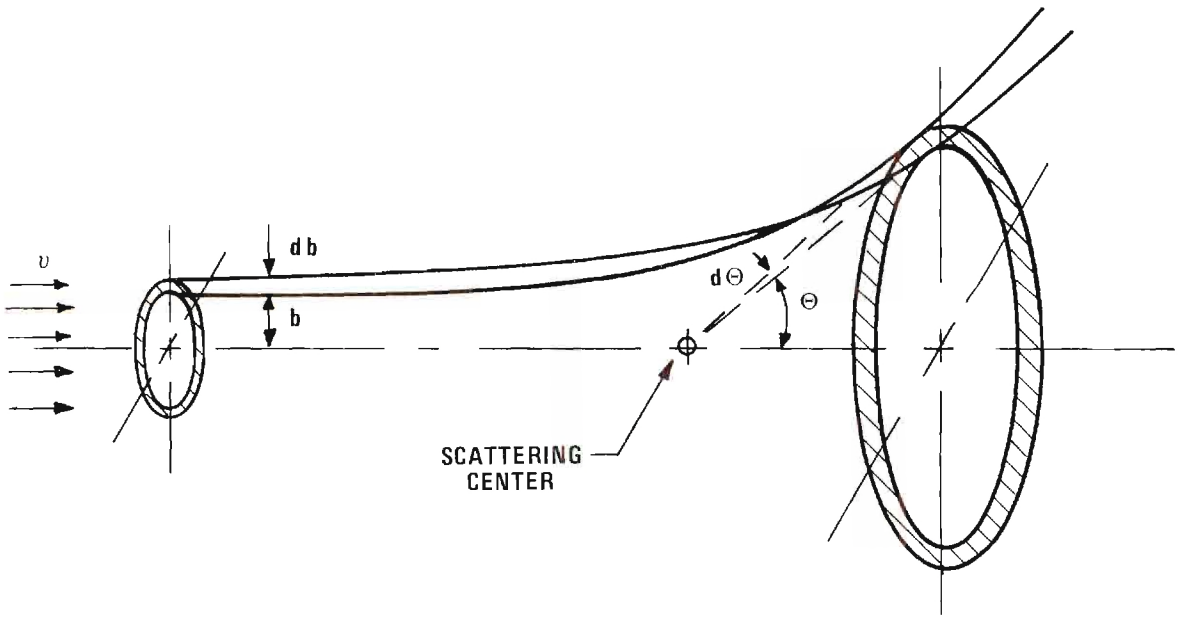

Figure 3. Scattering of Projectile by Center of Force.

$\frac{d\sigma}{d\Omega}(\Theta)$ is a quantity having the dimensions of area per steradian; it is the differential cross section for elastic scattering in the C.M. frame of reference. Figure 3 illustrates this situation. Thus,

$$|N_o'(2\pi b db)| = |N_o'(2\pi \sin\Theta\, d\Theta)\frac{d\sigma}{d\Omega}(\Theta)|$$

or

$$\frac{d\sigma}{d\Omega}(\Theta) = \frac{b}{\sin\Theta}\left|\frac{db}{d\Theta}\right| . \tag{27}$$

The impact parameter, b, is a function of the energy and the scattering angle related through equations (25) and (26), $b = b(\Theta, E_{cm})$. In general, $b(\Theta, E_{cm})$ cannot be expressed in an analytic form; however, numerical solutions for the impact parameter are possible.

The total scattering cross section is given by

$$\sigma(\Theta) = \int_o^{\pi} 2\pi \frac{d\sigma}{d\Omega}(\Theta) \sin\Theta\, d\Theta \tag{28}$$

where it is assumed there is no azimuthal dependence.

Differential scattering cross sections provide information about the interaction potential, for it is this potential energy function that is responsible for the scattering. Basically, there are two ways to deduce the potential function from the measured cross section. One is to compare directly the measured values with calculations from arbitrarily assumed potential functions. The second is to deduce the potential energy function from the measured value.

Firsov[33] has shown how the potential (assuming a spherically symmetric function) can be deduced from differential scattering data at

fixed energy. This technique consists of two steps. First, the differential scattering cross section data are used to find the angular dependence of the impact parameter. The next step is to find the potential energy as a function of the separation distance. This technique has been applied to experimental data.[34]

F. Smith[35] points out that, if experimental data were absolutely accurate and extended over the full angular range from 0 to π at a fixed energy, no ambiguity would exist in extracting the potential by the Firsov method. However, experimental limitations place a boundary on the angular range, the resolution, and the accuracy of measurements. Hence, F. Smith[35] developed a single inversion technique to extract the potential function which combined data over a wide range of energy and angle. With this method it is, in principle, possible to estimate the potential function numerically, but Smith[20] states that, due to scatter in data, the procedure is somewhat ambiguous. He found it more profitable to fit curves using simple, physically plausible, potential functions.

In the present experiment the impact parameter was very small so that the first estimate of the interaction potential giving rise to the scattering force between the projectile and the target is simply the Coulomb potential between the bare nuclei. The Coulomb potential is

$$U(r) = \frac{Z_1 Z_2 e^2}{r} . \qquad (29)$$

Upon substitution of this potential into equations (25) and (27), the classical Rutherford scattering cross section is obtained.

$$\frac{d\sigma}{d\Omega}(\Theta) = \left(\frac{D}{4}\right)^2 \frac{1}{\sin^4\left(\frac{\Theta}{2}\right)} \tag{30}$$

D, the collision diameter, was previously discussed. Also, from the $\Phi(r)$ equation a relation for the distance of closest approach can be obtained.

$$r_o = \frac{D}{2}\left(1 + \frac{1}{\sin\frac{\Theta}{2}}\right) \tag{31}$$

The effect of the screening of the nuclei by the orbital electrons has been ignored. Several ways have been suggested to include this effect. One of the simplest is to consider the Bohr potential function mentioned above.

$$U(r) = \frac{Z_1 Z_2 e^2}{r} e^{-r/c_B} \tag{23}$$

The exponential factor modifies the pure Coulomb potential to simulate the effect of the electron screening. The extent of the electron screening is measured by c_B, the screening length, given by equation (2). The differential scattering cross section for this screened potential energy function has been numerically calculated and presented in tabular form.[26,36] Also, these calculations have been compared with experimental results.[8,37]

O. B. Firsov[38] has made calculations with another potential function

$$U(r) = \frac{Z_1 Z_2 e^2}{r} \chi\left(\left[Z_1^{2/3} + Z_2^{2/3}\right]^{\frac{1}{2}} \frac{r}{a}\right) \tag{32}$$

where χ is the Fermi-Thomas shielding function.[39]

Both the Bohr and the Firsov potentials have shown good agreement with experimental work.[34] Lindhart, et al.[40] have considered the scattering by several types of potentials--the two potentials just discussed as well as a Lenz-Jensen potential and a power law potential. The effect of these potential functions is to modify the pure Coulomb potential to simulate the effect of electron screening. At high impact velocities, i.e., very close distances of approach, the screening effect introduced in each of these potentials reduces to the "pure" Coulomb potential. The entire development (regardless of the potential function used) is for elastic collisions. However, the present experiment does not, in fact cannot, truly distinguish elastic from inelastic events.

Subsidiary measurements, to be described in Chapter IV, with the present equipment indicate the average inelastic energy loss, Q (at any fixed scattering angle in the present range), to be small. These particular observations were not very sensitive and could only set an upper limit on Q of less than 15 percent of the incident energy. More direct measurements[11,12] of the inelastic energy loss in high energy heavy particle collisions show Q/E to be actually less than 0.01. Therefore, since the inelastic energy loss is such a small percentage of the projectile energy, it is reasonable to compare the measured total differential scattering cross section with the theoretical cross section based on elastic scattering. Firsov[10] has shown the validity of such consideration, and Smith[20] refers to such high energy scattering, where Q/E is very small, as quasielastic scattering.

As seen in equation (27) the impact parameter, b, is closely re-

lated to the differential scattering cross sections. While the impact parameter is not directly measured (see equation (15)), it is closely related to observables. In the semi-classical limit[1]

$$b \simeq b(\Theta, E_{cm}, Q)$$
$$\Theta \simeq \Theta(b, E_{cm}, Q) .$$

In recent years such relations have been used to analyze experimental data in order to correlate various observed processes with particular impact parameters.[1] However, it has been necessary to assume a potential energy function to obtain the connection between b and Θ.

Certain expansions have been developed which have proven very valuable in the comparison and analysis of experiments.[35] These are

$$\tau \equiv E_{cm}\, \Theta(b, E_{cm}) = \tau_0(b) + \frac{1}{E_{cm}} \tau_1(b) + \frac{1}{E_{cm}^2} \tau_2(b) + \ldots \quad (33)$$

and a reduced cross section

$$\rho \equiv \Theta \sin\Theta \frac{d\sigma}{d\Omega} (\Theta, E_{cm}) = \rho_0(\tau) + \Theta\rho_1(\tau) + \Theta^2\rho_2(\tau) + \ldots \quad (34)$$

Smith[35] suggests plotting experimental data in terms of ρ versus τ. In such graphs small angle scattering data can be effectively compared over wide spans of energy.[20] Also, particular features occurring in a limited range of τ can be recognized as being associated with a given impact parameter and distance of closest approach, even if the actual values of these distances are not known.

Charge Changing Theories

Investigations of the scattering of He^+ ions on various noble gas targets have discovered very interesting oscillatory behavior.[8,41] This behavior, which is most pronounced in the resonant case, $He^+ + He$, has been observed in the energy range from 0.4 to 200 keV. At low energies ($\approx$ 1 keV) the oscillatory behavior also exhibits an angular dependence, but the oscillation becomes independent of scattering angle (if $\theta \geq 4°$) above 25 keV.

This oscillatory behavior was exhibited in the following manner.[42] The scattered particles were observed at a fixed angle, under single collision conditions. The fraction of the He^+ ions which was neutralized by electron capture varied with the energy of the projectile, showing pronounced maxima at certain energies. A most interesting feature was that the maxima are equally spaced when P_o was plotted against the reciprocal of the velocity.[42]

These oscillations in the electron capture probability can be interpreted by means of the following qualitative picture.[15] As the $He^+ + He$ system collides, it is assumed that the system can be described by the normalized sum of only two wave functions of He_2^+. These are χ_g and χ_u, functions of even and odd symmetry, respectively. The energies associated with these states are E_g and E_u. The "instantaneous-time dependencies" of these states are different, being exp - $(iE_g t/\hbar)$ and exp - $(iE_u t/\hbar)$. During the collision these wave functions get in and out of phase with an "instantaneous-beat frequency" $(E_g - E_u/h)$ which is a function of internuclear separation r. The beat frequency increases as the particles approach, reaches a maximum as they pass close to one another, and then decreases as they re-

cede. Since χ_g is even and χ_u is odd, it is evident in adding them that the extra electron is on one side of the molecule when the two are in phase and on the other side when they are out of phase. Thus, the occurrence of charge transfer depends on whether the collision time is an integral or half-integral number of "instantaneous-beat frequency" periods.

The impact parameter method (I.P.M.) has been used to put the above qualitative discussion on a more formal basis being used, with various extensions, to explain charge transfer data.[15,42,43] The relevant portions of the I.P.M. will be outlined as it applies to the resonant $He^+ + He$ case. Structure definitely appears in the non-resonant cases,[8] and the same general theoretical scheme is applicable,[43] with suitable modifications.

The impact parameter method assumes that the nuclei move in classical orbits, and quantal perturbation theory is applied to determine the transition probability from one electron state to another.[43] Further, it is assumed (for the symmetrical case $He^+ + He$) that only two states of He_2^+ are needed to describe the system;[43] excitation to other states is ignored. Also, the adiabatic assumption has been made that the electron wave functions at any instant are the same as they would be if the two nuclei were stationary at the same internuclear distance, r.[15] This last assumption has been modified both by Lichten[16] and by Bates and McCarroll.[14]

From these approximations it has been shown that[14]

$$P_o = \sin^2 \left\{ \pi \frac{J(r_o)}{h} - \pi \beta(v, r_o) \right\} \qquad (35)$$

where

$$J(r_o) = 2 \int_{r_o}^{\infty} (E_g - E_u) \frac{r}{\sqrt{r^2 - r_o^2}} \, dr \, , \tag{36}$$

and $(E_g - E_u)$ is the energy difference between the adiabatic symmetric and antisymmetric states of the molecule, He_2^+. $\beta(v, r_o)$ is a phase term which changes slowly compared to the first term.

Equation (35) has the same form as developed initially by Bates, et al.[44] and used by Ziemba and Russek[43] in discussing $He^+ + He$ data, the principal difference being the term, β. β is a phase correction which arises in taking account of the transitional energy of the active electron. At low energies, theory predicts that β approaches zero, in which case equation (35) reduces to exactly the same form as developed earlier.[44]

The energy difference has been approximated by[15]

$$E_g - E_u = A \, e^{-r/\kappa} \tag{37}$$

with A = 130 eV and κ = 0.422Å. (This expression is valid for $He^+ + He$.) It is obtained from the molecular state curves of Lichten[16] or numerically from calculations by Phillipson.[45] Substituting equation (37) into (36), the integration can be performed analytically yielding

$$J(r_o) = A \, r_o \, K_1 \left(\frac{r_o}{\kappa} \right) \tag{38}$$

where K_1 is the first-order modified Bessel function of the second kind.

At higher energies[43]

$$r_o K_1 \left(\frac{r_o}{K}\right) \simeq K$$

Since the angular dependence of P_o is contained in $J(r_o)$, this last statement shows that, at high energies, the probability of charge exchange is independent of scattering angle and a function of energy only. This assertion agrees with the present data (Figures 33 and 37), not only for the resonant case of $He^+ + He$, but also for the non-resonant cases. This angular independence was observed also by Ziemba, et al.[9] when using He^+ projectiles at 25 keV with $\theta \geq 4°$.

Experimental data can be represented closely by the semi-empirical equation[42]

$$P_o = K_o\left(\frac{1}{v}\right) + K_2\left(\frac{1}{v}\right) \sin^2 \left[\frac{\pi \langle E' a \rangle}{vh} - \beta\right] \qquad (39)$$

where K_o and K_2 are slowly varying functions of the reciprocal velocity. E' is the interaction energy associated with the oscillation, and (a) is the distance over which the collision occurs. K_2 is a damping function whose origin has been discussed by different authors.[16,17] Notice that if $K_o = 0$ and $K_2 = 1$, equation (39) has the same form as equation (35).

Lichten[16] proposes that damping arises in the deviation from adiabatic behavior which leads to a breakdown of the two-state approximation. It is proposed, based on the uncertainty principle, that the total wave function for the system must include a mixture of electronic states lying in a band very close to the states involved. The effect of mixing additional states destroys the interference, thus damping the oscillations. Marchi and Smith[17] propose a different reason for the damping, showing

that a two-state theory, even when properly formulated, would show a damping effect as a result of the interference of two scattering amplitudes that have different magnitudes at the scattering angle.

The values of $\langle E'a \rangle$ and β are determined empirically from a plot of reciprocal velocity versus P_o.[42] The period T of one cycle of electronic oscillation is

$$T = \frac{a}{v_{n+2}} - \frac{a}{v_n} = \frac{h}{E'}$$

where v_n and v_{n+2} are velocities of the projectile at the n^{th} and $(n+2)^{th}$ maxima of the reciprocal velocity versus P_o curve. It was assumed that this period could be set equal to Plank's constant, h, divided by the interaction energy, E', associated with the oscillation.

$$\langle E'a \rangle_n = \frac{h}{\frac{1}{v_{n+2}} - \frac{1}{v_n}} .$$

$\langle E'a \rangle$ can be determined experimentally in this manner. Since neither E' nor (a) are precise concepts, the brackets indicate an effective value of this quantity. Certainly the collision begins and ends gradually so that a fixed (a) is an over-simplification; also, the interaction energy varies with nuclear separation. For the case He^+ + He, Lockwood and Everhart[42] find that values $\langle E'a \rangle$ = 102 eV·Å and $\beta = 0.23\pi$ fit their low energy experimental results with K_2 = constant. Figure 38 shows that this equation fits the present data between 150 and 1000 keV very well if $K_2 \neq 1$, but rather $K_2 = 1.729 \times 10^8/v$ when v is the projectile velocity in cm/sec.

Further extensions of the I.P.M. treatment center around the determination of the energy difference $(E_g - E_u)$. The adiabatic representation has been used by many authors with the impact parameter method, but it is necessary to modify the adiabatic hypothesis in the neighborhood of an avoided crossing of the potential energy curves by making a particular linear combination of two adiabatic states. This method is satisfactory, but it is unclear how to construct the basic linear combinations in general situations where several states may be interacting.[16] Lichten has suggested the use of diabatic states which can be approximately described by molecular orbital considerations. These diabatic states which are constructed from a set of molecular orbital wave functions,[16] have the property of running smoothly through crossing points.

Lichten[46] has given a theoretical interpretation of inelastic atomic collisions. This work rests on two basic assumptions: molecular states can be used in the analysis of atomic collisions, and electrons are emitted from discrete states of the system. The agreement between this model and experiment in details of energy loss, fast electron spectra, and positions of critical internuclear distances is most impressive.[46] F. T. Smith[47] recently reexamined the equations of the general Born-Oppenheimer model for molecular problems. These results, which he refers to as the standard diabatic representation, have the properties called for in the work of Lichten.

As the projectile energy increases ($\approx$ 1 MeV), the recoil velocities of the nuclei become large compared with electronic velocities. Under these conditions, i.e., when the collision time is short compared with electron orbit time, the large momentum transfer between the nuclei is

not transmitted to the electrons, and the nuclei will become stripped of all electrons,[16] emerging from the collision fully ionized. The present measurements show that this condition is approached by the scattered projectile as seen in Figures 38 through 40. Under these conditions one would expect some high energy approximation (such as the Born approximation) to adequately describe the electron stripping process. While the Born approximation calculations have been applied to total cross sections, the results of the approximation for differential scattering cross sections have not been published; hence, comparisons between experiment and theory cannot be made at present.

A purely statistical theory was advanced several years ago by Russek.[18,19] This theory assumed that as the ion and atom collide a relatively small amount of kinetic energy of relative motion is transferred to the electrons. This energy is assumed to be distributed statistically among the outer-shell electrons, and the probability that any given number of electrons acquire more than the ionization energy is computed by statistical analysis. This ionization mechanism is analogous to the evaporation of molecules from a heated liquid.

This theory was initially designed for heavy particle interaction and gives good agreement with experiment in predicting both the height of intersections ($P_n \times P_m$) and of the peaks (P_n) of the ionization probability curves.[9,37] Further approximations, which were more difficult to justify,[48] were necessary to connect the probability curves with the angle of scatter. The statistical theory has been extended to apply to cases where any number of electrons (from 2 to 8) are contained in the outer shell.[19] In Chapter V, this theory is compared with data from the

present experiment. The agreement between theory and experiment can be seen in Table 9.

This statistical model as originally proposed is inconsistent with the shell structure of atoms and the discrete, sharp nature of autoionizing states. The statistical aspects of the theory have been improved and made more comprehensive,[49] such that the theory is now consistent with the concept of autoionizing transitions.[50,51]

CHAPTER III

SCATTERING EXPERIMENTS AT HIGH ENERGIES

The first experimental measurements of differential scattering cross sections in the high energy range for atomic ions incident on atoms were performed in 1954 and 1955 by Fedorenko[52] and by Everhart.*[53] After initial studies of differential scattering, these groups subsequently pursued somewhat different types of investigations. Fedorenko[54] turned generally to total cross section measurements, whereas Everhart[9] measured primarily electron capture and stripping associated with large angle scattering. (It is interesting that these two groups after following their different routes would perform coincidence experiments at almost the same time.[11,55])

In the mid-sixties Pivovar*[37,56-58] measured differential scattering cross sections for heavy ion-atom collisions. This work ranged to considerably higher energies than other measurements.

Measurements with which Fedorenko was associated, but not as the principal investigator, have more recently been conducted by V. V. Afrosimov.[4,21,59] This work was undertaken to confirm a proposed model explaining results from coincidence experiments.[21] These differential scattering cross sections show very interesting behavior.[4,21,59]

The work of these four groups constitutes the experimental data on differential scattering cross sections in the keV energy range. However,

---

*In the present chapter the groups will be referred to by the name of the principal investigator, e.g., Fedorenko's group and Everhart's group.

it is necessary to mention the results of one other research team, Lorents and Aberth,[2,3] for their results at lower energies gave impetus to the present investigation. Gilbody[60,61] has also made important contributions to the study of scattering of atomic systems; however, his work will not be discussed because it is not directly connected to the present measurements.

Lorents and Aberth[2,3] measured the elastic differential scattering cross section for He^+ on He, Ne, and Ar from 20 to 600 eV. In their very careful investigation a great deal of structure was discovered in the cross section curves which provided many new insights into the various mechanisms controlling the scattering. With the appearance of these results, reexamination of earlier work (i.e., that of Fedorenko and of Everhart) showed that similar structure in the cross section curves could have been completely missed, due to the limited angular resolution that was possible at the time of these early measurements. In fact, V. V. Afrosimov has detected structure in a careful reexamination of the total differential scattering in heavy noble ion-noble gas collisions at 25 and 50 keV.[4,12,59] One purpose in undertaking the present measurements was to see if similar structure could be found in the cross section curves at high keV energies for He^+ projectiles.

Several technological advances now make it possible to measure the differential scattering cross sections with much higher resolution than was possible in 1955. It is the purpose of this chapter to present a resumé of the experimental conditions and limitations in the differential scattering cross sections which have been measured to date. This resumé will provide a background against which to compare the experimental con-

ditions of the present measurements, as well as a framework of the data that have been accumulated to the present time.

As shown in Chapter II, the experimental differential scattering cross section is given by

$$\frac{d\sigma^n}{d\omega}(\theta) = \frac{N^n(\theta)}{N_o} \frac{1}{N_t} \frac{1}{G(\theta)} \tag{15}$$

where $\frac{N^n(\theta)}{N_o}$ is the ratio of scattered beam of charge state n to the incident beam in the collision region, N_t is the target density, and $G(\theta)$ is the geometrical factor. These three factors plus the scattering angle, θ, must be measured to determine the differential scattering cross section. The charge state of the scattered particles must also be measured to determine the scattering cross sections for electron capture or electron stripping. The methods employed in the measurement of these quantities will play the dominant role in the following discussion of the measurements of Fedorenko, Everhart, Pivovar, and Afrosimov.

Previous Experiments

N. V. Fedorenko[52,62,63]

The work of this group is covered in three papers which are summarized in Table 1. This work concentrates on the scattering of noble gas ions and alkali ions by noble gas atoms from five to 150 keV. The measurements provide an overall view of a large amount of information; i.e., they present a broad outline of data on scattering.

Following are specific points about this group of measurements.

1. The scattered particles were measured as a current into a

Table 1. Experimental Work of N. V. Fedorenko's Group (Differential Scattering Cross Sections Were Measured)

Title, Reference, Date	Cases Examined	Energy Range (keV)	Angular Range (°)	Angular Resolution (°)	Comments
"Single Scattering of Positive Ions in a Gas" [52] (1954)	Many cases investigated but only a few reported. Examples: (1) Scatter without change of charge $\left.\begin{matrix}He^+\\Kr^+\\Na^+\\I^+\end{matrix}\right\} + \left\{\begin{matrix}Ne\\Kr\end{matrix}\right\}$ (2) Stripping $Ar^+ + (\ ) \rightarrow Ar^{2+}$ (3) Dissociation $H_2^+ + (\ ) \rightarrow H^+$	5-30; most work at 10	$2\frac{1}{2}$-15	≈ 2.2	Deflected ions were magnetically analyzed. Measured currents with Faraday cup. Pressure measured with radiometric manometer. $\frac{d\sigma}{d\omega}$ may be in error by a factor of 2; but random error 10-15%.
"Single Scattering of Stripped Argon Ions" [62] (1955)	$Ar^+ + Ar \rightarrow Ar^{0-5+}$ $Ar^+ + \left\{\begin{matrix}He\\Ne\\Kr\end{matrix}\right\} \rightarrow Ar^{4+}$	40-150; most work at 75 with Ar target	0-15	≈ 0.5	Working pressure $\simeq 2 \times 10^{-4}$ Torr. Data had ~ ± 10% reproducibility. Systematic error in θ ± 1°. Calculated integral cross section from measurements.

Table 1. Experimental Work of N. V. Fedorenko's Group (Differential Scattering Cross Sections Were Measured)(Concluded)

Title, Reference, Date	Cases Examined	Energy Range (keV)	Angular Range (°)	Angular Resolution (°)	Comments
"Scattering of Multiply Charged Ions and Electron Capture" [63] (1960)	$Kr^{+,2+,3+}$ + {Ne, Kr} → $Kr^{0,+}$; Ne^{2+} + {Ne, Kr} → $Ne^{0,+}$	33	0-2.5	≈ 0.5	Error of ≃ ± 20-25%. This represents reproducibility of results. The angular range was $0.5° \leqq \theta \leqq 2.5°$ without charge exchange, $0 \leqq \theta \leqq 2°$ with charge exchange.

Faraday cup with an electrometer. This technique limits the minimum measurable scattered current to values greater than $(10)^{-14}$ amperes, which in turn limited the accessible angular range. (The cross sections in general decrease rapidly with increasing angle.)

2. The limitations of the current measuring techniques also required the slit dimension be relatively large, which, in turn, decreased the angular resolution.

3. The scattered beam was magnetically analyzed. This introduction of a magnetic field near the scattering chamber could have led to a distortion of the angular distribution, particularly at low energies. Everhart[64] notices general agreement in magnitude of his results for the differential cross sections (as a function of angle) with those of Fedorenko, but a disagreement on the slope of the curves.

4. The incident beam current could not be measured simultaneously with the scattered current when $\theta < 10°$. Therefore, these currents had to be measured sequentially most of the time. Since it is the ratio of these currents that is needed, the experimenter is forced to assume constancy of the beam current while measuring scattered current if only sequential measurements are made. As is well known, this can be a very dangerous assumption. (This comment about sequential rather than simultaneous current measurements is common to the work of all four groups.)

5. The random error in the measurements was 10 to 15 percent, but the absolute differential scattering cross sections could have been in error by a factor of two.

E. Everhart[8,53,64]

The work of this group represents the most systematic body of data

considered. After the original measurement of total differential scattering cross sections, the apparatus was continually modified and improved as different phenomena were investigated. The measurements all seem to originate from the same basic stem -- large angle scattering of single collisions. These papers form a very comprehensive set; it is almost like reading the log of one long continuous experiment rather than many separate works. Table 2 lists the pertinent facts concerning the experiments that measured differential scattering cross sections.

Many further experiments followed those listed in Table 2. While much of this work (reporting charge state fractions in the scattered beam) is relevant to the present investigation, it does not involve substantial changes in those aspects of the experimental techniques discussed here.

General comments about this work follow.

1. A Faraday cup was initially used to detect the scattered current; this was supplemented later by a secondary electron detector which was used for single particle detection. First, a thermal detector, then later the secondary electron detector, was used to detect the neutral beam.

2. The angular definition was continually improved, being approximately 2.3° initially but improving to ± 0.5° in the last paper in Table 2.

3. The scattered currents were electrostatically analyzed.

4. The beam current was measured sequentially with scattered current.

5. A McLeod gauge was used to measure the pressure.

6. The absolute accuracy was stated to be 30 to 50 percent; vary-

Table 2. Experimental Work of E. Everhart's Group (Measurements Include Both the Differential Scattering Cross Sections and P_n)

Title, Reference, Date	Cases Examined	Energy Range (keV)	Angular Range (°)	Angular Resolution (°)	Comments
"Differential Cross-Section Measurements for Large-Angle Collisions of Helium, Neon, and Argon Atoms at Energies to 100 keV" [53] (1955)	He^+, Ne^+, Ar^+ + Ar	25, 50, 100	$4\frac{1}{2}$-38	≈ 2.3	Scattered current measured with Faraday cup--no charge analysis. Pressure measured with McLeod gauge. Accuracy of measurement ± 30%. Compared data to Rutherford cross section.
"Charge Analysis and Differential Cross Section Measurements for Large-Angle Argon Ion-Argon Atom Collisions with Energies between 25 and 138 keV" [64] (1956)	Ar^+ + Ar He^+ + Ar	Several energies between 25 and 138	4-20	± 0.5	Scattered beam electrostatically analyzed. Used (i) Faraday cup, (ii) secondary electron multiplier, and (iii) thermal detector to measure scattered current. Relative value on $\frac{d\sigma}{d\omega}$ ± 20%. Absolute error on $\frac{d\sigma}{d\omega}$ ± 50%.

Table 2. Experimental Work of E. Everhart's Group (Measurements Include Both the Differential Scattering Cross Sections and P_n)(Concluded)

Title, Reference, Date	Cases Examined	Energy Range (keV)	Angular Range (°)	Angular Resolution (°)	Comments
					Error in P_n data ± 10%. Compare Ar^+ scattering with screened Coulomb potential; He^+ scattering with Coulomb potential.
"Measurements of Large-Angle Single Collisions between Helium, Neon, and Argon Atoms at Energies to 100 keV" [8] (1957)	$He^+ + \{He, Ne, Ar\}$; $Ne^+ + \{Ne, Ar\}$; $Ar^+ + Ar$	25, 50, 100	4-40	± 0.5	Improved accuracy of $\frac{d\sigma}{d\omega}$ by: (i) measuring beam current in collision chamber with a Faraday cup, (ii) improving scattering geometry. Compare He^+ data with Rutherford scattering. Compares data with Fedorenko[16]--agreement as to magnitude, but some difference on slope.

ing with the particular reported work; the relative accuracy was much better than this. The error in P_n was ± 10 percent.

7. The scattering cross sections all compared well with theoretical predictions which used a screened Coulomb type potential (a Bohr potential). The scattering of He^+ ions was compared with calculations based on a simple Coulomb potential.

L. I. Pivovar[37,56-58]

This series of papers, Table 3, concentrated on the scattering of heavy ions (Ar^+ and Kr^+) by noble gases heavier than He. The total differential scattering cross sections were reported. These measurements were differential in energy at a fixed scattering angle; they were not measured as a function of scattering angle.

As the energy dependence of these cross sections was given at only three different angles, it is possible to compare these measurements with other reported work at only three points. This fact was unfortunate; it would have been very interesting to see if structure exists in the differential scattering cross sections at the high energies of this set of experiments, since structure has been reported at 50 keV in the differential scattering cross section curves as a function of angle for some of the same projectile-target combinations.[21]

In this work Pivovar also measured the fraction of the scattered projectiles in each particular charge state. These data compare very well with the statistical theory of Russek.[18] The data do not show the definite plateaus and "breaks" as exhibited by the data of Afrosimov which are discussed below. (Pivovar and Afrosimov do not measure exactly the same thing; Pivovar plots P_n as a function of energy--250 to 1400 keV--

Table 3. Experimental Work of L. I. Pivovar's Group (Measurements Include Both Differential Scattering Cross Sections and P_n)

Title, Reference, Date	Cases Examined	Energy Range (keV)	Angular Range (°)	Angular Resolution (°)	Comments
"Differential Scattering Cross Section and Charge State Distribution of an Argon-Ion Beam in Single Collisions with Gas Atoms at 250-1400 keV" [37] (1963)	Ar^+ + Ar + Kr	250-1400	1,2,3 Does not measure as function of angle	Divergence of scattered beam 0.5	Electrostatic separation of charge state. Measured scattered currents with Faraday cups. Pressure measured with ionization gauge calibrated against McLeod gauge. P_o negligible even at 1°.
"Differential and Integral Cross Sections for the Loss and Capture of Electrons by Singly Charged Ions at 250-1400 keV Energies" [56] (1964)	Ar^+ + Ar + Kr	250-1400	0-3	Divergence of scattered beam 0.5	Measures differential scattering cross section at 1°,2°,3° as in [37]; opened slits to count all ions 0-1°.
"Deep 'Stripping' and Scattering of Kr^+ Ions in Single Collisions with Ne, Ar, Kr, and Xe Atoms" [57] (1966)	Kr^+ + {Ne, Ar, Kr, Xe}	250-850	0-3	Divergence of scattered beam 0.5	Measured charge state n = 12+. Random error in differential scat-

Table 3. Experimental Work of L. I. Pivovar's Group (Measurements Include Both Differential Scattering Cross Sections and P_n)(Concluded)

Title, Reference, Date	Cases Examined	Energy Range (keV)	Angular Range (°)	Angular Resolution (°)	Comments
					tering cross section ≈ 25%. Differential scattering cross section agrees well with screened Coulomb potential.
"Differential and Integral Cross Sections for the Loss and Capture of Electrons by Fast N^+, Ne^+, and Ar^+ Ions" [58] (1966)	N^+, Ne^+, Ar^+ + Ne, Ar, Kr, Xe	250-1400; some data to 1800	0-3	Divergence of scattered beam 0.5	

at three fixed angles, whereas Afrosimov shows P_n as a function of angle--five to 40 degrees--at a fixed energy, 25 keV.)

Specific comments on the experimental apparatus of Pivovar follow.

1. Scattered currents were measured with a Faraday cup. Previous comments about this technique are equally applicable here.

2. The scattered particle current was electrostatically analyzed.

3. The scattered particle current and beam current were measured sequentially.

4. Pressure was measured with an ionization gauge which was in turn calibrated against a McLeod gauge.

5. Pivovar estimates that his random error in differential cross section measurement was approximately 25 percent. His data agree with theoretical curves based on a screened Coulomb potential. No estimate is given of his absolute error.

V. V. Afrosimov[4,21,59]

Afrosimov measured the differential scattering cross section for several noble ion-atom combinations. This work is summarized in Table 4. A number of deviations from smooth curves were found (when the differential cross sections were plotted as a function of angle) which appear in the form of bumps superimposed on the smooth curve. The existence of this structure was used to support the concept of collective oscillations in the electron shells which had been advanced to explain coincidence data.[21,65]

These data are presented to supplement other work, and they suffer badly in this role because the experimental conditions were not specifiec and must be inferred. Specific comments follow.

1. The particle detection system is unknown; however, it is

Table 4. Experimental Work of V. V. Afrosimov's Group (Differential Scattering Cross Sections Were Measured)

Title, Reference, Date	Cases Examined	Energy Range (keV)	Angular Range (°)	Angular Resolution (°)	Comments
"Ionization and Scattering with Characteristic Energy Losses in Atomic Collisions" [4, 21] (1965)	Ar^+ + Ne Ar^+ + Ar Kr^+ + Kr	25, 50	4-25	1	Gives NO direct information on experimental apparatus. Implied that angular resolution ≈ 1°. Daly type counting system used for particle detection. Shows graph, $d\sigma/d\omega$ for Kr^+ + Kr at 50 keV; deviates from screened Coulomb curve in form of bumps superimposed on smooth curve; deviations ≈ 10-30%. Concludes from curve: "Form of $d\sigma/d\omega$ curves give grounds for assuming that the real interaction potential is not a continuous function of the shortest distance (of approach), and apparently changes abruptly on going from the excitation of one characteristic line to the excitation of another."
"Peculiarities of Scattering in Violent Collisions of Atomic Particles [59] (1967)	ions + atoms of noble gases. Specific cases: Kr^+ + Xe Kr^+ + Kr	25, 50	5-40	≈ 1/6	Kr^+ + Kr most pronounced irregularity.

believed that it was probably a Daly-type device such as was used in the coincidence work.[55] A Daly-type detector is suitable for single-particle counting.

2. The angular resolution in the initial measurements was improved to 10 minutes in subsequent work.

3. The separate charge states were not analyzed in the measurement of the differential scattering cross section curves. However, the fraction of charge states was analyzed as a function of angle in at least one case. The charge states were magnetically analyzed.

4. The method of measurement of the incident beam was not specified.

5. The method of measuring the target gas pressure was also not mentioned.

6. The error in these measurements was not stated.

In this work, projectile-target combinations were examined that had been measured earlier by both Fedorenko and Everhart. It is not surprising that the structure found had not been seen previously. Improved angular resolution and detector efficiency made possible the observation of the features reported by Afrosimov. It is regrettable that these data have not been reported in a more thorough manner.

Present Experiment

Prior to the present measurements, total differential scattering cross sections as a function of scattering angle have been measured at fixed energies up to 100 keV for He^+ projectiles. The angular resolution in these measurements was approximately one degree. Total differential scattering cross sections have been measured as a function of energy to

1400 keV at fixed scattering angles. Also, total differential scattering cross sections have been measured as a function of scattering angle at fixed energies to 50 keV with fine angular resolution; however, these extensions have been made only in heavy noble gas ions-atom collisions.

The present work measures the total differential scattering cross section (also the differential scattering cross section for electron capture, electron stripping, and scattering without change of charge) as a function of scattering angle at several specific energies between 150 and 830 keV with an angular resolution of approximately 10 minutes. Additionally, the probability of electron capture and electron stripping at fixed angles for He^+ ions was measured from approximately 150 to 830 keV. (These probabilities had been previously reported from 10 to 200 keV.) Thus, the present measurements fill a gap in the overall data picture by extending to higher energy measurements of the scattering of He^+ ions, and it complements the extensive low energy measurements[2,3] for these same collision partners.

The experimental techniques and apparatus are considerably different in the present measurements from those used by other workers. These differences will not be specified here; they are discussed in detail in Chapter IV.

CHAPTER IV

APPARATUS AND TECHNIQUES OF MEASUREMENT

The present apparatus was originally designed to perform a coincidence experiment.[66] To accomplish this task and also to have a most versatile piece of equipment, the design provided the capability of measuring the cross section differential in either the scattering angle of the projectile or the recoil angle of the target. Thus, there exist two detection systems which rotate about a common axis and which view a common volume of the incident beam in the collision chamber. The present experiment utilizes only one of these detection systems, the analysis system for the fast scattered particle.

In discussing the apparatus, we shall consider the source of projectiles, the hardware of the scattering experiment, i.e., the mechanical construction, the vacuum system and the electronics, the tests used to evaluate the experimental equipment, and the techniques which were employed in making the actual measurements. Also, the source of possible errors in the measurements will be discussed.

Source of Projectiles

A one MV Van de Graaff positive ion accelerator was the source of projectiles in this experiment. This accelerator has been previously described in detail.[66,67] During the present measurements, the energy calibration was verified empirically by measuring with a nuclear magnetic resonance gaussmeter the field of the beam analyzing magnet that corres-

ponds to the 1.019 MeV threshold energy[68] of the $H^3(p,n)He^3$ nuclear reaction.

He^+ ions were the projectiles used during this investigation. In order that the states of the collision partners be precisely defined, it was very important that these projectiles be in their ground state when entering the collision chamber. The following discussion will present the reasons for believing the projectiles were in the ground state upon entering the collision chamber.

Certainly, when the ions were first formed in the ion source bottle in the Van de Graaff, they populated all excited states of the ion. Between the source bottle and the collision chamber the projectiles traveled a path of approximately 10 meters with a velocity of 10^8 cm/sec, thus, the flight time from source to collision chamber was of the order 10 μsec. Along this path the projectile (1) traveled through the accelerator tube where the field strength was of the order of 8×10^3 volts/cm, (2) traveled through a set of deflection plates in which the field strength was approximately 500 volts/cm, (3) were deflected by the analyzing magnet which sorts the proper charge state with an "equivalent" electric field ($E = v \times B$) of approximately 10^4 volts/cm, and (4) passed through a final set of deflection plates where the field was of the order 200 volts/cm, before entering the collision chamber.

The lifetime of an excited state of a hydrogen-like atom of nuclear charge Z is of order $Z^{-4}(10)^{-9}$ sec.[69] Hence, the lifetimes of the excited states of the hydrogen atom, which are tabulated,[70] are certainly an upper limit on the lifetimes of the allowed states of a He^+ ion. For the following estimates these tabulated lifetimes have been used.

Excited states with $n \leq 6$ have very short lifetimes and will decay before reaching the collision chamber. The 2s state is an exception and will receive special attention below. Excited states (ns) where $6 \leq n \leq 18$ have lifetimes too long to decay in the flight time of the projectile; however, Stark mixing of the substates of each n state in the electric field of the accelerator tube will cause these states to decay before reaching the collision chamber. The mixed states have a transition probability approximately equal to the transition probability of the (n,p) level. The lifetime, τ, of these states is given by

$$\tau(n,p) \simeq 0.054\ n^3 \times 10^{-8} \text{ sec}$$

for all states $n \leq 25$.[71] Excited states for $n \geq 18$ will be stripped of their electron due to Lorentz ionization[72] in the electric field of the accelerator tube and will be eliminated when the beam is charge selected by the deflecting magnet. Hence, all allowed excited states of the projectile will have undergone radiative decay or will have been Lorentz ionized before reaching the collision chamber.

Particular attention must be given to the metastable 2s state. Harrison, et al.[73] report that the lifetime of this state as a function of the quenching field, ξ, (volts/cm) is

$$\tau = \frac{1.4(10)^{-2}}{\xi^2} \text{ sec} .$$

The electric fields in both the accelerator tube and the analyzing magnet are sufficient to quench this metastable state; thus, it should be ef-

fectively removed from the beam before the projectiles reach the collision chamber.

One other problem that must be considered is the repopulation of excited states through collisions with residual gas. The background pressure in the connecting tubing between the deflecting magnet and the collision chamber is better than 10^{-5} Torr. Assuming a cross section of excitation into excited states of 10^{-19} cm^2, less than 0.01 percent of the incident beam will be excited between the analyzing magnet and the collision chamber. Therefore, it is concluded that the projectiles entering the collision chamber are He^+ ions in their ground state.

Description of Scattering Apparatus

Mechanical Construction

The apparatus utilized in this experiment is composed of four principal parts: the support and rotation assembly, the collision chamber, the projectile collimation, and the analysis system. These subsystems which will be described can be seen in Figure 4.

Support and Rotation Assembly. A stainless steel shaft, Figure 5, is the kingpin of the entire apparatus. It is mounted vertically, and this shaft supports and aligns the entire experiment. Its center line is the axis of rotation for both detection systems. The bottom of the shaft has a close-tolerance fit through a massive piece of thick-walled steel tubing. A lip on the shaft rests on the top of this tubing (these are both finished surfaces) and these support not only the shaft but the entire apparatus. A lock nut holds the shaft rigidly to the tubing. The tubing itself is welded both to the top and bottom flanges of three I-beams which are in turn welded together along both flanges. A steel plate

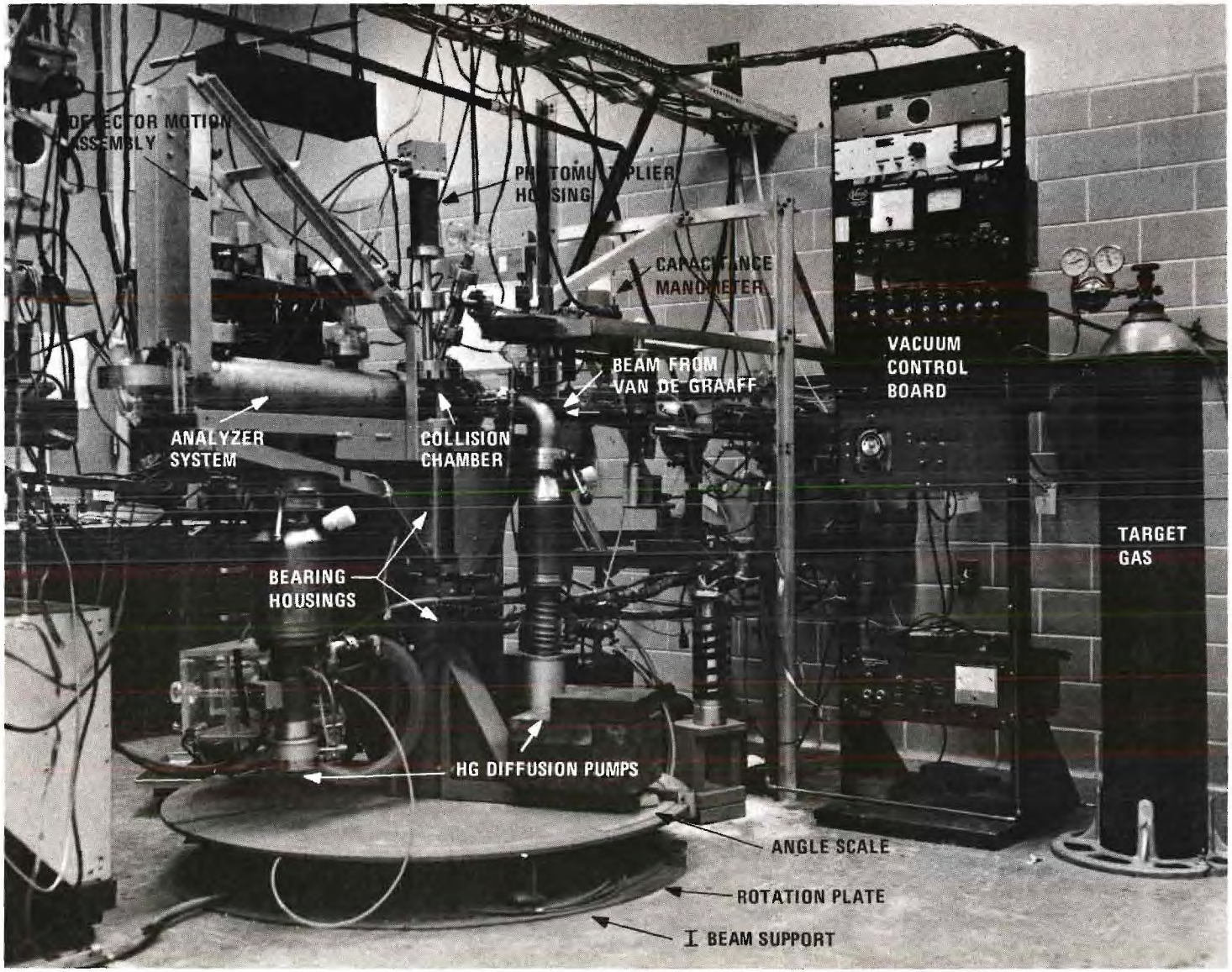

Figure 4. Apparatus.

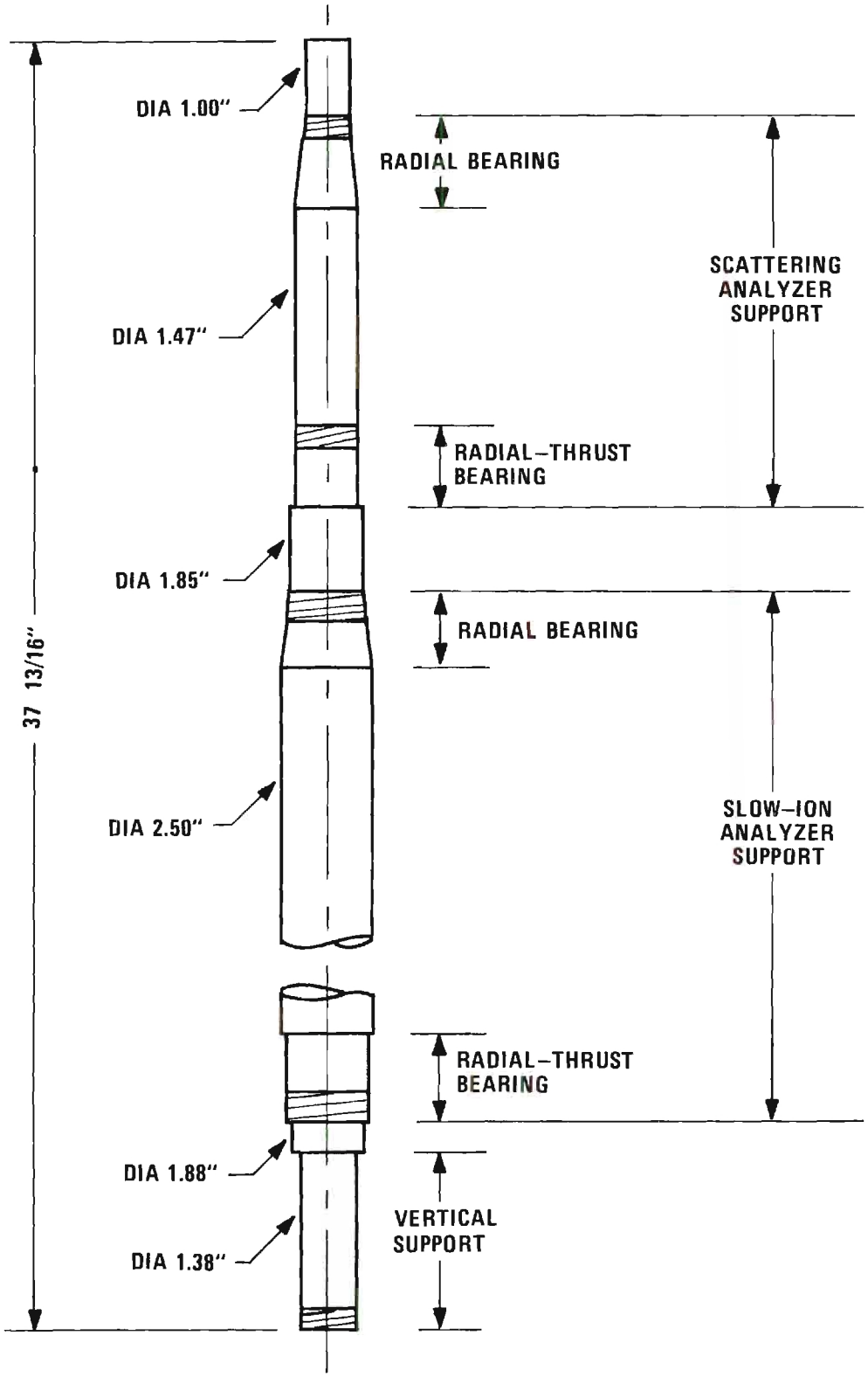

Figure 5. Main Support Shaft.

of diameter 48.6 inches is screwed to the top of the I-beams, and it has the angle scale mounted on it. (The thick-walled tubing and joints of the I-beams are hidden beneath this steel plate and cannot be seen in the photograph, Figure 4.)

A five-eighths inch bolt located at the end of each I-beam provides the apparatus with a vertical degree of movement and tilt for alignment with the ion beam from the Van de Graaff. The five-eighths inch bolts rest on a plate which can be rotated relative to the base plate providing a horizontal degree of freedom in aligning the apparatus. These features are visible in the photograph, Figure 4. These two degrees of movement are for gross alignment of the entire apparatus with the projectile beam from the accelerator. The internal alignment procedures and provisions for steering the projectile beam will be discussed below.

Two identical rotation systems are attached to the shaft, one mounted vertically above the other. The lower rotation system supports the slow-ion recoil assembly (which was not utilized in the present experiment); the upper rotation system supports the fast beam analyzer (referred to henceforth as the analyzer system). The mounting positions of these analyzers are shown in Figure 5.

Each rotating detection system is suspended by two high-precision bearings. The bottom bearing is of a two-way radial thrust type. It is slipped on the shaft to a machined shoulder which supports it. This bearing is actually a pair of back-to-back radial-thrust ball bearings which were prestressed to remove all clearance and preload the bearing. The top bearing is a double row radial roller bearing in which zero clearance is attained in a different manner. The inside of the inner race has a

slight taper, matched by a taper on the shaft at that location. A nut on the shaft above this bearing is tightened, driving the bearing down the taper to stretch the inner race and stress the rollers. The high precision performance of this bearing is dependent on proper tightening of this nut.

Rigidly attached to a massive steel housing that is closely fitted to the outer race of these bearings is a massive arm supporting the analyzer system and, exactly opposite it, an angle indicator and counterweight arm. The counterweight is adjusted to eliminate, as far as possible, any net torques from acting on the shaft. These features are visible in Figure 4.

Collision Chamber. The collision chamber rests atop the main axle shaft. Three bellows connect the collision chamber to the rest of the apparatus. These bellows are welded to the chamber and flanged to the bases of three brass cones. The tips of these cones protrude into the collision chamber proper to within approximately an inch of the rotation axis. These cones hold the collimating apertures for the projectile beam, for the recoiling slow ions, and for the scattered fast particles. Figure 6 is a photograph of the interior of the collision region where the tips of the three cones are visible.

In the present experiment it was necessary to provide a means of measuring the projectile current in the collision region and, further, to be able to monitor this current continuously. Mounted to the top of the collision chamber is a retractable Faraday cup, for absolute measurement of the beam current, and a photomultiplier and lens assembly, for continuous monitoring of the product of the beam current and target gas

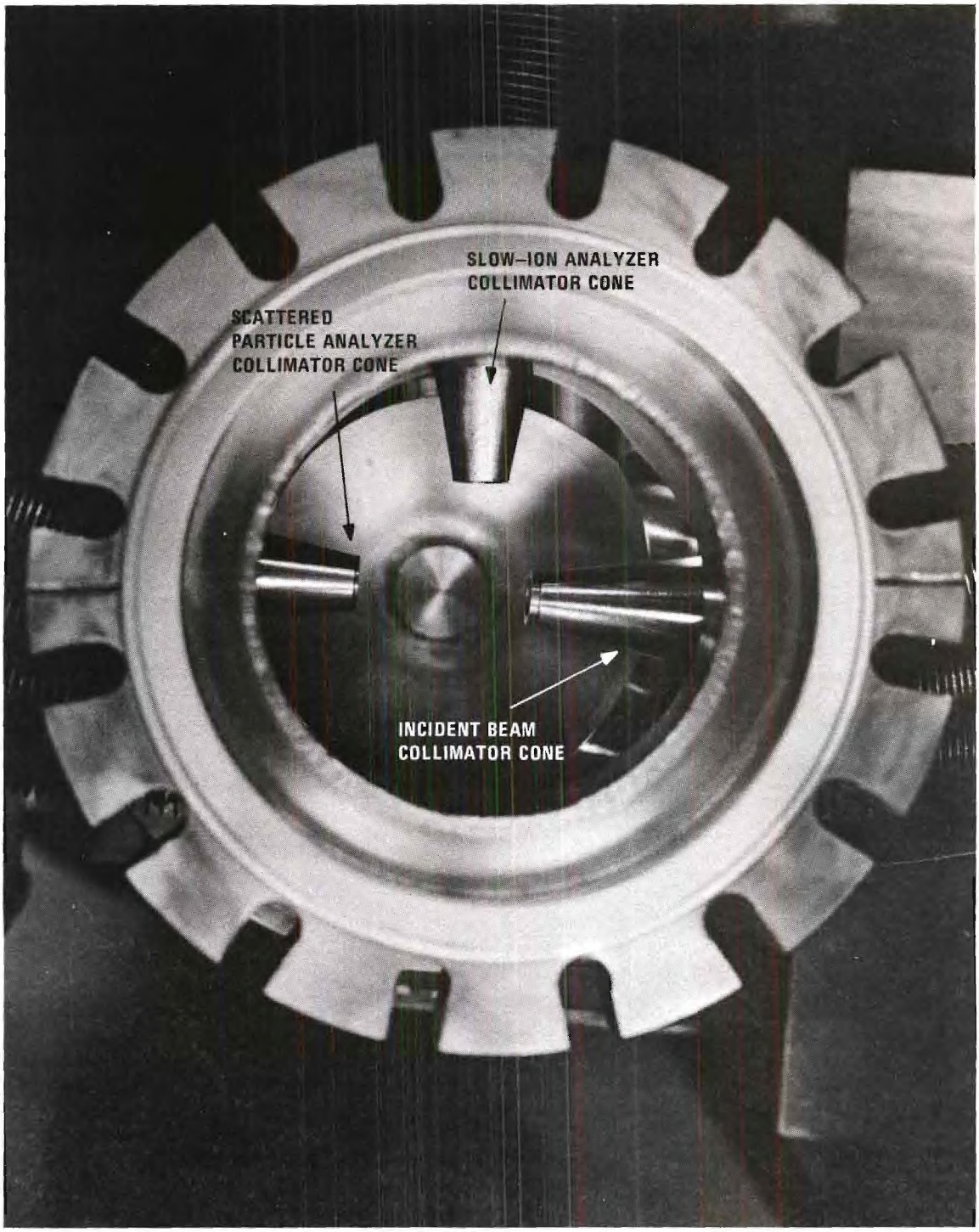

Figure 6. Interior of Collision Chamber.

pressure. This monitoring system will be discussed in a later section of this chapter. The top of the collision chamber can be seen in the photograph, Figure 7.

The Faraday cup has a slanted back surface so that secondary electrons emitted when the projectile beam impinges on the back of the cup are directed preferentially to the walls of the Faraday cup. Additionally, there is a secondary electron suppressor plate in front of the cup and insulated from it. The projectile beam entered the Faraday cup through a circular hole, three-sixteenths inch in diameter, located in the center of the suppressor plate. The beam diameter at this point was less than 0.042 inch. (The beam diameter is discussed below.) This shield was negatively biased (typically -20 to -60 volts) to return any secondary electrons near the mouth back into the cup. Current to this shield could be monitored. When the cup was in fully extended (down) position, it was observed that no current was collected on this shield (whether it was negatively biased or not).

The photomultiplier was an E. M. I. #6256S tube. It measured the collisionally induced photon emission from the target gas. The properties of this photomultiplier tube and associated optical components will be discussed in a later section of this chapter.

These mounting arrangements of the Faraday cup and the photomultiplier require that the top of the chamber remain stationary with respect to the projectile path through the collision chamber. This chamber was mounted so that it was free to rotate about the vertical axis as the angular positions of the two analyzers were varied. However, the slight rotations accompanying movement of only the fast beam analyzer over the angular

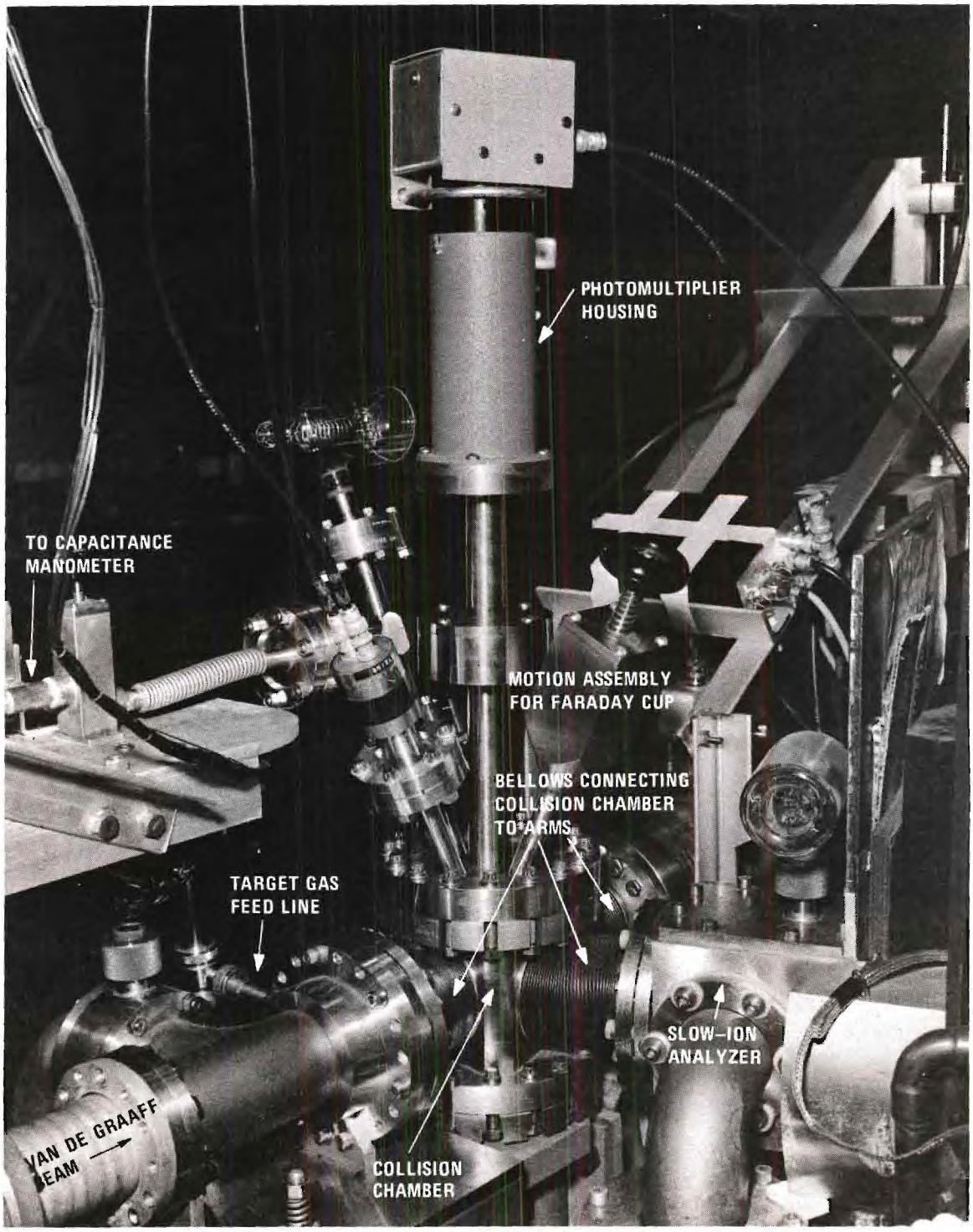

Figure 7. Top of Collision Chamber.

range involved in the present measurements were observed not to affect the photon counting rate or the projectile current measured with the Faraday cup. Also mounted to the collision chamber is an ionization gauge and a flexible connection to a capacitance manometer.

To better illustrate exactly how the Faraday cup and photomultiplier are mounted, a cross sectional view of the top of the collision chamber is shown in Figure 8. A bellows assembly from a two inch Veeco gate valve provides motion for the retractable Faraday cup. In its "down" position the collimated beam from the Van de Graaff is intercepted by this cup; while in its "up" position the cup does not obscure the view of the beam region of the photomultiplier. The Faraday cup collected the beam at the same location as that viewed by the photomultiplier; therefore, these measurements could not be made simultaneously.

A two-lens system focuses the photons on the photocathode. The first lens is mounted on the top of the collision chamber approximately two and one-half inches from the beam path. A fine Ni mesh of 97 percent transparency is mounted in front of this lens to prevent any charge buildup on this dielectric surface from producing fields in the beam region. The second lens (see Figure 8) then focuses the photons onto the photocathode. This lens also provides the vacuum seal. These features, as well as the Faraday cup in its retracted position, can be seen in Figure 8. The optics of this lens system are further described later in this chapter.

Projectile Collimation. The projectile beam was collimated by two apertures located in a non-rotating arm attached to the main support shaft. These apertures were 0.025 inch in diameter and were separated by five inches. The projectiles pass through a third aperture of larger diameter

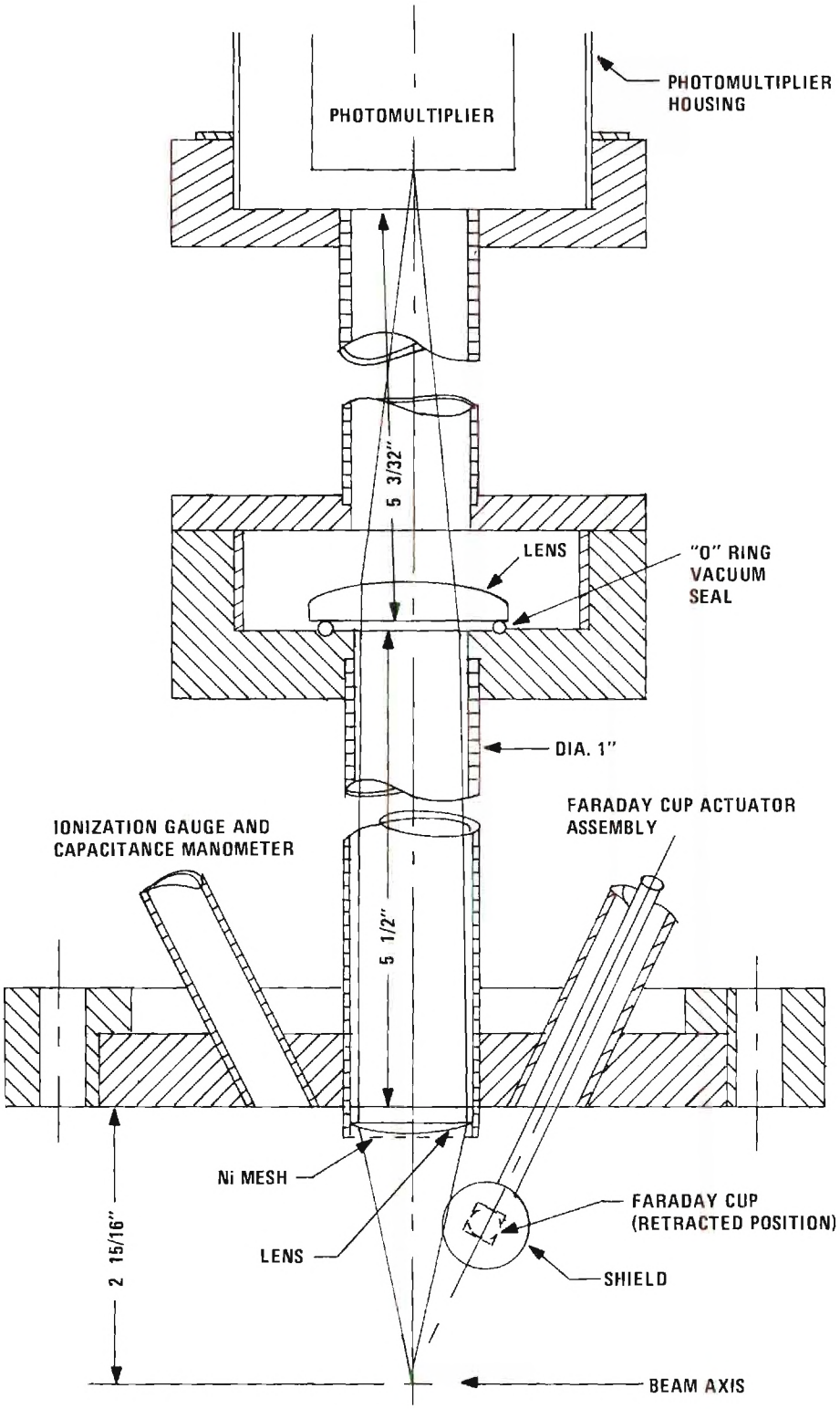

Figure 8. Cross Sectional View of Top of Collision Chamber.

to enter the collision region itself. This aperture is 0.048 inch in diameter and is located 1.48 inches from the axis of rotation. Its purpose is to confine the target gas to the collision region. The beam should not strike the edge of this aperture; however, some ion burn has been detected around the edge of this aperture. A diagram of the projectile beam collimation as well as the collimation of the scattered beam is given in Figure 9.

The maximum angular divergence of two rays defined by the 0.025 inch apertures is 34 minutes of arc. The third aperture (diameter 0.048 inch) limits this maximum divergence to 26 minutes of arc, which would produce a beam diameter of 0.059 inch over the rotation axis. However, the actual projectile beam is, in principle, nearly paraxial when it enters the two collimating apertures, because it comes from a small focus 10 feet away. Scattering from residual gas degrades this paraxial quality of the beam. Measurement of the smallest scattering angle indicates a maximum divergence of the projectile beam to be between 12 and 18 minutes of arc, but most of the intensity is much more paraxial than these maximum limits, as indicated by measuring the intensity profile. This leads to the conclusion that the diameter of the projectile beam was between 0.028 inch (only 0.003 inch greater than the geometrical optimum beam diameter) and 0.042 inch (considerably smaller than the worst possible case).

Analyzer System. Particles scattered through an angle θ were collimated and passed into the analyzer system by a two-slit geometry. This beam of scattered particles passed through a parallel plate electrostatic deflector for separating the charge states and was then counted individually with a surface barrier detector. At the energies of the present experiment

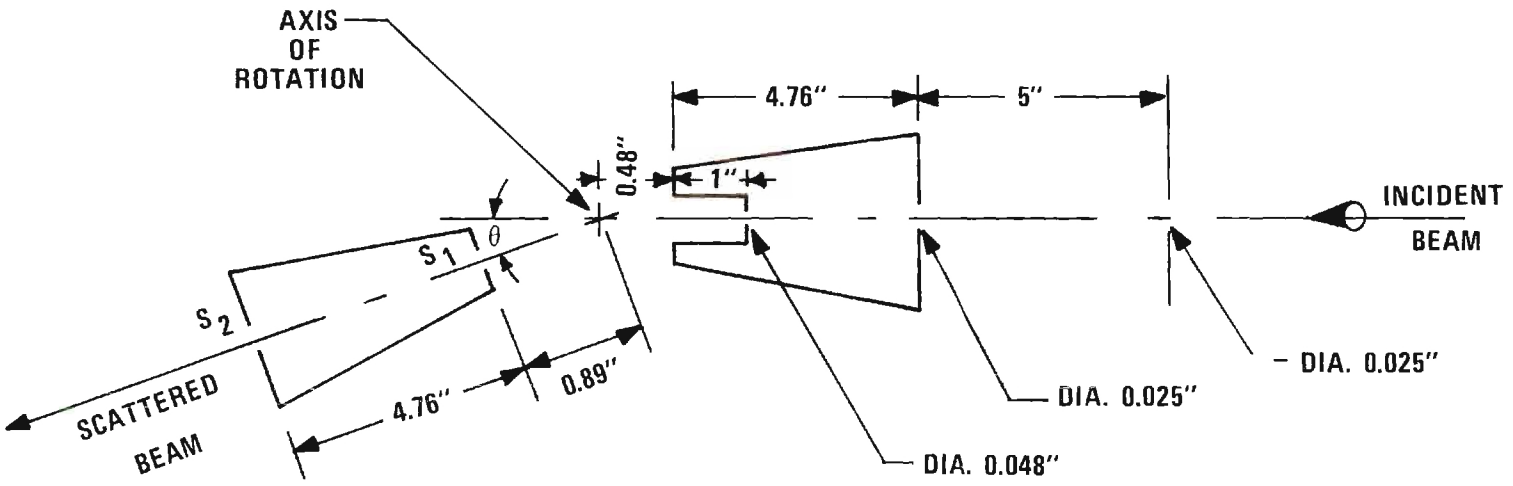

S_1 : 0.0156" x 0.040"
S_2 : 0.0091" x 0.0095"

Figure 9. Collimation of Incident and Scattered Beam.

this detector was 100 percent efficient. A schematic drawing of the entire apparatus, showing the relation of the analyzer to the projectile beam and the collision chamber, is presented in Figure 10.

The size and location of the slits forming the collimation geometry are shown in Figure 9. The calculated "maximum angular spread" of this geometry is 18 minutes; however, measurements of the width of the scattered beam at the detector, to be described later in this chapter, indicate an angular spread of approximately 10 minutes. The minimum angle possible before an edge of the first aperture (0.0156 inch x 0.040 inch) entered the unscattered beam in the collision region was approximately one degree. As soon as an edge of this aperture entered the main projectile beam, many particles of degraded pulse height (apparently scattered from the slit edge) were counted by the detector, and it became impossible to make measurements below this limit. (The method of detecting these slit-edge scattered particles will be described in the "Techniques" section of this chapter.)

The scattered beam was collimated by two rectangular slits, thus, at the detector, the scattered projectiles formed a rectangularly shaped beam. Measurements (to be described below) indicated the size of this beam to be approximately 0.070 inch x 0.090 inch (width by height), and these dimensions are in good agreement with calculated estimates based on the geometry of the two-slits. The calculated maximum divergence of a beam that could pass through these two-slits would give an image 0.120 inch x 0.150 inch at the detector.

The scattered particle analyzer section of the apparatus is contained in a long stainless steel tube whose supporting frame is rigidly

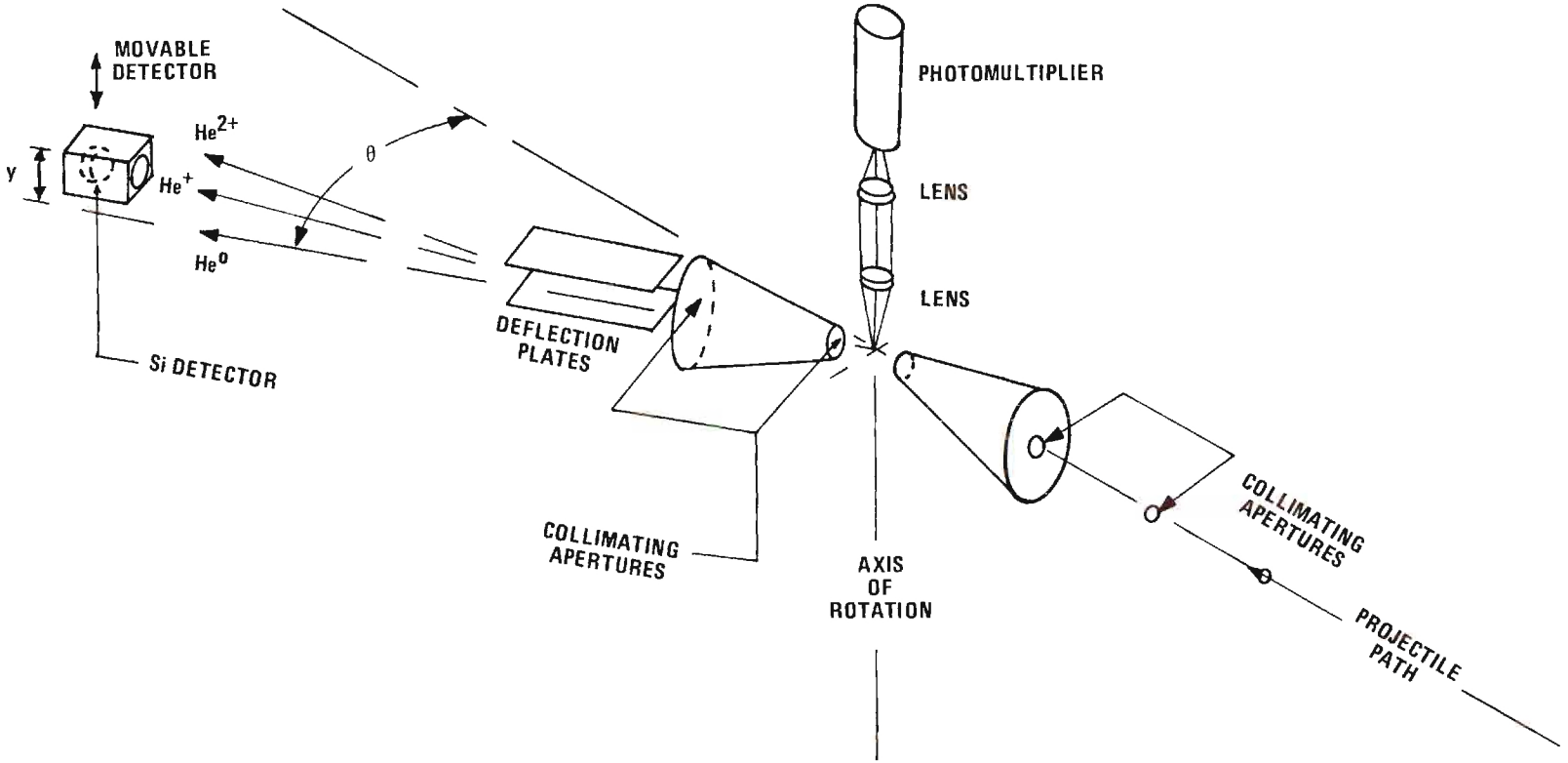

Figure 10. Schematic of Scattering Apparatus.

secured to the bearing housing (see Figure 4). As previously described, this bearing housing, and thus the entire analyzer, rotates about the main support shaft. The base of one of the three cones previously mentioned was attached to the front of the analyzer. This cone protruded through the bellows connection with the collision region to a point approximately one inch from the rotation axis. The small apertures which define the collection geometry are located in the front and rear of the cone.

Immediately following the second aperture, at the base of the cone, are a pair of parallel plates. The surface of these plates lies in the horizontal plane so that deflections produced by them are in the vertical plane. This is shown schematically in Figure 10. The bottom plate is grounded, while an electric potential can be applied to the upper plate to deflect the beam of charged particles.

Eighteen inches past the center of the deflection plates is the vertical plane containing the silicon surface-barrier detector. At the rear of the chamber is a Faraday cup which can be used to measure the beam current in the analyzer section when $\theta \approx 0$ degrees. It is useful for studying the beam profile and to locate the true $\theta = 0$ position. The design of this cup is very similar to the design of the Faraday cup in the collision chamber, i.e., this cup has a slanted back surface and also an electron suppressor plate, insulated from the Faraday cup, the particles entering the cup through a circular hole in the center of the suppressor plate. This Faraday cup collects scattered beam measured as a current only for scattering angles less than 20 minutes. This limitation is imposed by the current measuring capability of an electrometer,

which was used to measure this current. (The current sensitivity of the electrometer was mentioned in the preceding chapter.) The projectile current in the collision chamber cannot be measured with this Faraday cup in the analyzer section even with $\theta = 0$, because the defining apertures into this analyzer are smaller than the cross sectional area of the beam in the collision chamber. Measurement of the total incident current was provided by the retractable Faraday cup directly in the collision chamber, which has already been discussed.

A silicon surface-barrier detector was used to count all particles scattered through angle θ and entering the two-slit collimation assembly of the analyzer system. This detector counts the scattered projectiles with 100 percent efficiency. (The properties of this detector will be described later in this chapter.) This detector is shielded from the environment of the analyzer system by a small box which is completely enclosed except for a hole allowing the particles passing through the two collimators to strike the front of the detector. The detector, with a portion of the box removed, is shown in the photograph, Figure 11.

The shielding box containing the detector was mounted to a drive mechanism, through a bellows, which allows it to be moved, both horizontally and vertically, in the plane perpendicular to the analyzer axis. Figure 12 shows a photograph of this drive mechanism with the detector connected to it. This movement capability was provided so that the silicon detector could be aligned on the axis of the analyzer section, as defined by the undeflected beam of scattered particles, and also moved vertically to receive particles deflected a particular distance. It was necessary that the vertical motion be very uniform and reproducible because

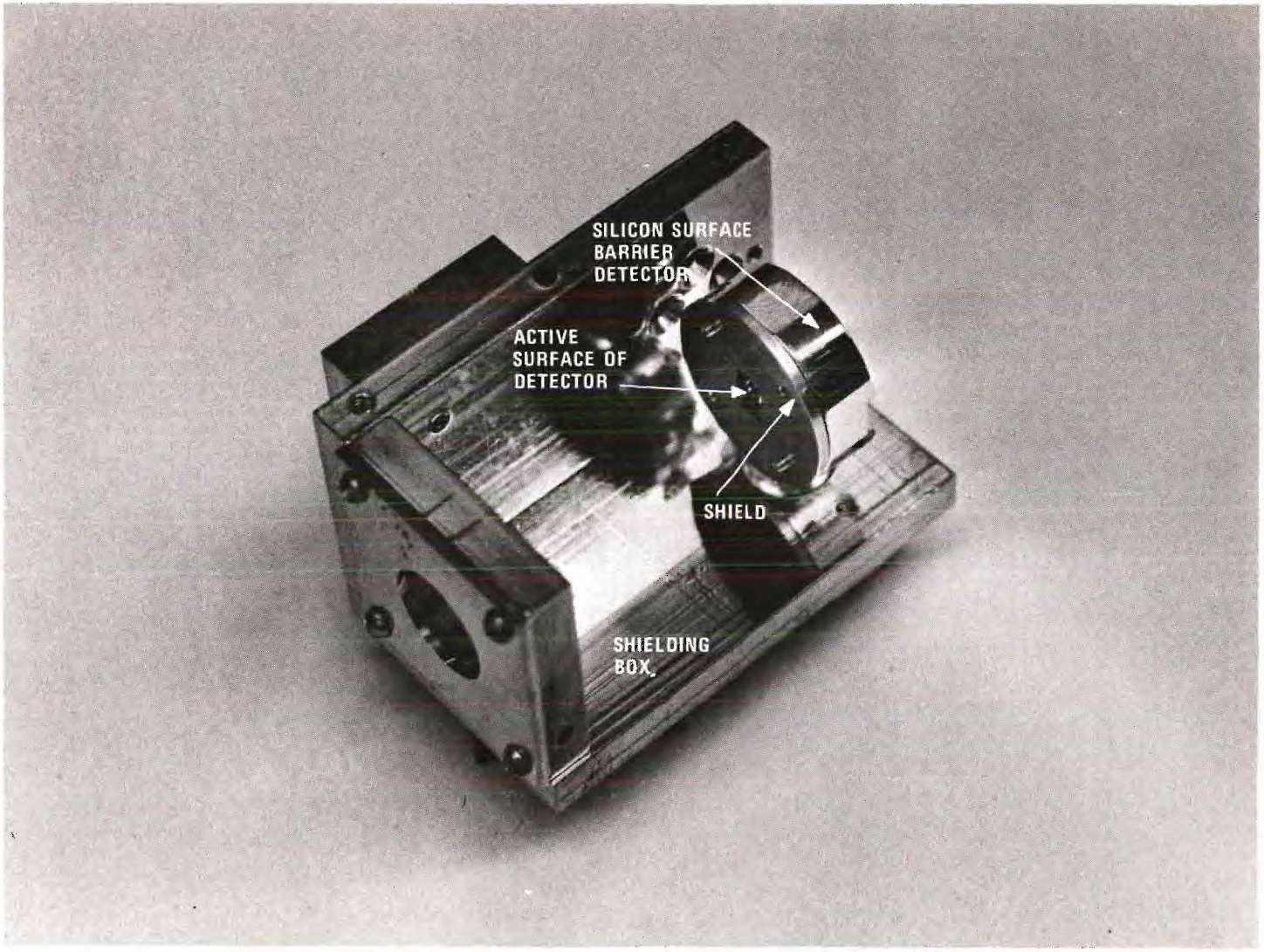

Figure 11. Silicon Surface Barrier Detector.

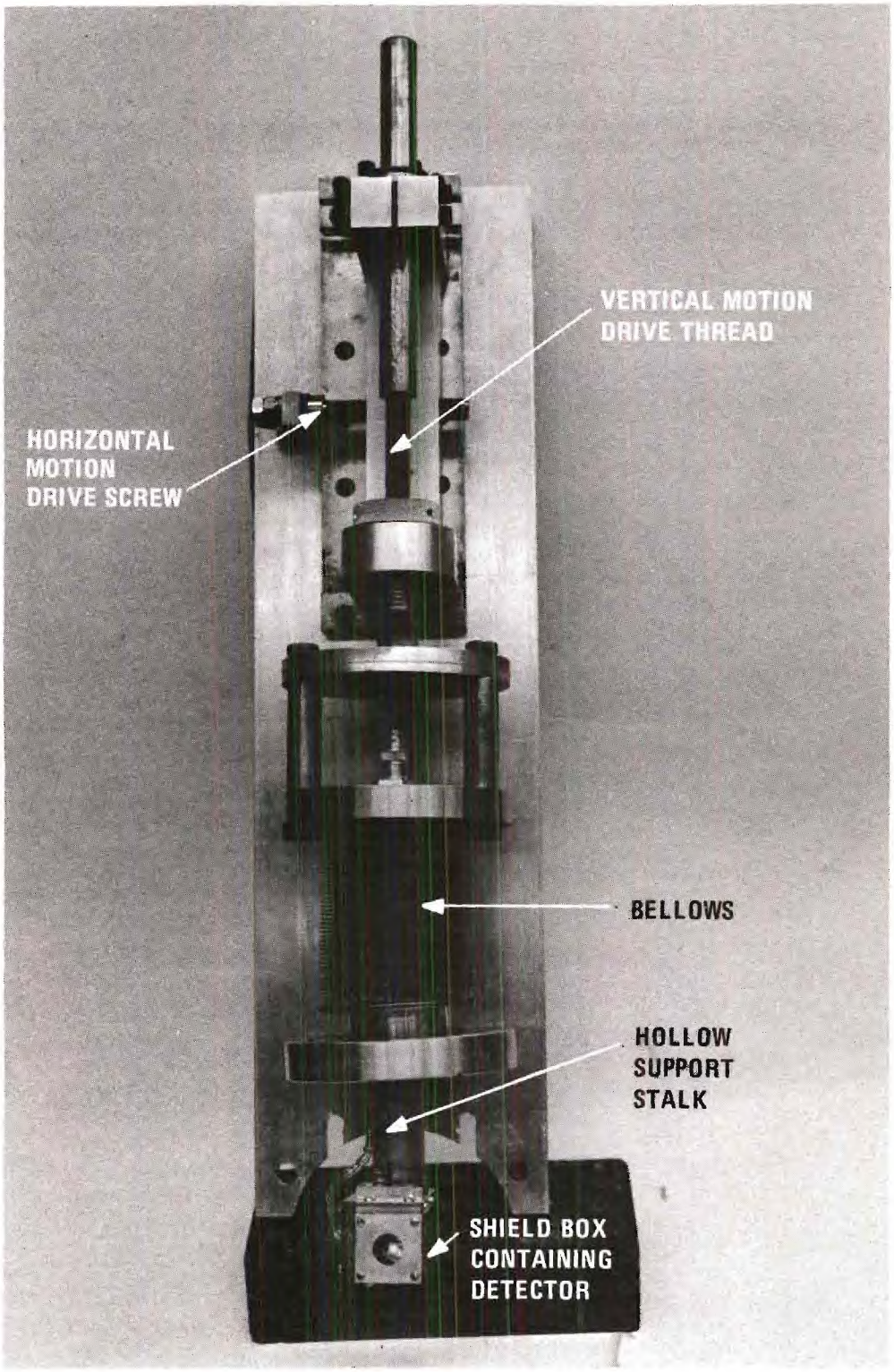

Figure 12. Two-Dimensional Motion Assembly for Silicon Detector.

the detector had to be moved vertically to a precisely defined position each time the number of particles of a particular charge state was to be counted. (The charge states of the scattered beam were separated by the deflection plates, see Figure 10.)

A case-hardened steel rod moving in a precision roller bearing provided the vertical motion for the detector. The bottom portion of the rod was threaded, and a drive nut served to move the rod a known distance to determine the position of the detector. This motion was used frequently throughout the measurements; it appeared to be uniform and reproducible to within 0.015 inch.

The horizontal motion was required only to optimize the centering of the detector in the deflected-particle plane. The movement was accomplished by a screw which drives the entire "vertical motion drive" in a horizontal track. This motion proved to have quite a bit of backlash; however, as it was only very infrequently used (only when the silicon detector was replaced), it presented no particular difficulties and was adequate.

The stalk which supports the detector shielding box in the collision chamber is actually a hollow tube, open to the atmosphere at the top but vacuum sealed at the bottom, which can be filled with a refrigerant (CO_2 or LN_2) to cool the detector and thus reduce thermal noise. However, this measure was found not to be necessary. The features of the mounting and motion assembly of the silicon detector can be seen in the photograph, Figure 12.

Initial tests indicated some spurious effects which were attributed to particles striking the glue around the edge of the detector face, which

holds it in a ceramic ring. A brass shield placed immediately in front of the detector and having a knife-edged hole opening only onto the active area of the detector eliminated this problem.

Alignment Procedures

Two stages were involved in the alignment of the apparatus; first, the apertures for collimating both the incident beam and the scattered particles were aligned (the internal alignment), and second the entire assembly was adjusted (using vertical and rotation adjustments described earlier) to receive the projectile beam from the Van de Graaff. As the external alignment simply rotates, elevates, and tilts the entire assembly, only the internal alignment procedures will be described.

A He-Ne laser was mounted so that its beam traveled along approximately the same path as the ion beam. It was possible to remove the bottom plate of the collision chamber and place a small pointer in the axis of rotation so that it extended into the laser beam path. With this point as a guide, the laser was moved to aim its beam directly at the rotation axis. Once this was accomplished, the laser was not moved. The apertures collimating the projectile beam and the two apertures collimating the scattered beam were individually aligned on the laser beam. The procedure itself was actually a series of successive approximations, because the construction and mounting of the incident beam collimator was such that one aperture could not be moved without affecting the position of the others. This feature was also true of the apertures collimating the scattered beam.

This alignment set the $\theta = 0$ position of the scattering analyzer. It was estimated, by observing the shifts in the diffraction pattern of

the laser beam, that the zero degree position was determined to less than five minutes of arc. Later scattering measurements with the ion beam determined that the zero angle determined with the laser beam was two and one-half minutes. (Following a later partial realignment, zero degrees was found to be at five minutes.)

A further set of variables which was used on a day-to-day basis after these initial mechanical alignments was provided by two sets of electrostatic deflection plates for steering the incident beam into the apparatus. One of these sets of plates was located before the beam analyzing magnet, the other set was located after this magnet. The voltages on these plates were empirically adjusted to maximize the projectile current in the collision chamber.

With the apertures thus aligned, the projectiles were collimated to a narrow beam of particles whose diameter was greater than 0.025 inch but less than 0.042 inch, and this beam passed through the axis of rotation. The two collimators leading to the analyzer section were aligned on the projectile beam, and the zero position of the angular scale was known within five minutes of the true path of the projectile beam. This fact was verified by subsequent measurements with the projectile beam from the accelerator.

Vacuum System

The vacuum in the experimental apparatus was obtained by three two-inch Edwards mercury diffusion pumps. The three pumps were mounted beyond the bases of the three cones protruding into the collision chamber, i.e., one pump was mounted in the beam input region between the two 0.025 inch apertures collimating the projectile beam, one was located in the

fast beam analyzer, while the third diffusion pump was in the recoil ion analyzer. Each of these pumps was mounted beneath a liquid nitrogen trap. The base pressure in the regions directly above each of these pumps was typically 7 to 8 x 10^{-7} Torr.

The collision chamber was semi-isolated from the highly evacuated incident-beam and analyzer region by the small apertures which collimated the incident and scattered beams. This semi-isolation was necessary because the latter regions were held at high vacuum while there was a finite pressure of target gas in the collision chamber. Sufficient pumping speed for preliminary evacuation of the collision chamber was provided by a three-eighths inch hole in the side of the incident-beam cone. Additionally, since the slow ion analyzer was not being used, the small aperture which would normally be installed in the tip of its cone was omitted, leaving a three-eighths inch hole into the collision region. A base pressure in the collision region of 7 x 10^{-7} Torr has been obtained; however, a base pressure of 1 x 10^{-6} Torr was more typical.

While taking data, the target gas pressure in the collision chamber ranged from 5 x 10^{-4} Torr to approximately 2 x 10^{-3} Torr. A large portion of the measurements was made with a target gas pressure of approximately one micron (1 x 10^{-3} Torr). Under operating conditions, when the pressure was one micron in the collision chamber, the pressure in the analyzer system remained approximately 1 x 10^{-6} Torr; in the beam collimation region, between the first two apertures, the pressure would be 1 to 2 x 10^{-4} Torr, because of the extra pumping hole in the side of the cone separating this region from the collision chamber. This was a cause of concern; however, careful investigation indicated that the collision chamber pressure had

to be four microns or greater before the measurements began to be noticeably perturbed by multiple collisions. Figure 13 shows this fact graphically. The ratio of the number of scattered particles to the number of incident beam particles is plotted against the target gas pressure. This graph should be a straight line of the form $y = sx$ where the slope, s, is proportional to the product of the differential scattering cross section and the geometrical factor. Deviations from the straight line indicate the onset of multiple scattering. (The effect of the increased gas pressure in the input region would cause a scattering of the incident beam, thus a larger incident beam in the collision region. Also, charge changing collisions could occur, which would destroy precise knowledge of the state of the incident beam.) Since the data were taken at pressures well below four microns, it was concluded that multiple collisions did not affect the measurements.

Pressure in the tubulation connecting the apparatus to the accelerator was approximately 5×10^{-6} Torr during operation. This was maintained by two two-inch Edwards oil diffusion pumps.

The target gas is fed into the system through an Edwards needle valve. The feed line was originally maintained at approximately atmospheric pressure; however, this procedure was changed and throughout a large part of this work the line was maintained at five to 10 psig. This gas line passed through a trap immersed in dry ice and acetone to remove condensible vapors. The major features of this gas feed system can be seen in Figure 4.

During the early part of this work the pressure in the collision chamber was measured using only an ionization gauge. This method was not

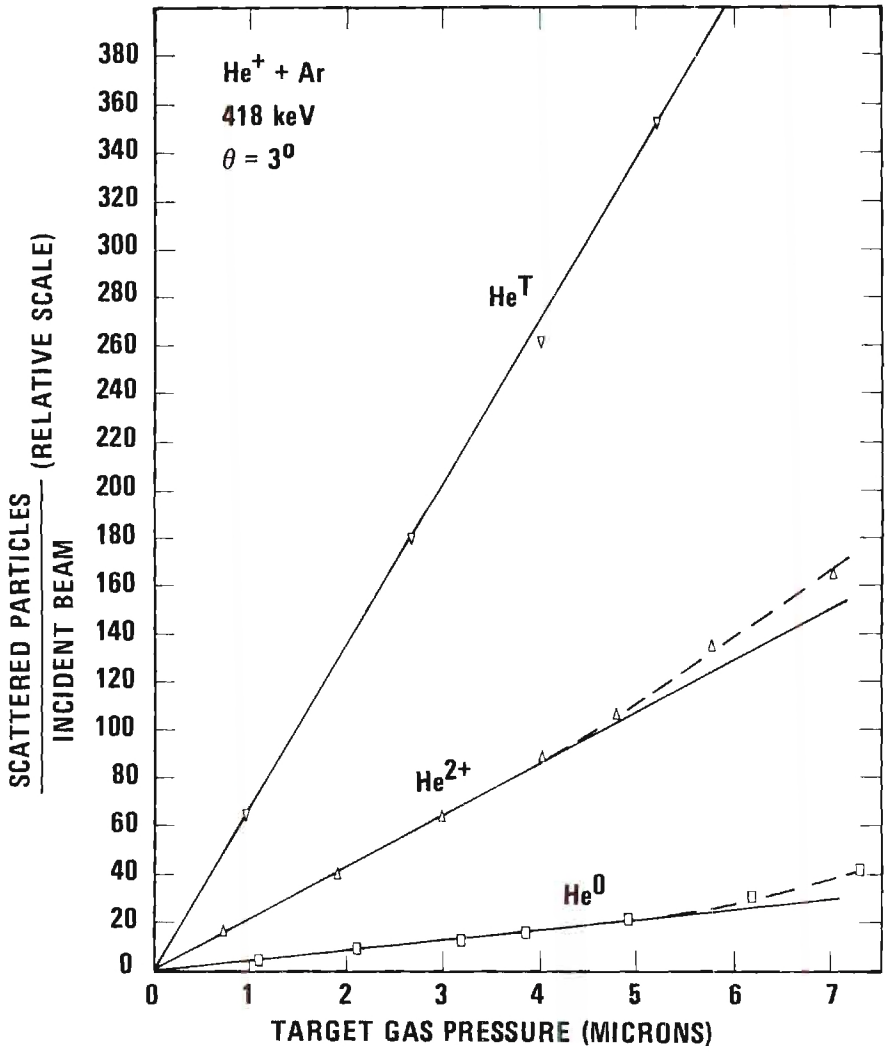

Figure 13. Scattered Projectiles Versus Pressure.

reliable enough for absolute determination of differential scattering cross sections; therefore, a capacitance manometer was added to the apparatus. This device has many advantages over the much older accepted standard, the McLeod gauge. The most notable of these advantages is that a capacitance manometer measures pressure in the sense of the definition[74] (i.e., as a force/unit area) and does not depend on the properties of a particular gas. The capacitance manometer was calibrated at the factory before shipment, but this calibration was at a much higher pressure than those used in this experiment. Therefore, it was felt necessary to calibrate the capacitance manometer against a standard in the pressure range that would actually be used. This calibration is described in Appendix B.

The reference side of the capacitance manometer was evacuated by a one inch Edwards oil diffusion pump with a liquid nitrogen trap. It maintained a reference pressure of less than 5×10^{-6} Torr.

Electronics

In this section we shall discuss the signal handling from its origin, the detector, to its conclusion where the information was presented in a useable form by displaying it on a scaler, by printing out the results on a teletype, and/or by punching a paper tape. The information handled consisted of sets of numbers representing (1) scattered particles, (2) photons, (3) target gas pressure, and (4) beam current. The procedures used are shown schematically in Figure 14. All identifying numbers referred to in this block diagram are Ortec equipment model numbers.[75] Other data used in this work were recorded by direct observation of meters or scales.

A silicon surface-barrier detector, which was used to count the

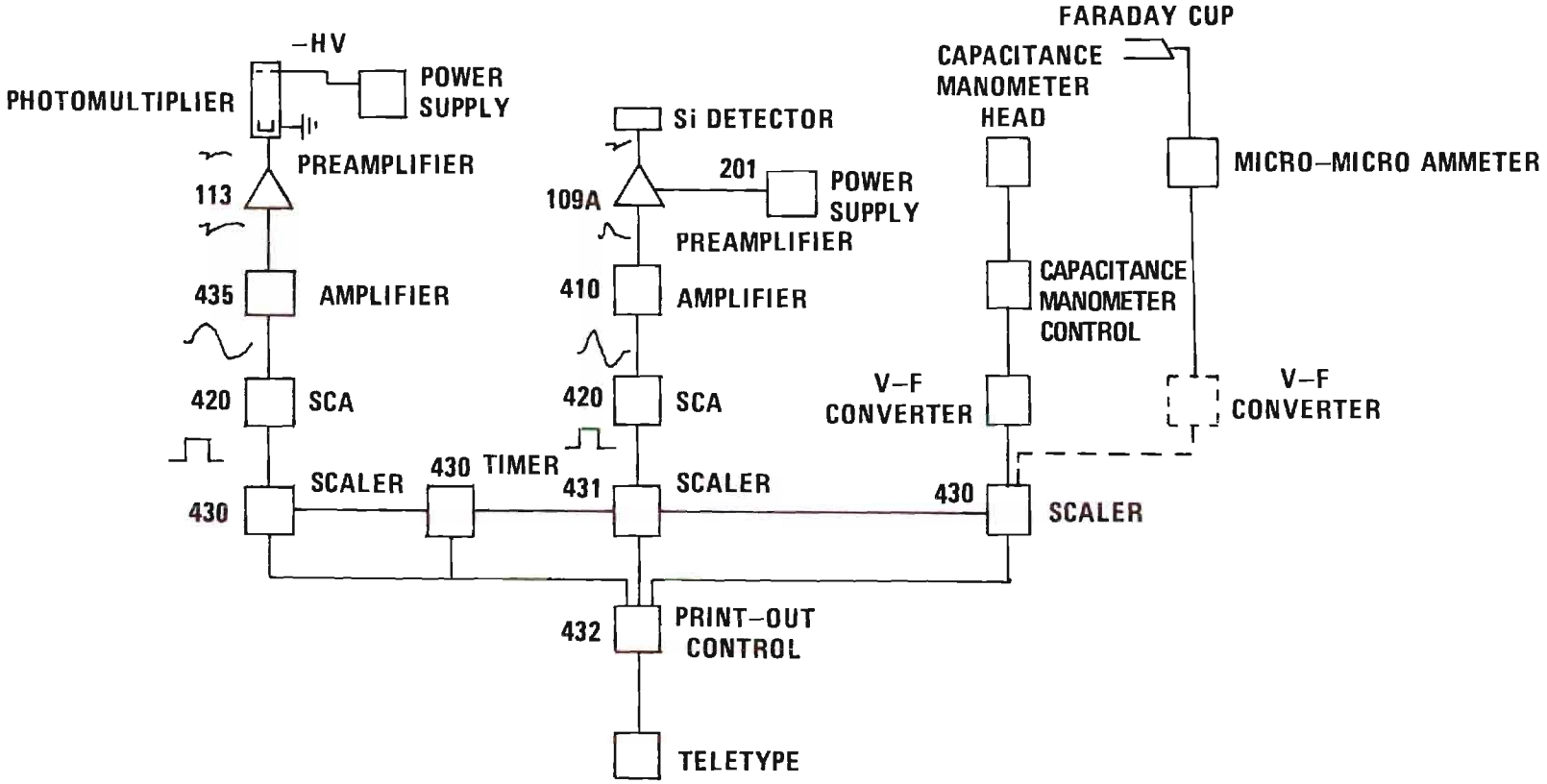

Figure 14. Wiring Schematic.

scattered particles, is a large area diode functioning as a solid state ionization chamber. A pulse of charge collects on the plate of this detector for each particle penetrating the thin gold window on the front of this device. The window has a thickness of approximately 40 $\mu g/cm^2$. The size of the pulse is dependent only on the energy of the incoming particle, not upon its charge state. (The charge of the counted particle is determined geometrically by the position of the detector and by the voltage applied to the deflection plates.) A single lead connects the detector, which is inside the vacuum chamber, with the preamplifier which is just outside the vacuum. This lead serves both to supply the operating voltage to the detector and to conduct the signals from the detector to the preamplifier.

The preamplifier, Ortec #109A, is a charge sensitive device having a field effect transitor (FET) input. In the preamp the pulse is amplified, inverted, and shaped to a rise time of approximately 40 nsec and a fall time of 50 μsec. This pulse travels to a linear amplifier, Ortec #410, which provides great flexibility in pulse shaping. This pulse shaping capability was found to be useful for optimization of the signal to noise ratio. During this work, a doubly differentiated R C shaping was used with time constants from 0.1 to 10 μsec. It was possible to separately adjust the two differentiation times and the integration time, but these were kept equal in the present measurements. Time constants of two μsec and 10 μsec were most commonly used; but, when working with high counting rates, it was necessary to use very small time constants to prevent dead time losses. The 10 μsec setting was particularly useful, for it discriminated rather strongly against picked-up noise. Some pulse

shapes and the useable count rates obtained with different time constants, are shown in Figure 15.

The shaped pulses were next fed into an Ortec #420 timing single-channel analyzer (SCA). This instrument was used primarily to provide a discrimination level, i.e., to reject pulses whose amplitudes were less than a preset value. The "window" of the single channel analyzer was employed to verify that a narrow pulse height spectrum was being produced and also to see that the center of the pulse height spectrum, which was set by the gain of the amplifier, was large enough to easily discriminate against random noise. (The distribution of the pulse height spectrum was also continuously monitored by observing the amplifier output on an oscilloscope. This monitoring paid large dividends in time saved by making it immediately evident when the scaler was recording counts from noise, slit-edge scatter, or other extraneous sources.)

When a linear pulse at the input of the #420 SCA exceeded the discriminator threshold, the unit developed an output logic pulse, five volts in magnitude and 500 nsec in width. The logic pulses were counted with a scaler, Ortec #430 or #431. The accumulated count could be automatically printed by a teletype machine or punched on a paper tape. These last two features in the data handling were accomplished by an Ortec #432 print-out control system.

An E.M.I. #6256S photomultiplier tube was used to detect collisionally induced photons in the collision region. (The photons were counted to provide a monitor of the beam current.) This photomultiplier tube is a 13 stage venetian blind type having a fused silica window. The photocathode was held at high voltage (typically -1100 volts) with the

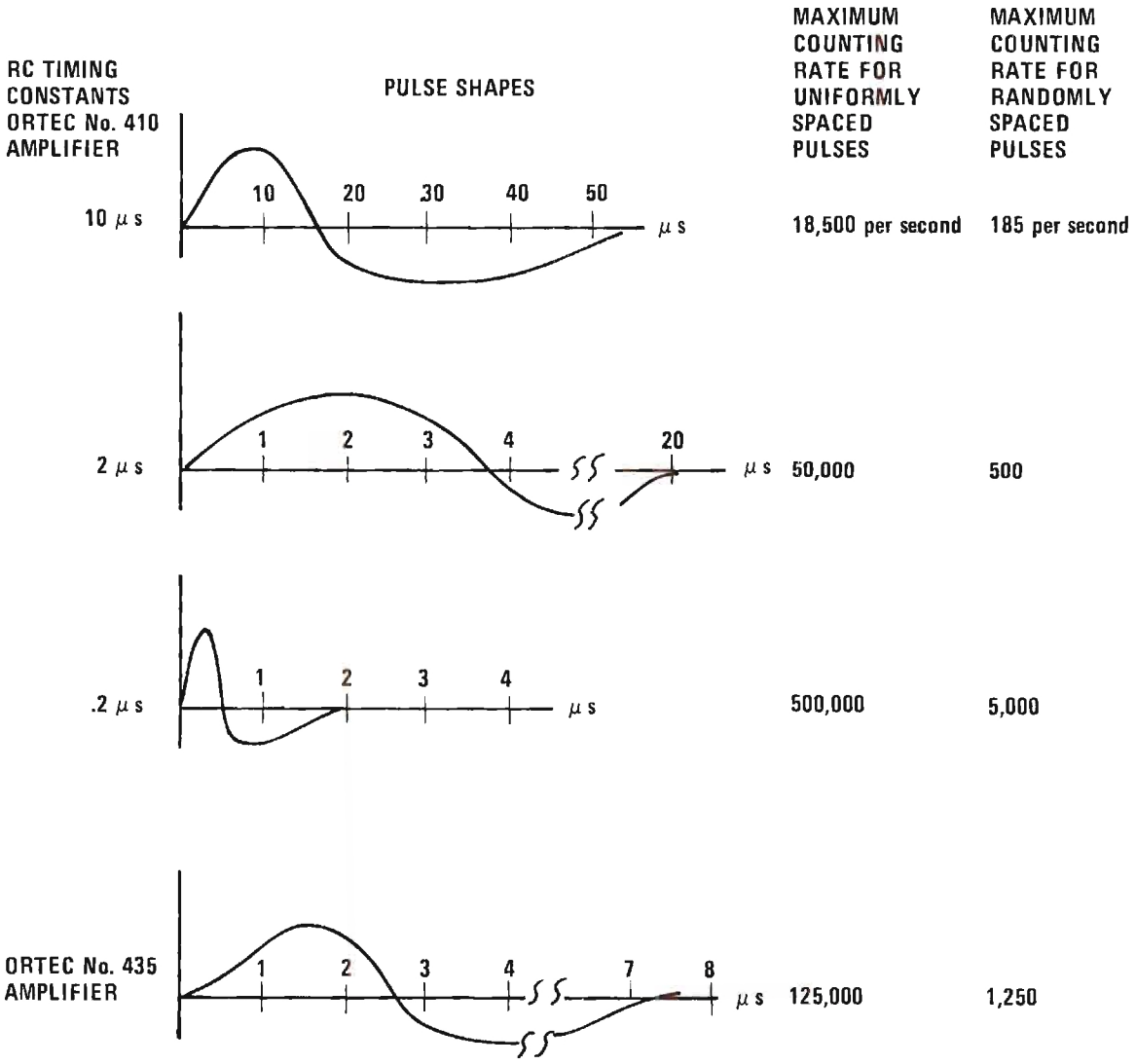

Figure 15. Pulse Shapes and Maximum Counting Rates.

anode end at ground. The wiring of the tube is shown in Figure 16. The high voltage was furnished by a Hamner model N-413 supply.

The signal collected at the anode was fed to a voltage sensitive preamplifier, Ortec #113. This is a non-inverting device with unit gain having low output impedence to drive the cable to the amplifier. It shapes the pulse to a rise time of less than 60 nsec and a fall time of 50 μsec.

The pulse from this preamp was fed into an Ortec #435 amplifier which gave a Gaussian shaped bipolar output. From here the signal was handled identically to the scattered particle signal, i.e., passing first to an Ortec #420, SCA used as a discriminator and then to a scaler, Ortec #430.

The pressure was measured during the latter half of the work with a capacitance manometer. The instrument provided, in addition to a meter readout, a dc voltage output which gave a 100 millivolt output for a full scale meter deflection. This dc level was fed into a voltage-to-frequency (V-F) converter (Hewlett-Packard model DY 2210). A V-F converter produces output pulses at a frequency that is proportional to an input dc voltage. The output pulses were counted on a scaler (Ortec #430) over the same time interval as the incident and scattered beam count. This arrangement digitizes the pressure reading and simultaneously integrates over the time of the measurement.

A very convenient feature of the Ortec #430 and #431 scalers is that one scaler can start and stop the counting of any number of other scalers simultaneously. This feature is provided by interconnections between these units. When a preselected "master" scaler reaches a preset

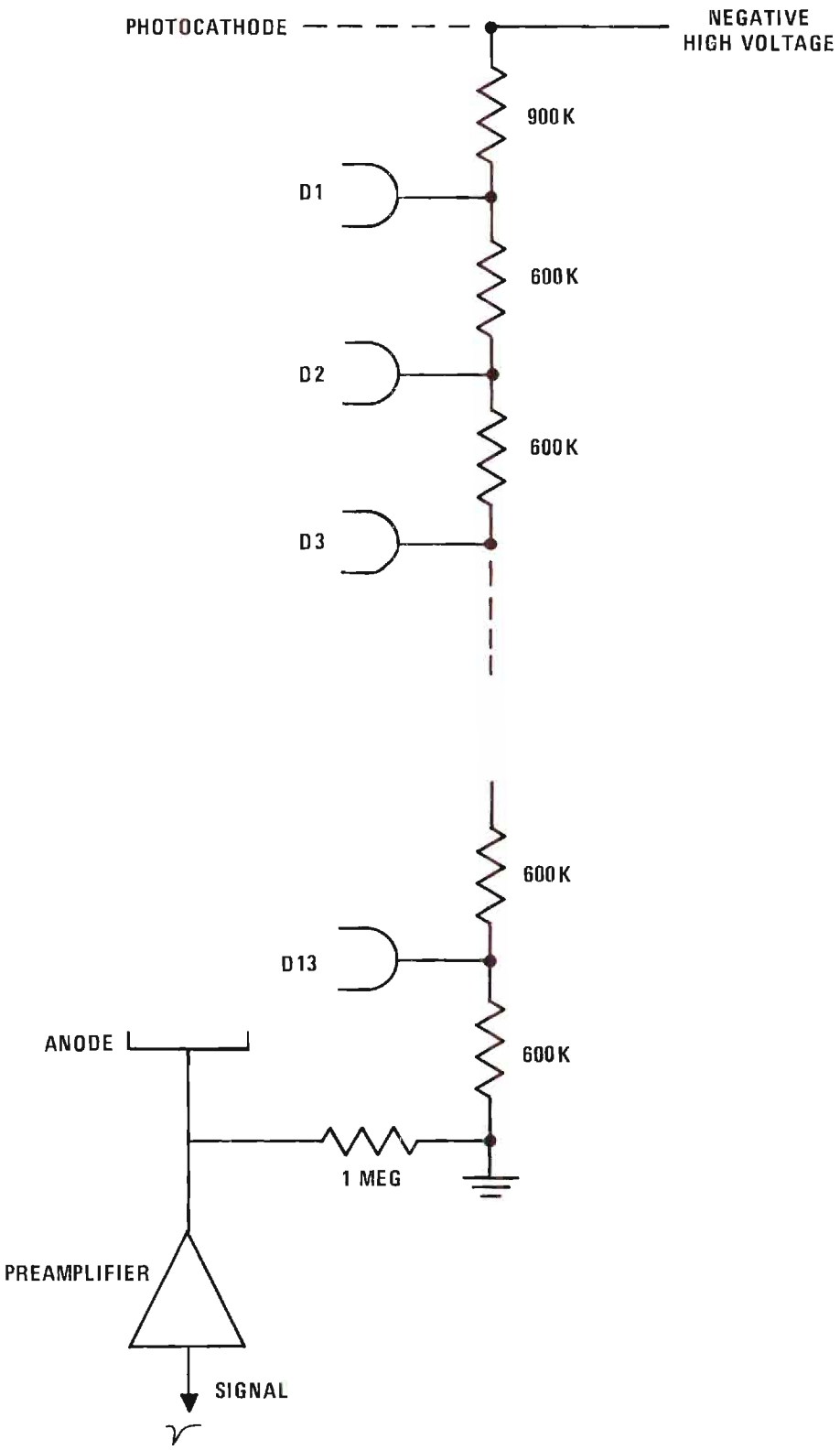

Figure 16. Wiring of E.M.I. #6256S Photomultiplier.

count, all scalers stop counting. During the present measurements, the scaler counting the number of photons was used as the master and all counting stopped when a preselected number of photon counts was reached. Thus, all counts were automatically normalized to constant incident beam for any given gas pressure. Four of these scalers were used: the three already described plus one used as a timer. (Any #430 can be switched to count the line frequency and thus display the elapsed time.) Therefore, the number of photons, the time to record this preset number of photons, the number of scattered particles, and the target gas pressure were simultaneously recorded for each data point.

During the calibration of the photon count rate versus beam current, it was necessary to read and record the current collected in the collision chamber with the Faraday cup which has been described in a previous section. This current was measured by a Keithley #415 micro-micro-ammeter. When making this measurement, the dc output from the Keithley was fed to the V-F converter so that a number proportional to the integrated beam current was counted with a scaler.

An extremely wide range of counting rates was encountered during the measurements (from less than one per second to greater than 5,000 per sec). A counting system, when fed pulses randomly spaced in time, will lose some counts due to dead time in the electronics at count rates much less than the maximum for regularly spaced pulses. From Poisson statistics it can be shown that small time intervals have a greater probability of occurrence than larger time intervals when considering randomly spaced events[76]; i.e., the pulses tend to arrive in clusters thus straining the electronics for brief increments of time. When the dead

time losses are small, the fraction of counts lost will be $\lambda\tau$, where λ is the observed average random pulse counting rate and τ is the resolving time of the system. In the present experiment, the count rate was kept at least two orders of magnitude below the maximum counting rate for uniformly spaced pulses; therefore, dead time losses were considered negligible in the present experiment.

Evaluation of Detection Systems

Scattered Particle Analyzer

The scattered particle analyzer was designed to detect particles scattered into its acceptance aperture with 100 percent efficiency and to determine their charge state. A silicon surface-barrier detector and an electrostatic deflection field were used to accomplish these tasks. Figure 10 gives an isometric view of the principal features of the analyzer section while Figure 17 gives a side view showing the important dimensions.

Scattered particles must pass through two collimating apertures to enter the analyzer. The geometrical considerations of such a two-slit arrangement are considered in Appendix A. Just inside the second aperture the particles are subjected to an electrostatic field, produced by a parallel-plate arrangement. Such a field functions as an energy analyzer, the deflections being independent of mass for given energy (actually, for given E/q, where q is the charge of the particle). In the present situation where a monoenergetic beam enters the analyzer, the deflection serves to separate the various charge components of the beam.

The voltage necessary to produce a given deflection is given by

$$y = \frac{Vqxd}{2Eb} \tag{40}$$

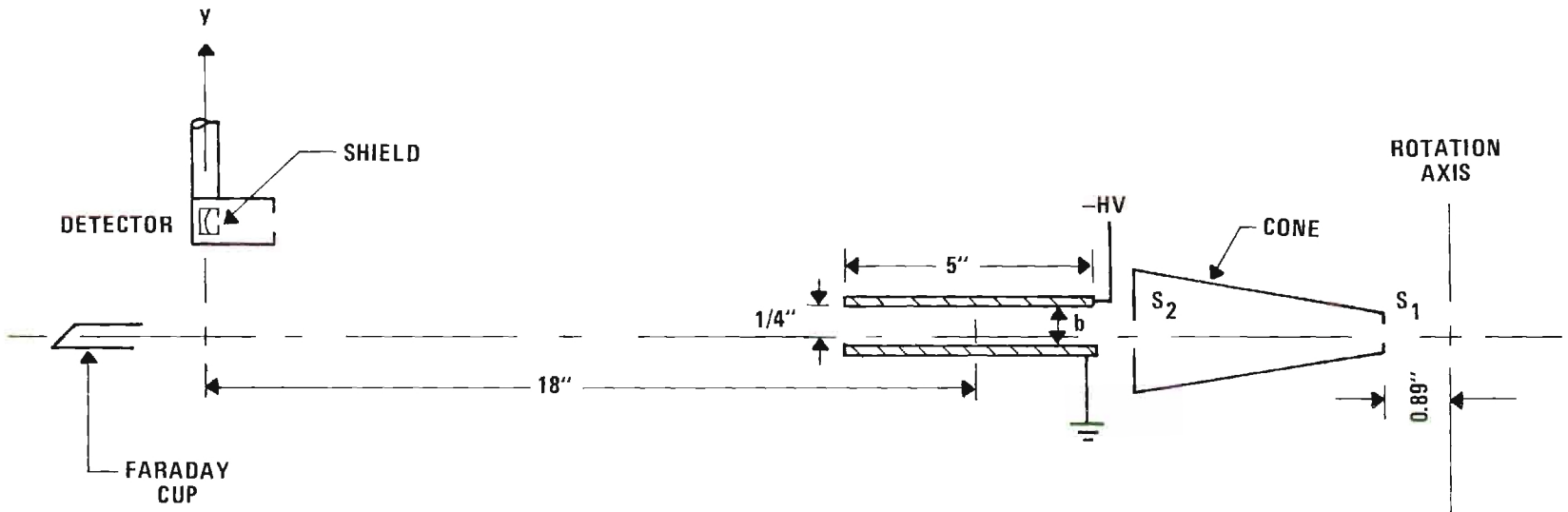

DIMENSIONS

S_1 : 0.0132" x 0.040"

S_2 : 0.0091" x 0.095"

b : 0.375"

Figure 17. Side View of Scattered Particle Analyzer.

where y is the vertical displacement of the ions at the detector plane, q is the charge, V is the voltage applied across the plates, x is the horizontal distance from the center of the plates to the plane of the detector, d is the length of the deflection plates, E is the energy of the ion, and b is the separation of the plates. In this calculation fringe fields were ignored. When the actual dimensions of the present apparatus are substituted into the equation it becomes

$$yE = 120\ qV \tag{41}$$

where y is in inches, E is in electron volts, q is in units of e, and V is in volts.

Thus, it can be seen that for a given energy E, there are two different methods by which this system may be used to detect scattered particles. One is to hold y fixed, thus making the left side of equation (41) a constant, since E is constant. Then, to satisfy the equation, qV must equal a constant. q has fixed values (q = 1 and q = 2); thus, as the voltage V is continuously varied, there will be two values of V for which equation (41) will be satisfied, these values corresponding to the physical situation when the different charge states are swept across the face of the detector. Notice that the highest charge state corresponds to the smallest voltage. For example, at 400 keV with y = 0.40 inch, He^{2+} ions are swept onto the detector when V = 660 volts, and He^{+} ions strike the detector when V = 1330 volts. Figure 18 illustrates this use of the detection system.

An alternate manner of detecting separately the various charge

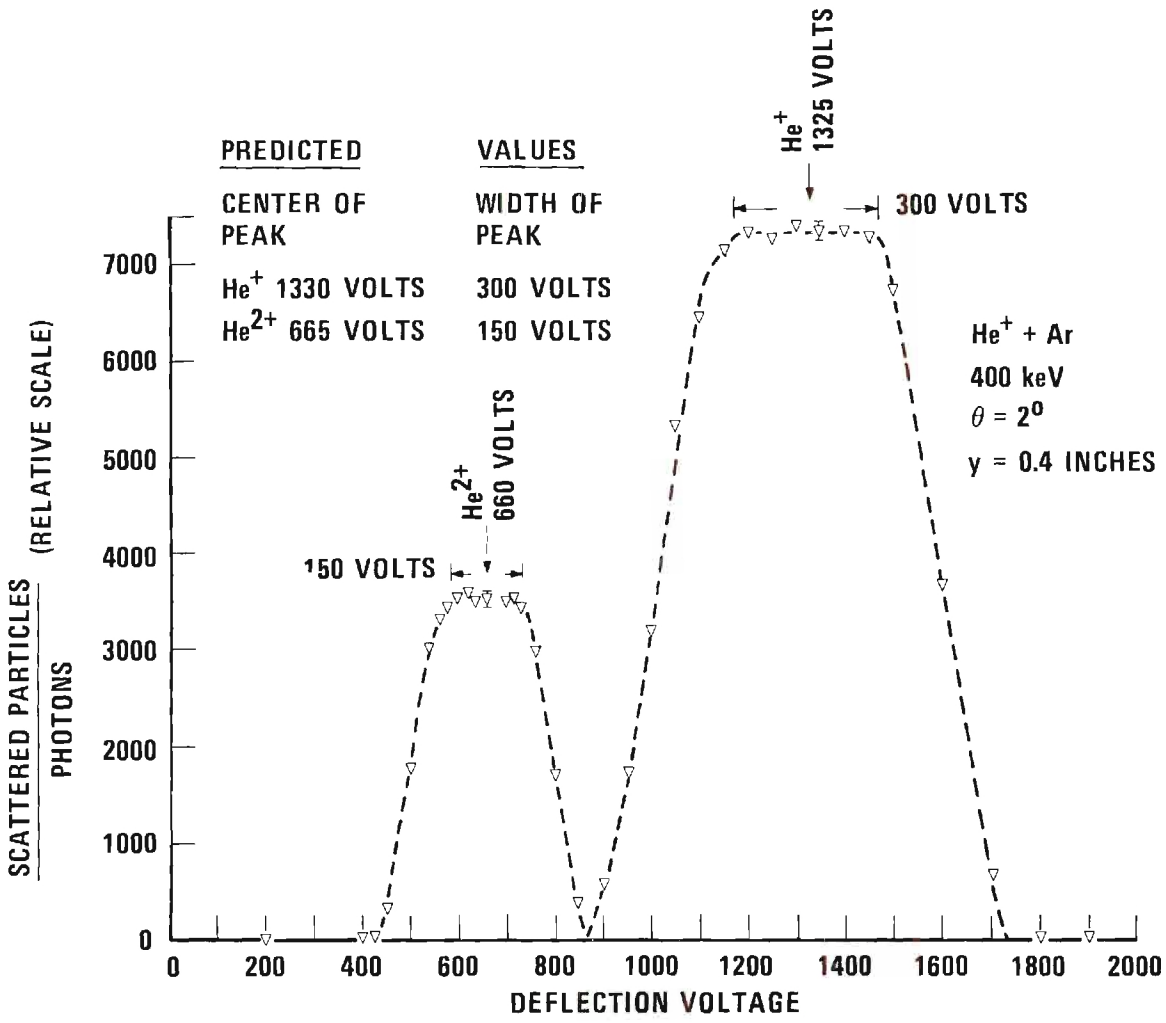

Figure 18. Scattered Particles Versus Deflection Voltage.

states consists of holding the voltage V constant and moving the detector along its vertical path. The results of this procedure are illustrated in Figure 19. In practice it has been found most convenient to utilize a combination of these two methods, particularly since it is impossible to detect neutral particles by the means first described.

By its very nature this deflection system is also an energy analyzer; however, this aspect is only of marginal value in the present experiment.

For the Si detector to produce an output pulse for an incoming particle, the projectile must pass through an Au window on the front of the detector. This window was a source of some concern, initially, for there was insufficient information at hand to predict whether or not the lowest energy particles could be detected with high efficiency.

To determine the response of the detector to the lowest energy projectiles in this experiment, 158 keV Ne ions were fired into the detector. Ne particles, being heavier than He, travel at slower velocities for a given energy; thus, straggling will be more pronounced for Ne as it passes through the Au window to the silicon wafer. Ne projectiles were used to test the detector under "worst case" conditions. Pulse height spectra showed the detector clearly separated Ne particles from the background noise. The pulse height spectra for 158 and 217 keV Ne particles are shown in Figure 20; spectra are presented for 217 keV particles at two different scattering angles. Figure 21 shows a pulse height spectrum for He projectiles. It is impossible to compare the relative positions of the peaks on these two figures, since different pulse height analyzers were used in taking the data, and it was not possible to normalize them.

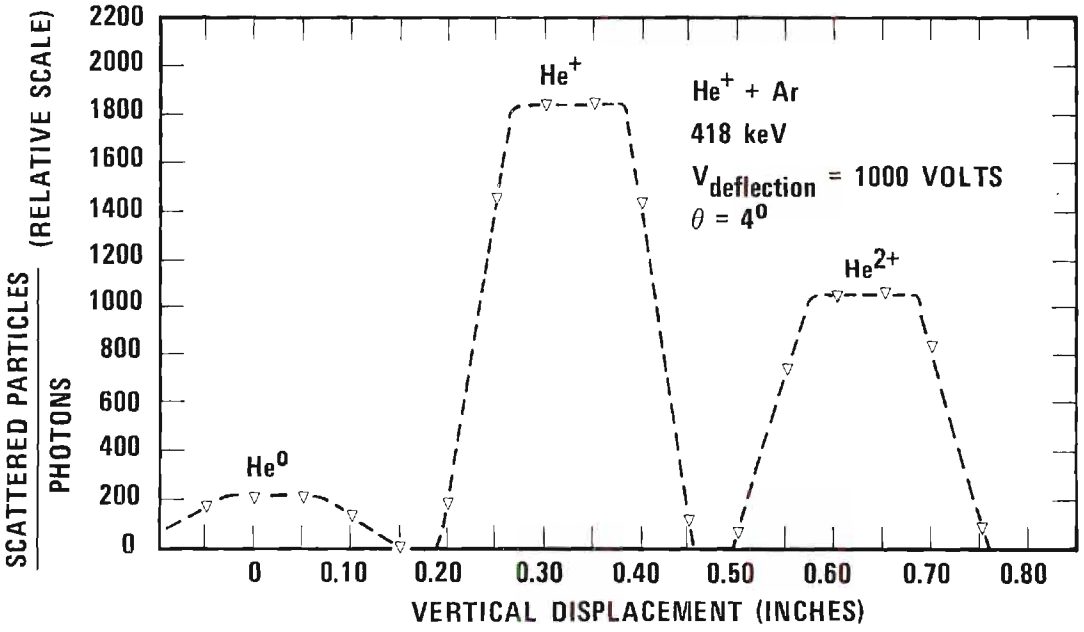

Figure 19. Scattered Particles Versus Vertical Position of Detector.

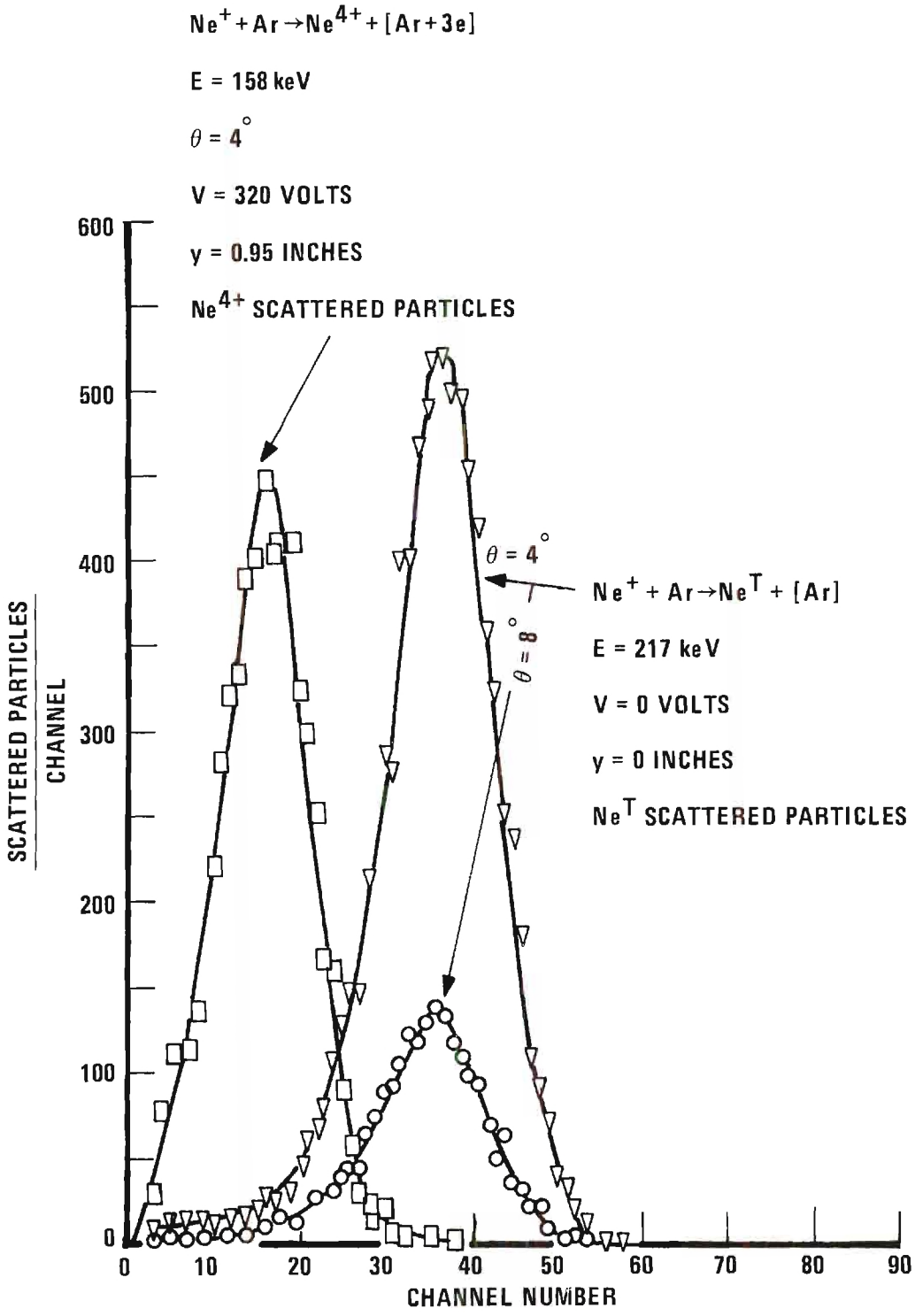

Figure 20. Pulse Height Spectra for Scattered Ne Particles.

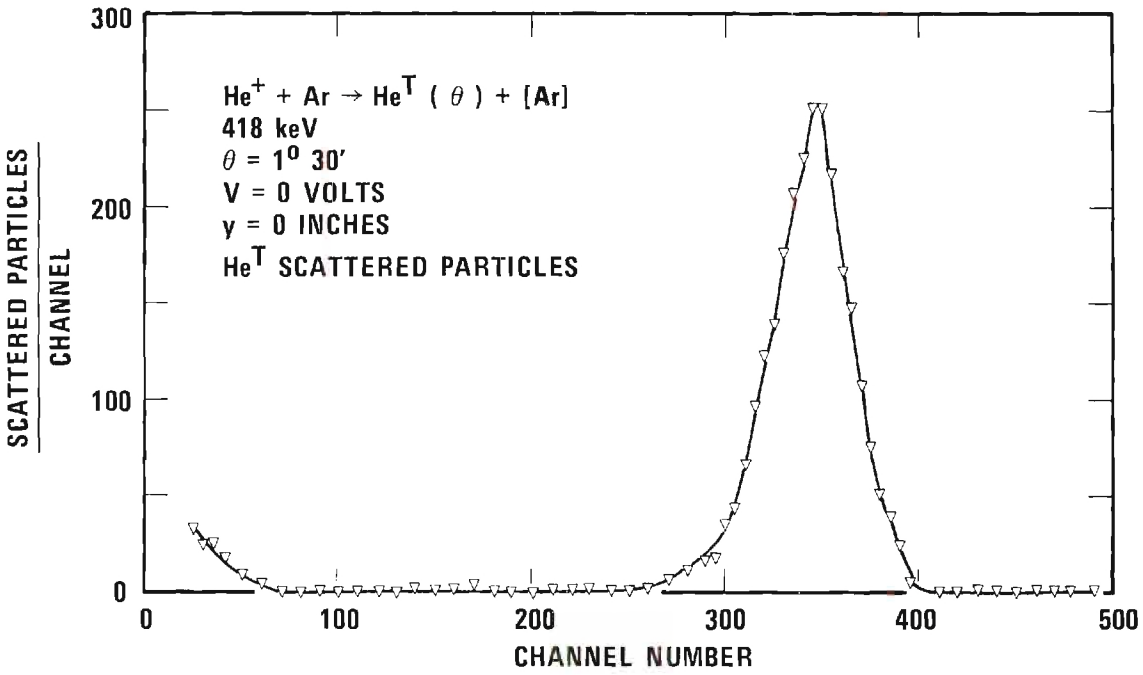

Figure 21. Pulse Height Spectrum for Scattered He Particles.

The narrow distribution of the pulse height spectrum for Ne projectiles at 158 keV, the separation of this distribution from background noise, and the increase in pulse height with increased particle energy lead to the conclusion that the detection efficiency of these detectors for a Ne beam whose energy is at least 158 keV is 100 percent. Straggling will be far less of a problem for He than for Ne particles in passing the Au window. Therefore, it was concluded that the detector used in the present measurement was 100 percent efficient for He projectiles.

Before making measurements it was necessary to insure that all particles of a given charge scattered into the solid angle $d\omega$ defined by the entrance collimator at scattering angle θ struck the detector. This was accomplished by sweeping the detector through the beam first in the vertical direction and then in the horizontal direction.

Figure 22 illustrates the beam profile measured in the horizontal plane. The width of this pattern and its shape are consistent with geometrical calculations estimating the spread of the beam in the detector plane. The measured beam profile is approximately 0.130 inch wide; however, most of the intensity originates in a narrow band, the "umbra", which is defined in Appendix A, having an approximate width of 0.070 inch on the detector surface.*

Once the horizontal position had been optimized, it was not again disturbed unless the detector itself had to be removed from the analyzer.

---

*During the course of the measurements, four different detectors were used. The first two had an active area of 25 sq mm. The shield used with these detectors had a knife-edged hole of diameter 0.188 inch. To verify that no particles were striking the horizontal edge of this shield, the last two detectors had an active area 50 sq mm and employed a rectangular shield of dimensions 0.250 inch x 0.188 inch. Results with these two detector and shield combinations were identical.

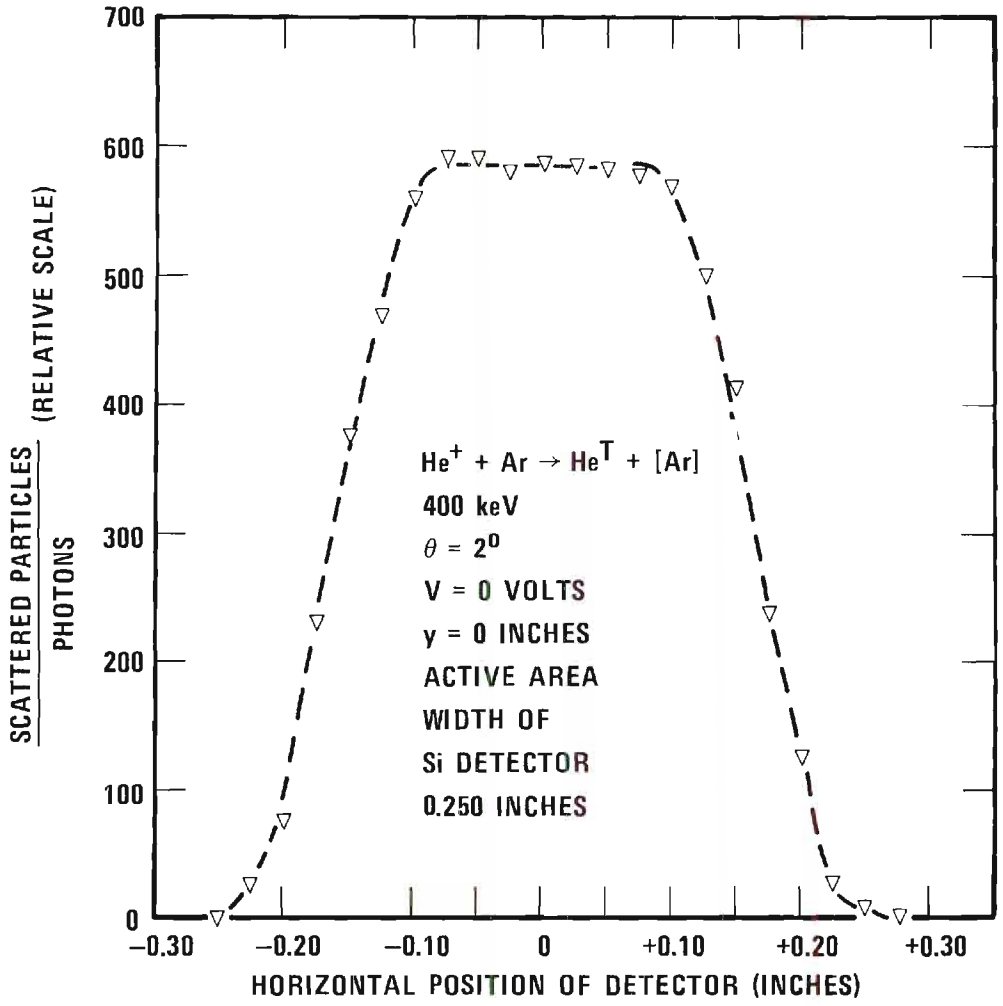

Figure 22. Horizontal Profile of Scattered Beam in Detector Plane.

The vertical positioning, however, was used extensively throughout the measurements (its motion was quite reproducible and dependable with no apparent backlash). Figure 23 shows the vertical profile of the beam measured with no deflection voltage. Shown on this diagram are measurements made at two different energies and two different scattering angles. The vertical spread of the beam was measured to be 0.090 inch for each of these different cases; a value in good agreement with geometrical estimates based on aperture sizes.

When a constant deflection field was applied, the He^{o}, He^{+}, and He^{2+} peaks not only appeared in the exact predicted location, but they also had the expected profiles. This agreement is shown both in Figures 18 and 19. Knowing the height of the beam at the detector, it is possible to predict (using equation (41)) for a given vertical position, the voltage necessary to bring each charge state onto the center of the detector, the width of the flat-topped peak for each charge state, and the voltage at which each of these charge states should begin to rise toward its peak as well as the voltage at which counts should cease. To verify these predictions, the detector was placed 0.40 inch above the neutral beam position and the deflection voltage varied to sweep various He peaks across its face. Figure 18 shows the excellent agreement between the predictions and the experiment.

A great deal of information is presented in Figure 18. On each peak is an arrow identifying the center of the peak and a set of limits showing the width of the plateau. Also included on this figure is a table showing the predicted center and width of the peak. Excellent agreement exists between the measured and the predicted values. These patterns

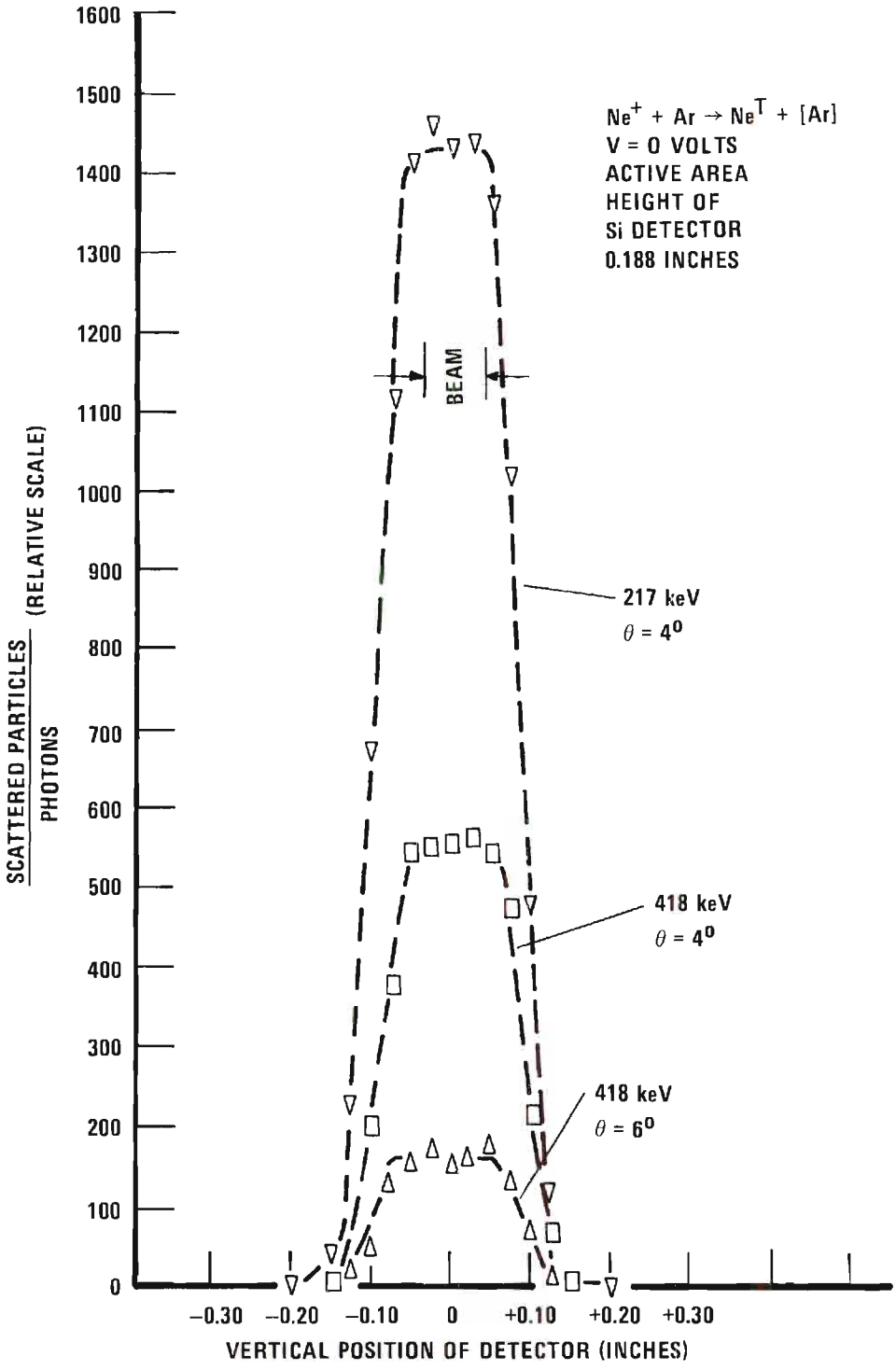

Figure 23. Vertical Profile of Scattered Beam in Detector Plane.

arise because the vertical extent of the beam is much less than the height of the shield aperture in front of the detector. Hence, the distribution changes from zero as the charge state component first strikes the detector, rising to the plateau when the entire beam is striking the detector. The plateau value is maintained as the beam is swept across the face of the detector. The observed count rate falls from the plateau value as the leading edge of the beam is intercepted by the shield, reaching zero when the trailing edge of the beam is intercepted by the shield.

Therefore, it is concluded from (1) the shape of the pulse height spectrum, (2) the agreement between the measured and predicted horizontal distribution, (3) the agreement between the measured and predicted height of the beam of scattered particles, and (4) the excellent agreement between the prediction and the observed vertical position and shape of the scattered beam when deflected that this analyzer system (1) detects all atoms or ions, and (2) determines the charge, for all particles scattered through angle θ into the solid angle $d\omega$ with 100 percent efficiency. The pulse-height spectrum is clear indication that there are no large energy losses. The sensitivity to energy loss of the apparatus is such that it is only possible to assert an upper limit to the energy loss of less than 15 percent.

Measurement and Monitoring of Projectile Beam

The beam current was measured with a Faraday cup which could either be placed in the beam path or removed from the beam, by means of a bellows-sealed actuator which has been previously described in the discussion of the collision chamber. Continuous monitoring of the beam was accomplished by counting photons emitted from collisionally excited target atoms. Two

quartz lenses focused these photons on the photocathode of an E.M.I. #6256S tube. An all-quartz system was employed to extend the range of wavelengths which could reach the multiplier since argon, as well as the other target gases used, has emissions in the ultraviolet as well as the visible range.[77,78]

During the first part of the measurements, only a single glass lens had been employed at the position closest to the multiplier tube. By adding the second lens, to increase the solid angle focused on the tube, and by using an all-quartz system, to extend into the ultraviolet range, the photon counting rate for given beam intensity and gas pressure was increased almost an order of magnitude.

Pumping ports were provided so that the region above the first lens was at the same vacuum as the collision chamber. The vacuum seal was formed by the second lens. A cross section view, Figure 8, shows the position of both lenses. Both lenses were plano-convex lenses; the lens in the collision chamber had a focal length of 64.7 mm while the top lens had a focal length of 124.8 mm. The beam in the collision region is at the focal point of the first lens; light emitted into the solid angle subtended by this lens is thus collimated into a parallel beam of light. This light is in turn focused onto the photocathode of the photomultiplier which is located at the focal point of the second lens.

Techniques of Measurement

As shown in Chapter II, the differential scattering cross section is given by the relation

$$\frac{d\sigma^n(\theta)}{d\omega} = \frac{N^n(\theta)}{N_o} \frac{1}{N_t} \frac{1}{G(\theta)} \quad . \tag{15}$$

To measure this cross section it is necessary to measure only three items: (1) the ratio of the number of particles of charge n scattered into $d\omega$ at angle θ to the number of incident projectiles, i.e., $\frac{N^n(\theta)}{N_o}$; (2) the target density, N_t, which is experimentally determined by measuring the target pressure and the temperature; and (3) the geometrical factor $G(\theta)$.

We have described in this chapter the various detectors which were used during these investigations; now, it is necessary to consider how they were actually employed in conjunction with one another to experimentally determine the differential scattering cross section.

There were two distinct phases of the measurements and they shall be considered in their chronological order, the difference in these phases being due to the change from an ionization gauge to a capacitance manometer for measuring the target pressure.

The analyzer determined $N^n(\theta)$. Actually, as described in the "analyzer system" section of this chapter, the detector determined the count rate of scattered particles; the position of the detector in conjunction with the voltage applied to the deflection plates determined the electrical charge of the particles being counted. Thus, N^o, N^+, N^{2+}, and N^T (N^T is the total number of scattered particles of all charge states) were counted, and it was verified that $N^S = N^T$ (within counting statistics) where

$$N^S = N^o + N^+ + N^{2+} \quad .$$

The measurement of scattering angle was dependent on the mechanical

construction. The scale was such that it could be read to an accuracy better than two and one-half minutes.

The ratio of the count rates $N^n(\theta)/N_o$ could not be measured directly since $N^n(\theta)$ and the incident beam intensity $I_o = eN_o$ could not be measured simultaneously, as explained previously. Here, e is the charge of the incident ions (the electron charge for He^+). For this reason, the intermediate step was introduced of observing the collisionally induced excitation of the target gas. The excitation photon count rate N_p could be counted simultaneously with the counting of $N^n(\theta)$, and it served as a continuous monitor and integrator of the incident beam; i.e., it provided an indirect measurement of N_o.

Calibration of the relation between N_o and the photon count rate will be discussed presently. Associated with the photomultiplier was a constant background count rate, n_{TN}, due to thermal noise. Thus the "true" photon count was $(N_p - n_{TN})$. (A fraction of the true count rate was in principle contributed by excitation of the residual background gas in the collision chamber, but this fraction was always less than one percent and was neglected.)

Thus the quantities directly measured for each data point provided the ratio $N^n(\theta)/(N_p - n_{TN})$. Calibration of the ratio $(N_p - n_{TN})/N_o$ was performed in two somewhat different fashions during the two phases of the measurements mentioned above, for reasons contained in the discussion to follow.

During the first phase (the November 1968 data), an ionization gauge provided the only measurement of the target gas pressure. The absolute accuracy of the cross section measurement was therefore no better

than the nominal calibration of the gauge, and even the relative measurements tended to suffer from some of the well known vagaries of ionization gauges. An additional difficulty arose from the fact that the gauge could not be operated simultaneously with the photon counting, because light from the gauge was reflected inside the collision chamber into the photomultiplier. The procedures followed in these measurements were designed to reduce the relative uncertainties as much as possible, with the intention of normalizing the data according to a later absolute calibration of the ionization gauge.

Great care was taken always to read the gauge under exactly reproducible conditions. In addition, the calibration of the ratio $(N_p - n_{TN})/N_o$ was carried out over as wide a range of target gas pressure as feasible. At each pressure, the photon count rate N_p was counted, and the projectile current I_o was measured with an electrometer, by collecting the beam into the Faraday cup in the collision chamber. (As previously described, these measurements could not be performed simultaneously. They were always performed alternately several times, until a reliable average value of their ratio was obtained.) In this manner, an average value of the ratio $(N_p - n_{TN})/I_o$ was computed for the given pressure. The values of this ratio for different pressures were then plotted against the pressure, in Torr, as measured by the ionization gauge, and a straight line through the origin was fitted to the points by the method of least squares. Figure 24 is such a calibration graph. The slope, γ, of this line then represented the quantity

$$\gamma = \frac{(N_p - n_{TN})}{I_o} \frac{1}{P}$$

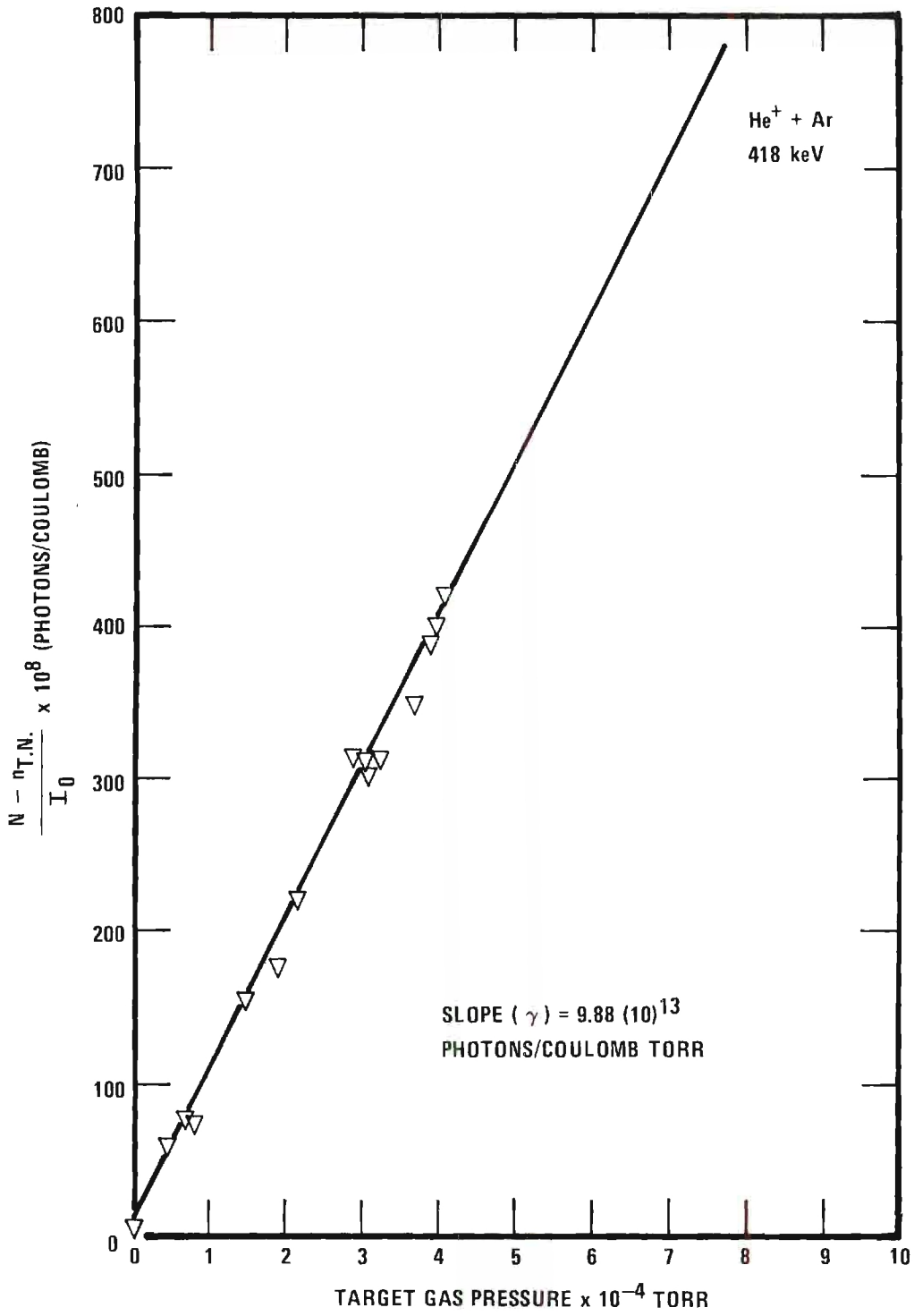

Figure 24. Calibration of Photon Count Rate Against Projectile Beam Using Ionization Gauge.

Such graphs were obtained repeatedly over the course of several days, and the average value of γ obtained for a particular beam energy was subsequently used for all data at that energy.

In terms of the measured quantities in the first phase of the measurements (the November 1968 data), the cross section (15) was, therefore,

$$\frac{d\sigma^n(\theta)}{d\omega} = \frac{N^n(\theta)}{(N_p - n_{TN})} e\gamma \frac{1}{L'} \frac{T}{T_o} \frac{1}{G(\theta)} \qquad (42a)$$

where L' is the number density of a gas at standard temperature T_o and a pressure of one Torr, and T is the temperature of the target gas.

During the later phase of the measurements (1969 data), a capacitance manometer was used for measurement of the target gas pressure. In addition to having a much more reliable absolute calibration than the ionization gauge (the calibration is discussed in Appendix B), this instrument provided a much more stable pressure reading, and it could also be read simultaneously with the photon count. (As previously explained, its output was digitized through the use of a V-F converter whose output was counted by a scaler, which effects an integration of the pressure reading over the same time interval as the photon count.) These factors permitted some simplification in the calibration of the ratio $(N_p - n_{TN})/N_o$. As before, the photon count and the measurement of the incident beam intensity had to be performed alternately several times, at a constant gas pressure, to obtain an average value of the ratio

$$\gamma' = \frac{N_p - n_{TN}}{I_o} .$$

However, the former step of obtaining this ratio at a number of pressures and plotting against the pressure to obtain an average slope was no longer found to be necessary. Single measurements of γ' now proved to be quite reliable, due partly to the better performance of the capacitance manometer and partly to the fact that a coincidental improvement in the optics of the photon counter had increased the photon count rates by an order of magnitude. γ' was measured at least once every day and was remeasured whenever the pressure was changed or was found to have drifted.

Thus, in terms of the quantities measured in the latter phase of the measurements (the 1969 data), the cross section (15) was given by

$$\frac{d\sigma^n}{d\omega}(\theta) = \frac{N^n(\theta)}{N_p - n_{TN}} e\gamma' \frac{1}{N_t} \frac{1}{G(\theta)} \qquad (42b)$$

The measured cross sections obtained when using the capacitance manometer were some 20 percent higher than those previously obtained when only the ionization gauge was available. This much difference could easily be attributed to the absolute uncertainties in the ionization gauge, particularly since the gauge was used on its highest range where it was observed to have two distinctly different modes of operation differing in scale reading by about a factor of two. To conclusively lay this difference to the ionization gauge, it would have been desirable to calibrate the gauge directly against the capacitance manometer. Unfortunately, the ionization gauge which had been used in the work was accidently broken before more than a very preliminary comparison had been completed. Thus, the direct evidence is inconclusive; but, the calibration of the capacitance manometer, plus its inherently more stable operation and its con-

tinuous operation (opposed to the infrequent "look" with the ionization gauge) led us to place full confidence in the cross section measured using the capacitance manometer. For this reason, the data taken early in the program were normalized to the latter data. Relative measurements with the ionization gauge are much better than the absolute measurements, so that the data taken when employing the ionization gauge were useable with a single normalization. Only Ar data were taken in this fashion and normalized to later data also using an Ar target.

The geometrical factor, $G(\theta)$, was evaluated using equation (57). As shown in Appendix A, an excellent approximation to it is given by

$$G(\theta) \simeq \frac{a\ b\ h}{d(d + \ell)} \frac{1}{\sin \theta} \tag{59}$$

Exact knowledge of the aperture sizes was crucial to assigning absolute magnitudes to the measured cross sections. This is readily seen in the fact that b and h were nominally machined to be 0.010 inch; however, the actual sizes, while within less than one thousandth of an inch of the specified sizes, introduced a 14 percent error into the calculations until the correct sizes were substituted for design sizes. The actual sizes were determined to within plus or minus two percent by a two-dimensional traveling microscope and also by measuring the diffraction patterns produced when a laser beam is passed through the apertures. These two very different methods agreed within the assigned errors. The best values obtained for the sizes of the apertures were as follows:

a = 0.0132 inch (used in November 1968 data)

a = 0.0156 inch (used in 1969 data)

b = 0.0091 inch

h = 0.0095 inch

Errors in Measurement

The experimental differential scattering cross section is evaluated by

$$\frac{d\sigma^n}{d\omega}(\theta) = \frac{N^n(\theta)}{N_o} \frac{1}{N_t} \frac{1}{G(\theta)} . \qquad (15)$$

As shown in the previous section, the cross section was actually computed from

$$\frac{d\sigma^n}{d\omega}(\theta) = \frac{N^n(\theta)}{N_p - n_{TN}} e\gamma' \frac{1}{N_t} \frac{1}{G(\theta)} . \qquad (42b)$$

It is necessary to consider the errors associated with the measurement of each of the quantities in this equation.

Counting statistics determines the error introduced in measuring the number of scattered particles, N^n. Let the possible error associated with a counted number of particles be represented by one standard deviation which is approximately equal to the square root of the number counted.[79] Thus, if a scaler records only 100 scattered particles, the probable error associated with this count would be ± 10 counts and would contribute a probable error of ± 10 percent to the cross section calculated by equation (42b). Table 5 shows some typical errors introduced from this source for argon and helium targets at the various energies investigated. As can be seen in Table 5, this error is small at small angles, but it becomes appreciable at larger angles. The smallest cross section in each case (i.e., the cross section for either the charge transfer or electron stripping) suffers most from counting statistics.

The statistical error introduced by counting the photons was ap-

Table 5. Typical Values for Statistical Errors

θ	$d\sigma^+/d\omega$	$d\sigma^{2+}/d\omega$	$d\sigma^o/d\omega$	$d\sigma^T/d\omega$
$He^+ + Ar$				
E = 208 keV				
50'	0.4	0.9	0.5	0.3
2°	1.5	3.6	2.1	1.2
4°	5.4	12.4	7.7	4.1
7°30'	5.8	11.2	7.6	4.1
E = 418 keV				
1°	0.5	0.6	1.3	0.4
4°	2.7	3.5	7.6	2.0
6°	3.5	4.8	9.5	2.7
8°	7.3	9.3	21.1	5.5
E = 627 keV				
35'	0.2	0.2	1.2	0.2
2°30'	1.7	1.5	12.6	1.1
4°	5.4	4.9	19.0	3.5
6°	6.2	5.0	28.8	3.9
$He^+ + He$				
E = 400 keV				
1°35'	1.4	3.2	2.1	1.1
3°	5.2	8.2	7.3	
5°	9.1	21.5	12.8	7.1
E = 600 keV				
1°35'	1.8	3.0	3.9	1.4
3°35'	6.2	11.3	14.4	5.0

proximately plus or minus two percent in the worst situation. The counting time varied over wide limits, from a few seconds to several minutes which in turn caused a spread in the error assigned to $N_p - n_{TN}$. The error in measuring this quantity, $N_p - n_{TN}$, is estimated to be plus or minus three percent. This is from worst case consideration.

γ' is the ratio of the photon count rate to the beam current. The maximum possible random error associated with this ratio is estimated to be plus or minus two percent at 400 keV incident energy and plus or minus three percent at 600 keV incident energy. These errors were assigned from the spread of the observed ratios about the mean value. They were the same for all target gases. This ratio could also introduce a possible systematic error of plus or minus three percent from use of the Keithley micro-microammeter.

The target density was determined by measuring the target gas pressure and the room temperature. The random error in reading the capacitance manometer was estimated to be plus or minus two percent. A possible systematic error of plus or minus five percent could have been introduced through the calibration of the capacitance manometer (see Appendix B). The error arising from the room temperature measurement was negligible.

The geometrical factor was the source of the largest of the systematic errors in the cross sections. As shown in Appendix A

$$G(\theta) \simeq \frac{a\ b\ h}{d(d + \ell)} \frac{1}{\sin \theta} . \qquad (59)$$

Aperture dimensions a, b, and h were measured to within ± 2 percent; the denominator, $d(d + \ell)$, was also known to within ± 2 percent. Hence, the

possible systematic error in $G(\theta)$ from these measurements was ± 8 percent.

A random error in $G(\theta)$ comes from the measurement of the scattering angle, θ. It was possible to determine the angle to within two and one-half minutes. At a scattering angle of one degree, the possible error in $\sin \theta$ is four percent; however, this error decreases rapidly with increasing θ.

Considering the random errors involved in the measurement of each of these quantities, the differential scattering cross sections have a random error of ± 8 percent plus the statistical error from Table 5. The possible systematic error associated with these data is approximately ± 13 percent.

He^+ + Ar with an incident energy of 418 keV was the pilot case in these measurements; the data accumulated for this case were far more extensive than for the other cases measured. Most data points shown in Figure 26 represent the average of many separate measurements, a few points being the average of 20 or more values. The individual points had a distribution of less than ± 10 percent about the mean value in almost all cases. When the mean values for the total differential scattering cross sections were plotted as a function of angle (Figure 26), the spread about a smooth curve was approximately ± 10 percent. The spread about a smooth curve for the charge transfer differential scattering cross section was 12 to 15 percent. Thus, the best estimate of the relative error for the total differential scattering cross section is ± 10 percent which is consistent with the previous estimate of the random error from consideration of the individual measurements which were performed.

The absolute error assigned to the total differential scattering

cross sections is ± 23 percent. In all cases measured the experimental and theoretical values differed by less than 23 percent.

If the ratio N^n/N^T could be counted simultaneously, the random error in P_n would arise solely from counting statistics. However, since the counting must be sequentially performed, the random error in P_n should be the sum of the random errors in measuring $d\sigma^n/d\omega$ and $d\sigma^T/d\omega$. For the P_n versus θ curves (Figures 33 through 37), the scatter about the mean is always less than the predicted random error, and, as expected, the fractional error increases for smaller values of P_n. The random error associated with the P_n versus energy curves (Figures 38 through 40) depends on the energy and the particular charge state fraction being considered. The spread of the data about a smooth curve is the best estimate of the error, being generally less than ± 10 percent.

CHAPTER V

EXPERIMENTAL RESULTS

The measured differential scattering cross sections as a function of angle at fixed energy are displayed graphically. The total differential scattering cross section agrees, within experimental error, with a classical theoretical calculation, assuming a Bohr potential. P_n, the fraction of scattered projectiles in charge state n, is shown as a function of both angle and energy. These data are compared with other measurements and with available theories.

During the course of the measurements, it proved necessary to completely realign the scattering geometry. The measurements before and after this realignment were in complete agreement, which provided a good consistency check on the data.

Differential Scattering Cross Sections

Figures 25 through 30 show the experimentally determined differential scattering cross sections plotted as a function of scattering angle for several fixed energies for the target gases Ar, He, and Ne. Each figure contains the total differential scattering cross section which is the sum of the differential scattering cross section for charge transfer, for electron stripping, and for scattering without change of charge. These three individual differential scattering cross sections are also displayed on each graph. In each case the total differential scattering cross section was directly measured (by counting all particles scattered

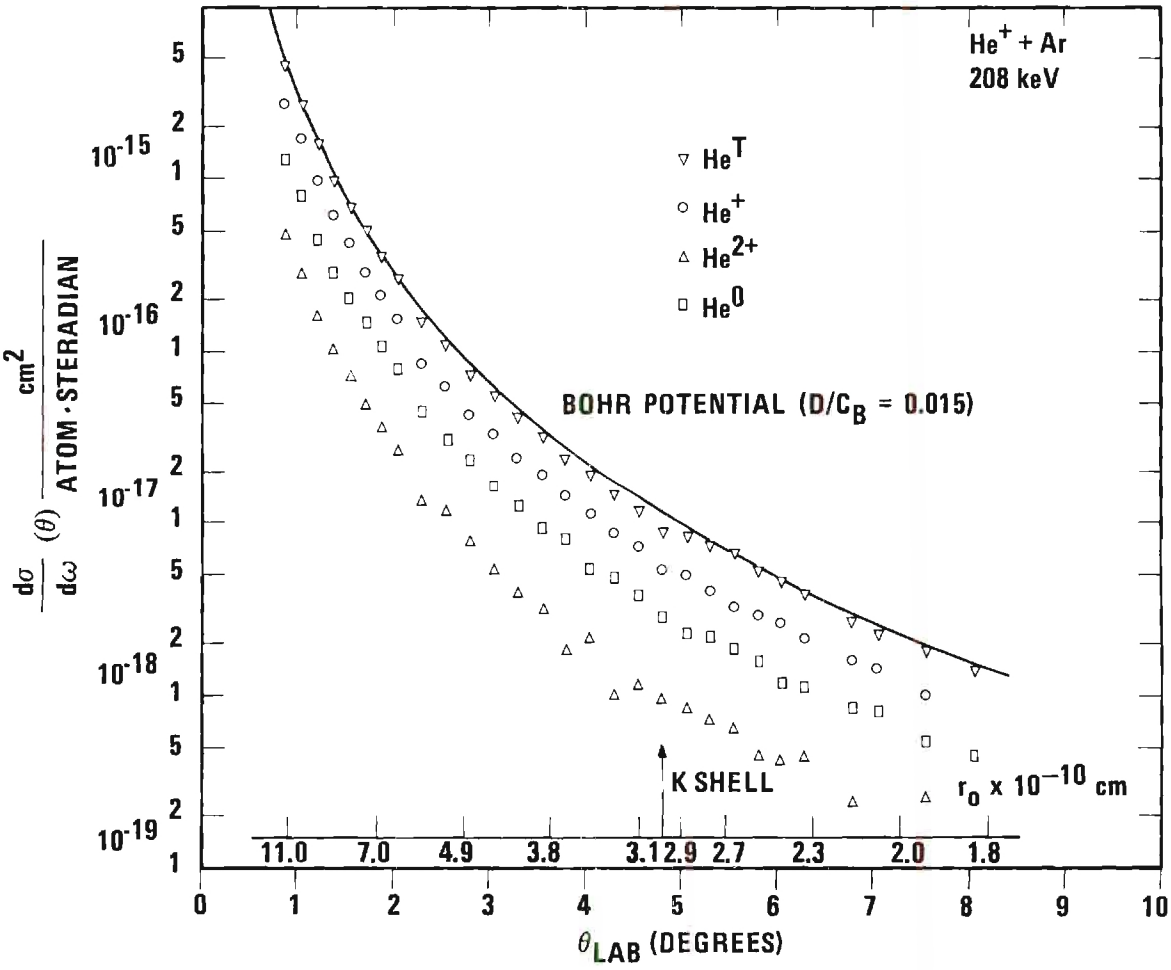

Figure 25. Differential Scattering Cross Sections Versus Angle for He^+ + Ar with Incident Energy of 208 keV.

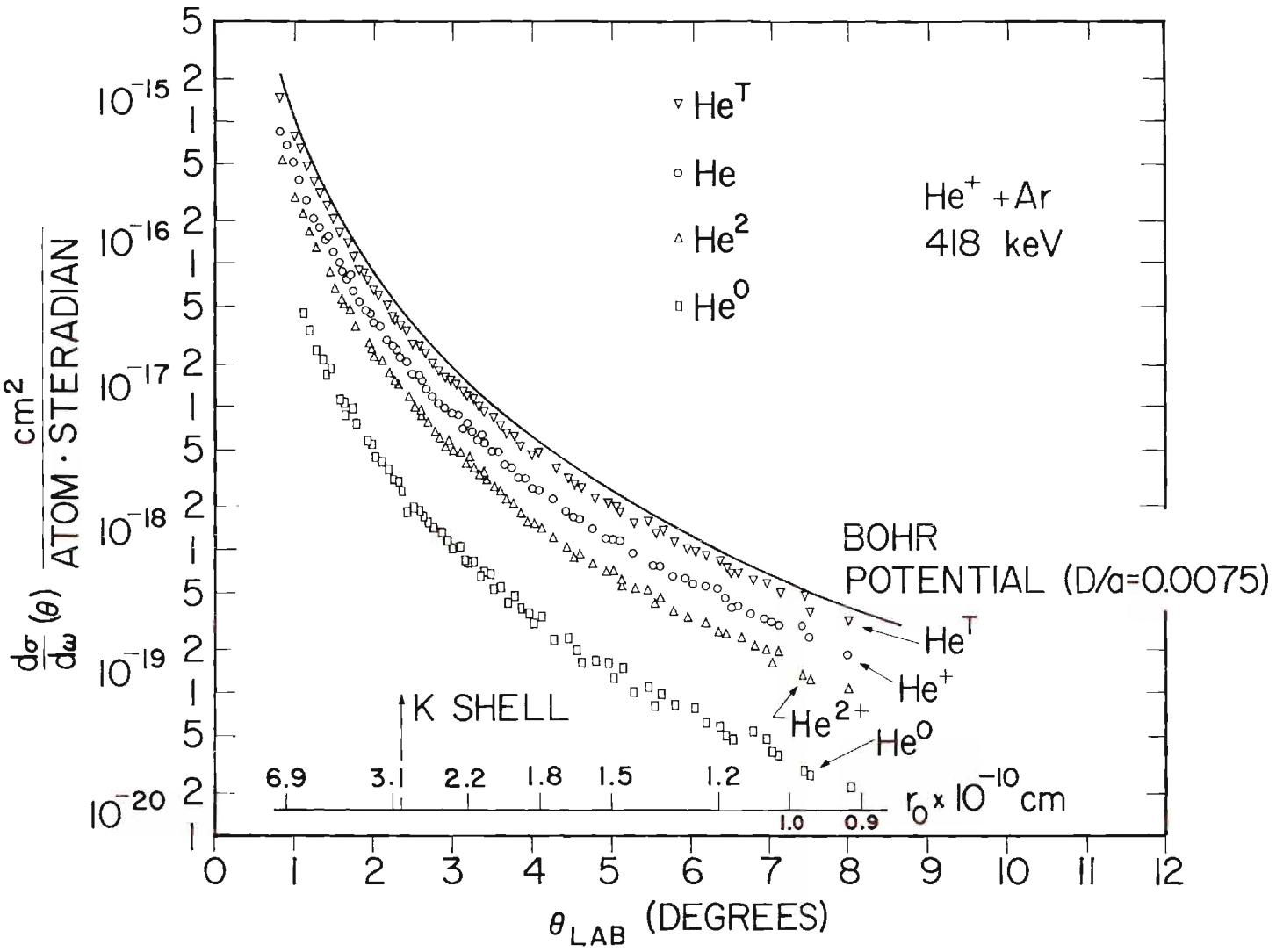

Figure 26. Differential Scattering Cross Sections Versus Angle for He^+ + Ar with Incident Energy of 418 keV.

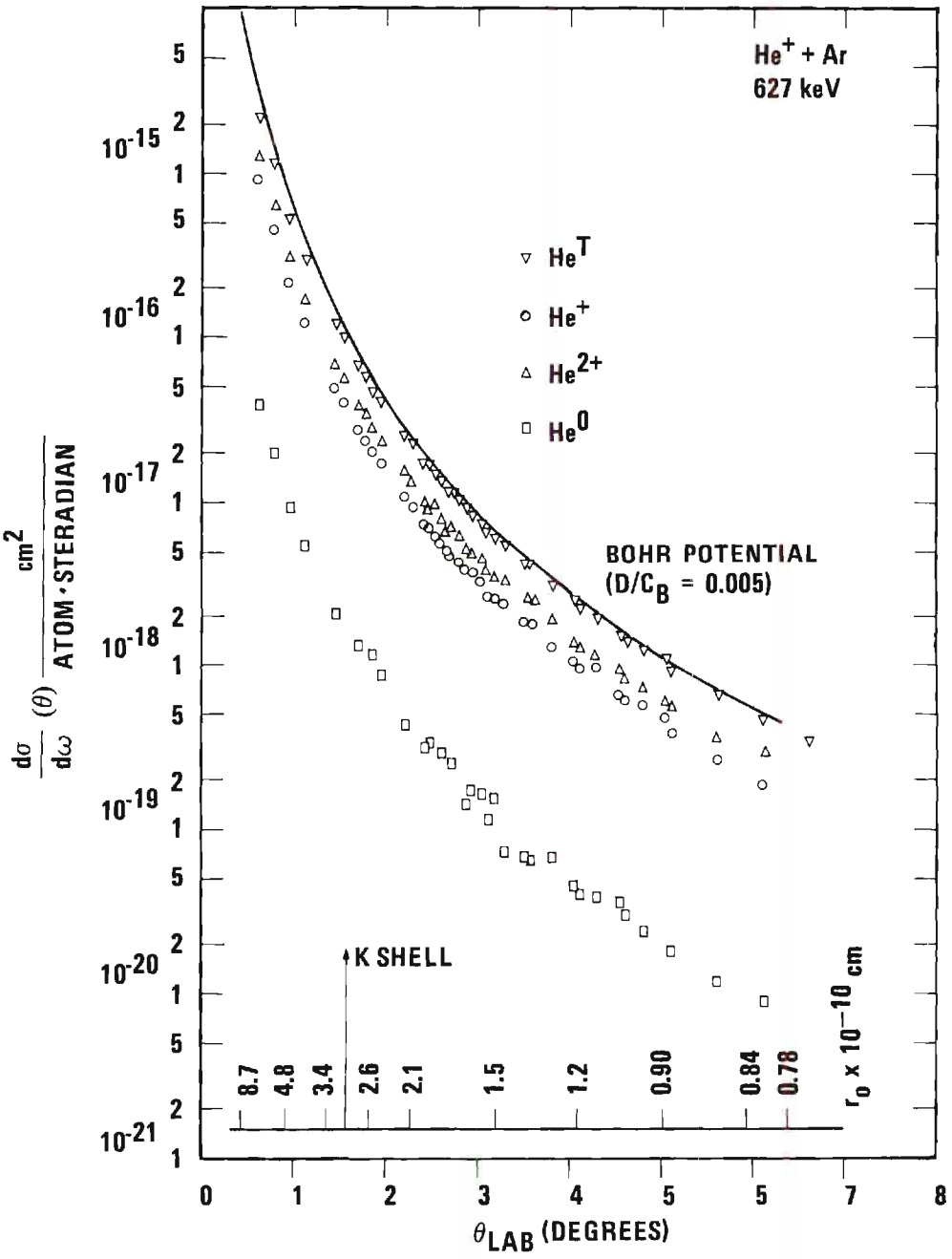

Figure 27. Differential Scattering Cross Sections Versus Angle for He^+ + Ar with Incident Energy of 627 keV.

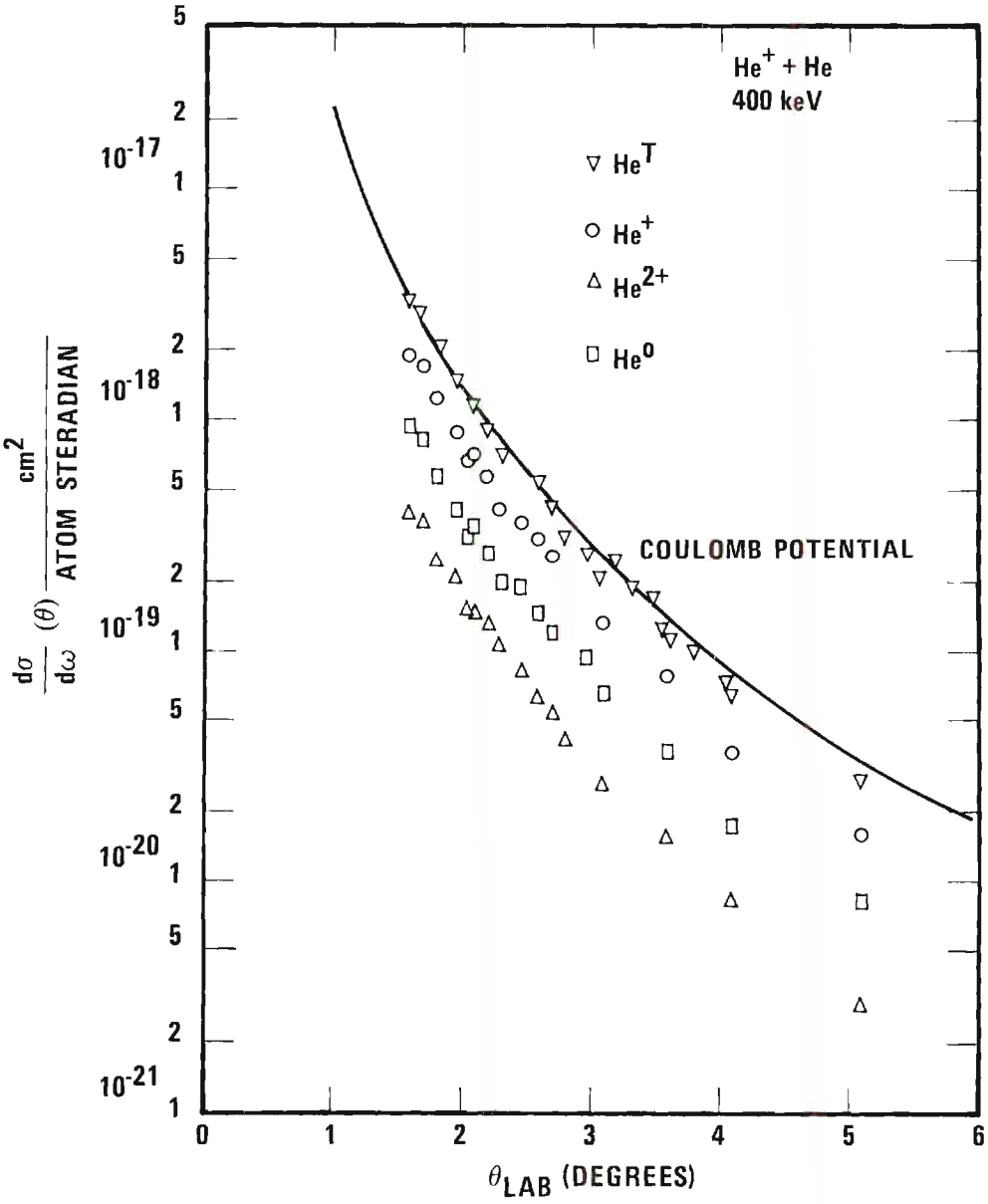

Figure 28. Differential Scattering Cross Sections Versus Angle for He^+ + He with Incident Energy of 400 keV.

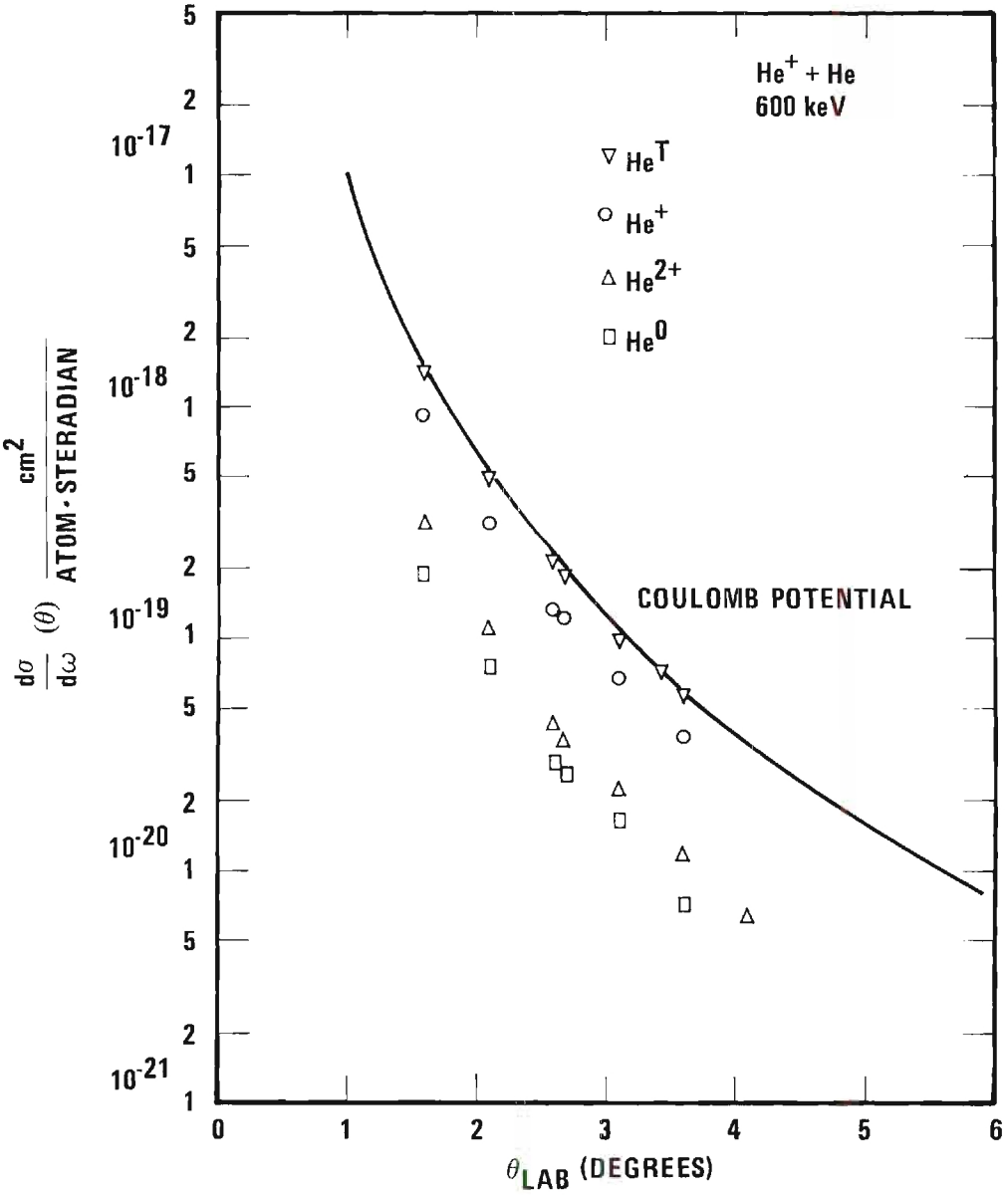

Figure 29. Differential Scattering Cross Sections Versus Angle for He^+ + He with Incident Energy of 600 keV.

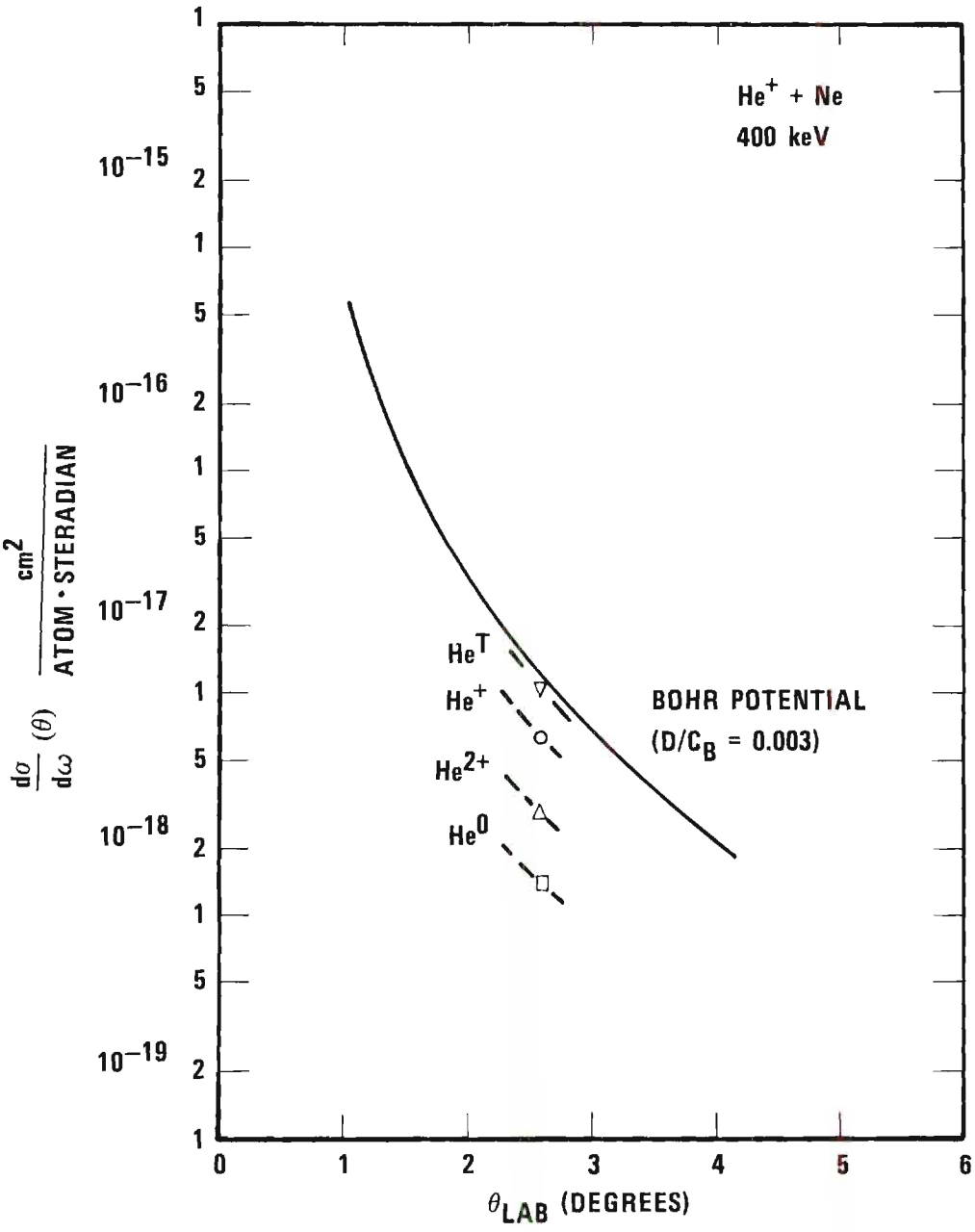

Figure 30. Differential Scattering Cross Sections Versus Angle for He^+ + Ne with Incident Energy of 400 keV.

into solid angle $d\omega$ at angle θ irrespective of their charge state) and compared with the sum; the measured total agreed with the sum of the individual cross sections within counting statistics in every case.

The data were accumulated over a period of seven months. During this time, several important additions were made to the apparatus, the most important being the capacitance manometer. With the capacitance manometer an accurate absolute measurement of the target gas pressure was made. Cross sections measured prior to the time of using this instrument (i.e., data taken in November and December, 1968) were normalized to later measurements. This normalization shifted all of the data taken in November and December of 1968 by a uniform 20 percent. Only Ar data were accumulated during this time period.

Figures 25, 26, and 27 show the cross sections as a function of scattering angle θ for He^+ ions incident on argon atoms at 208, 418, and 627 keV, respectively. There is excellent agreement between the shapes of the measured curves and the theoretical curve based on a classical calculation using a Bohr potential, equation (23). The shielding factor, D/c_B, is shown on each individual graph. The values of the theoretical cross sections were taken from the tabulation of Bingham.[36] It is equally interesting that the sum of the three cross sections,

$$\frac{d\sigma^T}{d\omega} = \frac{d\sigma^+}{d\omega} + \frac{d\sigma^{2+}}{d\omega} + \frac{d\sigma^0}{d\omega}$$

agrees absolutely (within experimental error) with the theoretical curve.

The theoretical differential scattering cross section based on a classical calculation using a Bohr potential is valid for elastic colli-

sions. The present measurements could not distinguish elastic from inelastic collisions. Although $\frac{d\sigma^+}{d\omega}$ did contain all the elastic scattering events, it also contained all inelastic events in which the projectile did not change its electrical charge. $\frac{d\sigma^T}{d\omega}$ contained all elastic plus all the inelastic events. But, reported measurements[11,12] indicate that the inelastic energy loss in high energy heavy body collisions is small when the fast particle undergoes appreciable scatter so that $\frac{d\sigma^T}{d\omega}$ can be considered as "almost" or "quasi-" elastic. From these considerations it was not obvious a priori whether the theoretical curve should compare with $\frac{d\sigma^+}{d\omega}$, with $\frac{d\sigma^T}{d\omega}$, or possibly with neither.

As the data, Figures 25 through 30, clearly demonstrate, $\frac{d\sigma^T}{d\omega}$ agrees with the theoretical curve within the experimental errors. The good agreement between these curves indicates that the scattering is governed by the nuclear-nuclear force and is independent of the final arrangement of the electrons after the collision. Also, the agreement confirms Smith's[35] contention that such high energy collisions can be considered as "quasi-elastic." Additionally, it suggests that the inelastic energy loss under these conditions must be very small, which confirms measurements from other laboratories.

The area under the total differential scattering curves is proportional to the "total cross sections" for the particular process, i.e.,

$$\sigma^{\text{stripping}}(E) = 2\pi \int_0^{\pi} \frac{d\sigma^{2+}}{d\omega}(\theta,E) \sin\theta \, d\theta$$

and

$$\sigma^{\text{transfer}}(E) = 2\pi \int_0^{\pi} \frac{d\sigma^{0}}{d\omega}(\theta,E) \sin\theta \, d\theta \, .$$

These total cross sections have been measured experimentally[80, 81, 82, 83] and theoretical[84, 85] calculations on some collision combinations have been made. It would be very interesting to compare the present measurements with these other works. However, Jones, et al.[83] have shown that greater than 99 percent of these total cross sections comes from collisions where the scattering was less than one degree. Thus, the area under the experimental differential scattering curves amounts to roughly only one percent of the total cross section for the given process. This was confirmed in a single case by comparing the area under the charge changing cross section with the experimental value[83] of $\sigma^{transfer}$. Hence, this comparison was not pursued.

The scattering force can be represented by the interaction potential

$$U(r) = \frac{Z_1 Z_2 e^2}{r} e^{-r/c_B} \qquad (23)$$

The effect of the screening factor (the exponential factor) becomes negligibly small when the scattering angle is greater than a few degrees. In Figure 31 is plotted, as was suggested by Smith,[35] a "reduced cross section" $\rho = \Theta \sin \Theta \frac{d\sigma}{d\Omega}(\Theta)$ as a function of the product $\tau = \Theta E_{cm}$. The advantage of this presentation of the data is that it combines the differential cross section for all angles and energies into a single graph; i.e., it shows the total differential scattering cross sections contained in Figures 25, 26, and 27. Also, the theoretical cross sections based on both the Coulomb and the Bohr potentials are shown. Notice that the two theoretical curves separate only below 8×10^5 eV degrees. This is equivalent to a scattering angle in the laboratory of approximately three

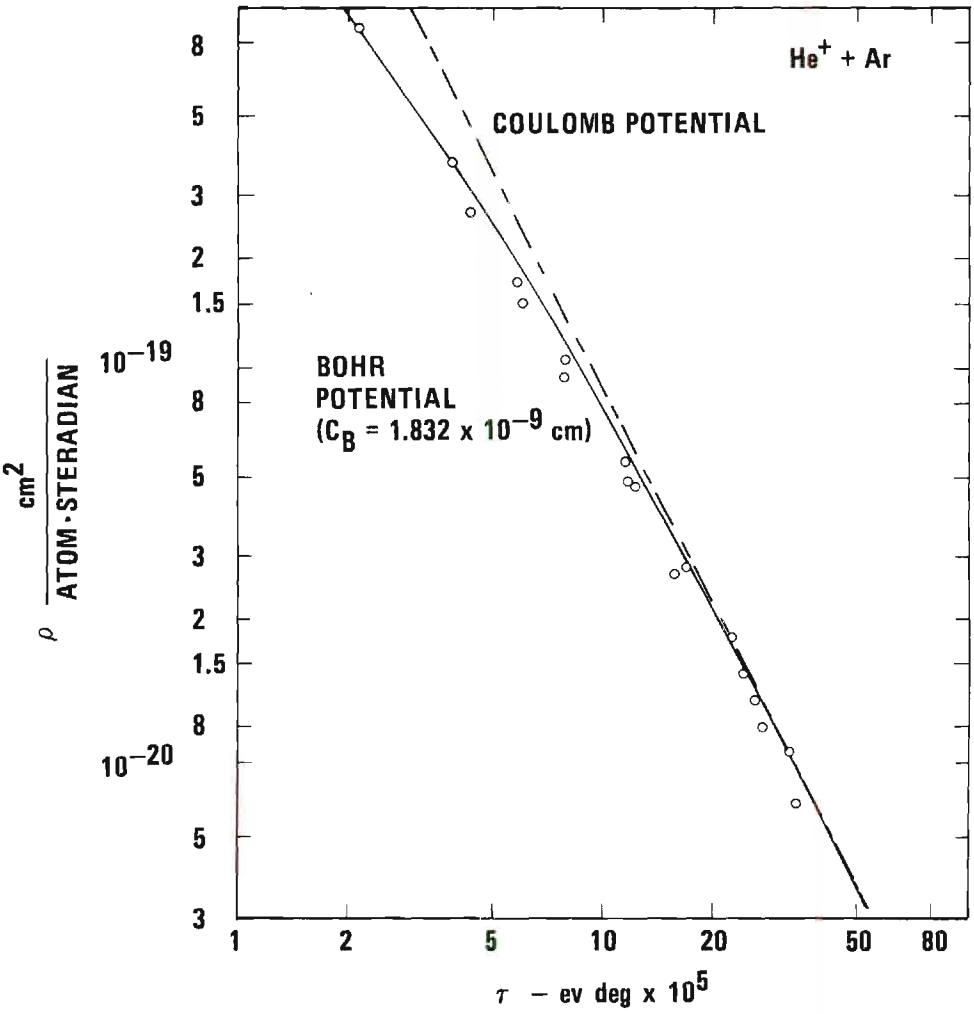

Figure 31. Reduced Cross Sections for Scattering of He^+ + Ar.

degrees 45 minutes when E = 208 keV, two degrees 15 minutes when E = 418 keV, and one degree zero minutes when E = 627 keV. Outside these angular limits, the "pure" Coulomb force between the two nuclei essentially governs the scattering.

The experimental data for He^+ + He are compared with the differential cross section curve for the pure Coulomb potential (Figures 28 and 29). The screening constant, D/c_B, is extremely small, indicating that the electron shielding is negligible for this case. The agreement between experiment and theory is very good. Only one point was measured for He^+ + Ne (Figure 30). As in the other cases, the total differential scattering cross section agrees with the calculated value.

Fuls, et al.[8] measured the total differential scattering cross section for He^+ incident on the same target gases as were investigated in the present measurement for incident energies between 25 and 100 keV. His results also agreed with the cross sections computed using the screened Coulomb potential.

Figure 32 shows the differential scattering cross sections at fixed angle for all charge changing processes measured as a function of energy. Also shown are the results of Fuls, et al.[8] for energies down to 25 keV, and the theoretical curves predicted classically from both the screened (Born) and the "pure" Coulomb potentials. Figure 32 shows that the differential scattering cross section for charge transfer falls off very rapidly, approximately as v^{-5}. The Born approximation for the "total" charge transfer cross section (i.e., $\sigma(E)$) predicts a v^{-12} dependence on impact velocity; however, various experimental measurements[86] have shown an extremely wide range in this velocity dependence, from $v^{-3.7}$ to v^{-10}.

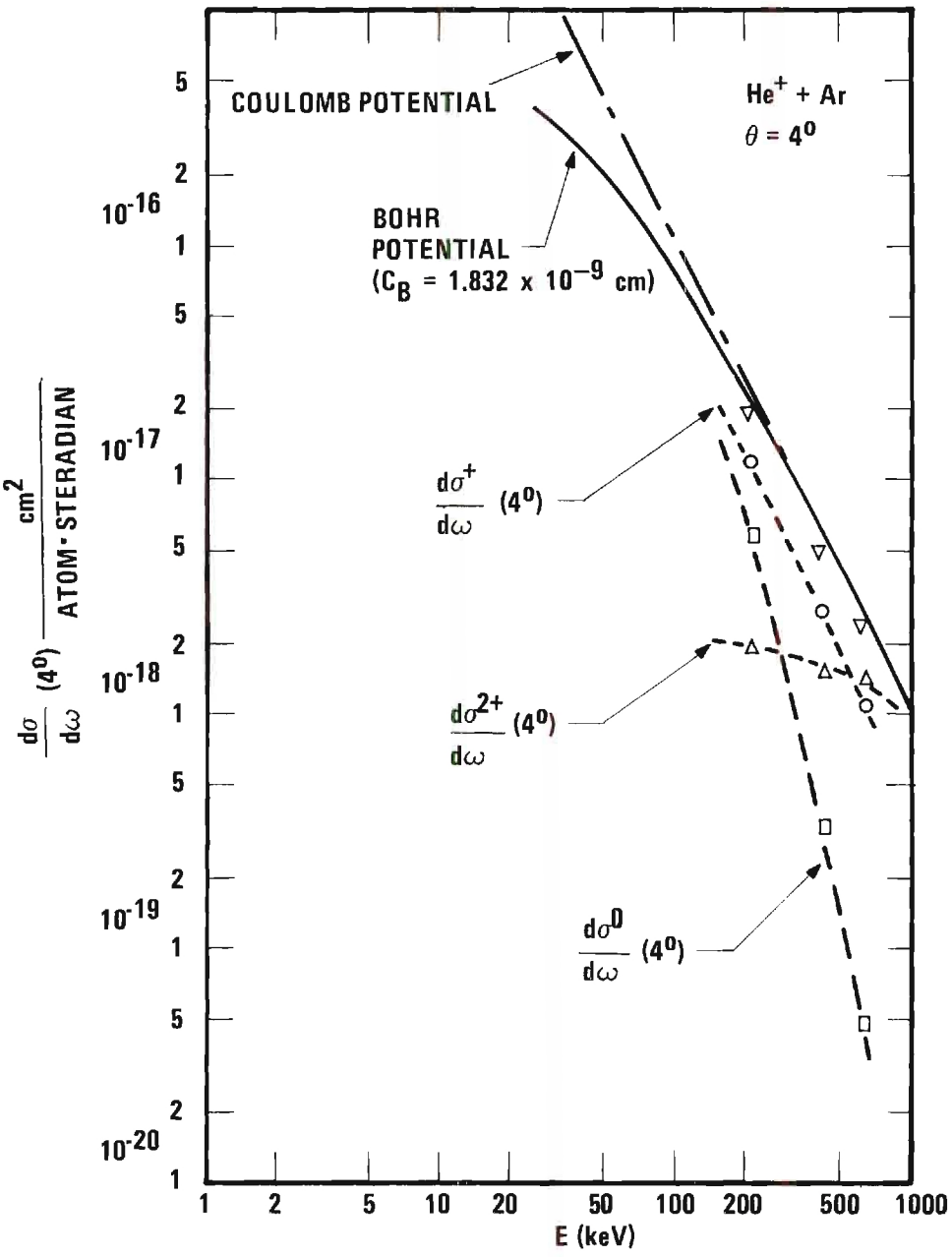

Figure 32. Differential Scattering Cross Sections Versus Energy for He^+ + Ar at a Scattering Angle of 4°.

From 200 to 600 keV the differential scattering cross section for electron stripping shows a velocity dependence approximately equal to $v^{-0.5}$; however, from 600 to 800 keV the velocity dependence of this cross section changes rapidly apparently approaching a v^{-2} dependence. This velocity dependence is similar to reported total loss cross sections.[86]

It is very interesting that these differential cross sections show an energy dependence similar to the total cross sections for charge transfer and stripping. Remembering that the total cross section is the integral of the differential scattering cross section, i.e.,

$$\sigma(E) = 2\pi \int_0^{\pi} \frac{d\sigma}{d\omega} (\theta,E) \sin \theta \, d\theta \ ,$$

one would not expect a priori that $\frac{d\sigma}{d\omega}$ and σ would necessarily show the same energy dependence.

Results using the Born approximation have not been published for differential scattering cross sections. As the higher energies in the present experiment are in the region where the Born approximations should be applicable, such a comparison would be very interesting.

A "distance of closest approach" scale has also been included in Figures 25, 26, and 27. These distances were taken from tabulated values[36] computed classically for the Born potential. Also on this scale is found the radius of the K shell of argon. (This K shell radius is based on the ionization potential.[20]) The data in these figures were closely examined for any evidence of structure in the curves, especially near the K shell radius. Figure 25 shows suspicious behavior when $r_o \simeq 2.9 \times 10^{-10}$ cm, a separation distance of approximately the K shell radius. However, this

feature is not seen at higher projectile energies, even though the data span the $r = 2.9 \times 10^{-10}$ cm region. Hence, it must be concluded that slight fluctuations in Figure 25 are probably not significant. Based on the accuracy of these measurements, if any anomalies giving rise to structure in the differential scattering curves exist within the investigated energy and angular ranges, they deviate from a smooth curve by less than 12 percent.

Charge State Fractions

Angular Dependence

Figures 33 through 37 show the fraction, P_n, of charge states, n, as a function of scattering angle, θ.

$$P_n(\theta) = \frac{N^n(\theta)}{N^T(\theta)} \qquad (17)$$

These figures show that P_n has no dependence on the scattering angle within the range of conditions investigated. This fact is consistent with Russek's prediction for the high energy behavior of P_0. Angular independence of P_n has been reported at 100 keV, also at 50 keV when $\theta \geq 4$ degrees.[8,87]

Energy Dependence

Figures 38, 39, and 40 display the energy dependence of P_n. The data in these graphs are presented in tabular form in Tables 6, 7, and 8. As P_n has no angular dependence under the conditions investigated, these curves were measured at several angles. The particular angles were chosen to minimize errors due to counting statistics, while at the same time

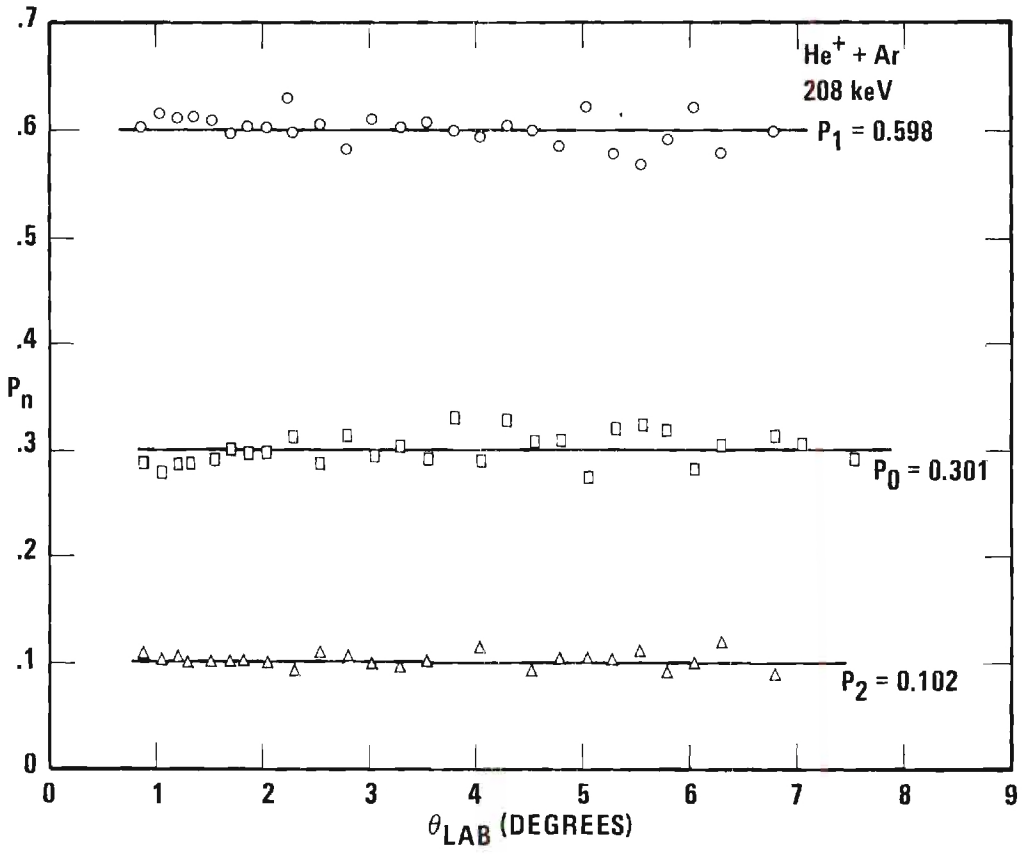

Figure 33. Fraction of Scattered Beam in Charge State n Versus Scattering Angle for He^+ + Ar with Incident Energy of 208 keV.

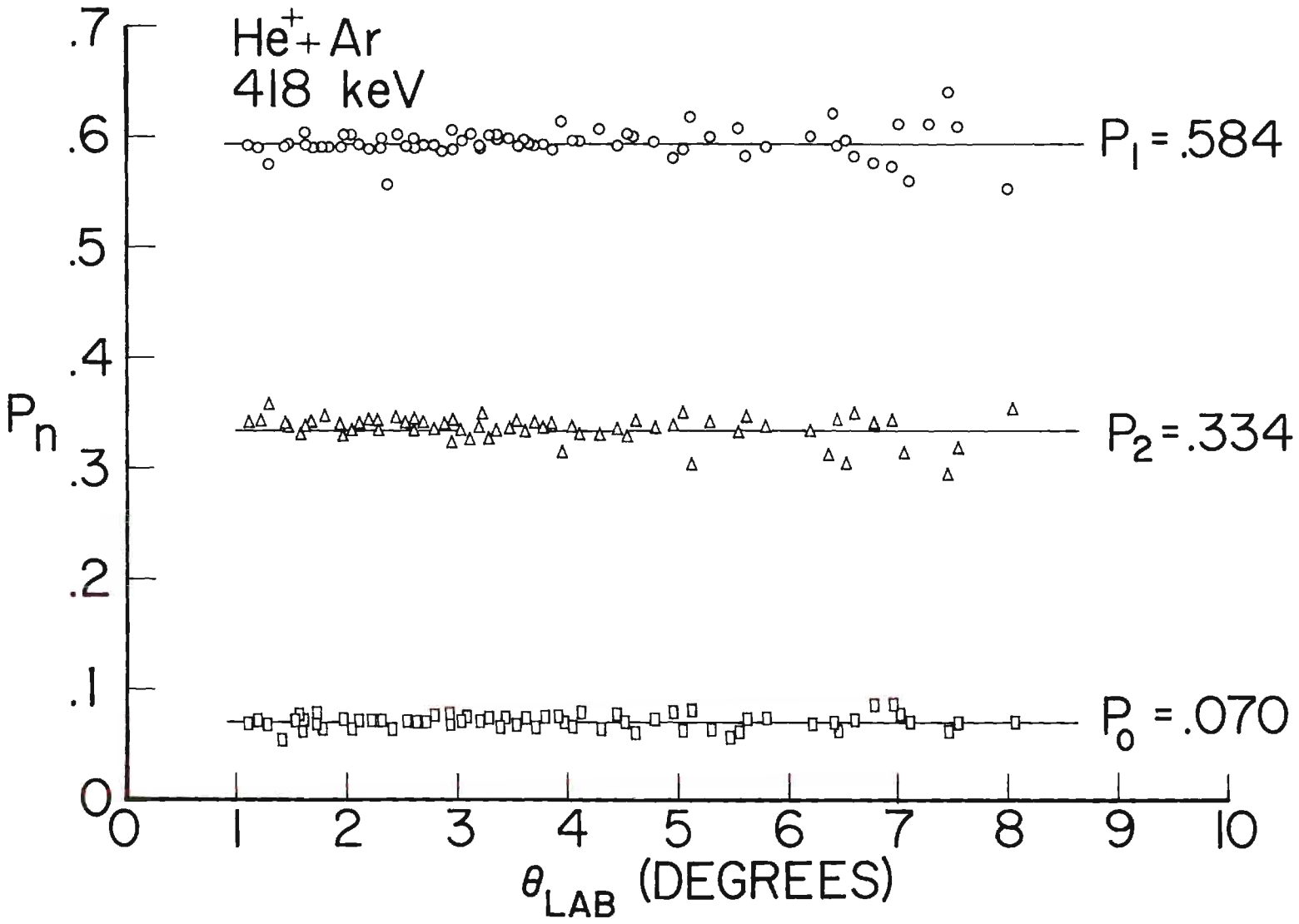

Figure 34. Fraction of Scattered Beam in Charge State n Versus Scattering Angle for He^+ + Ar with Incident Energy of 418 keV.

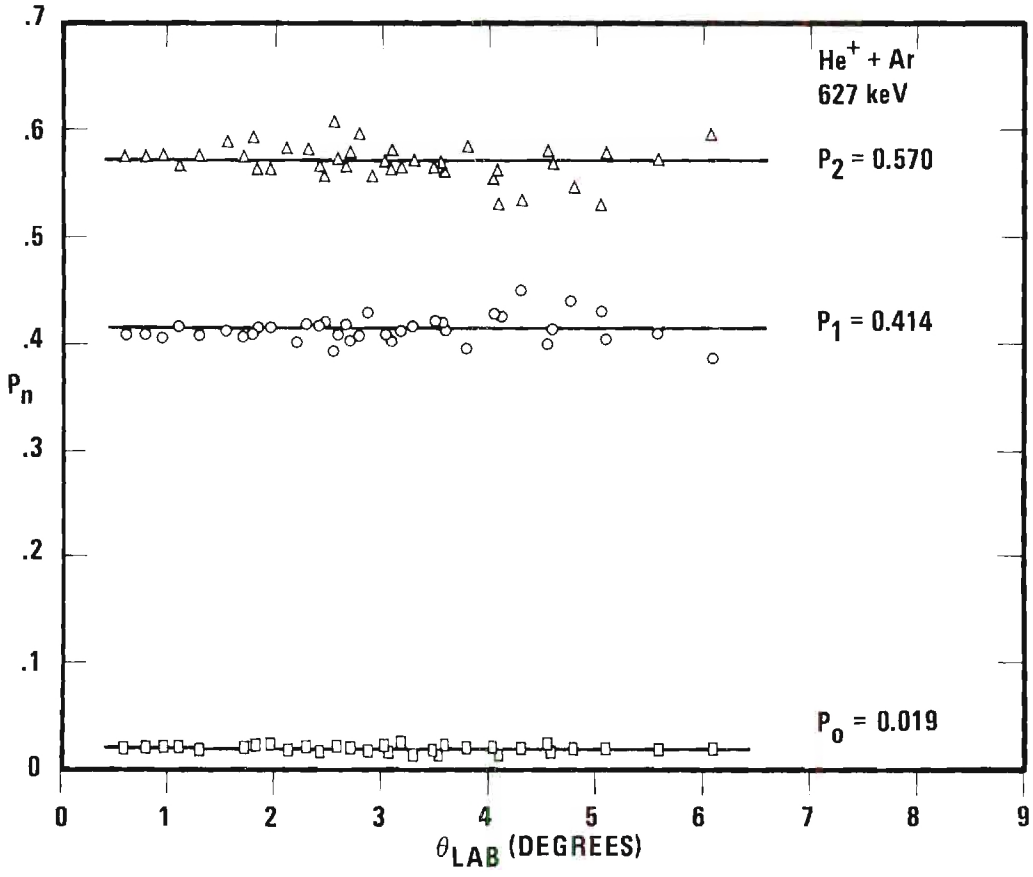

Figure 35. Fraction of Scattered Beam in Charge State n Versus Scattering Angle for He^+ + Ar with Incident Energy of 627 keV.

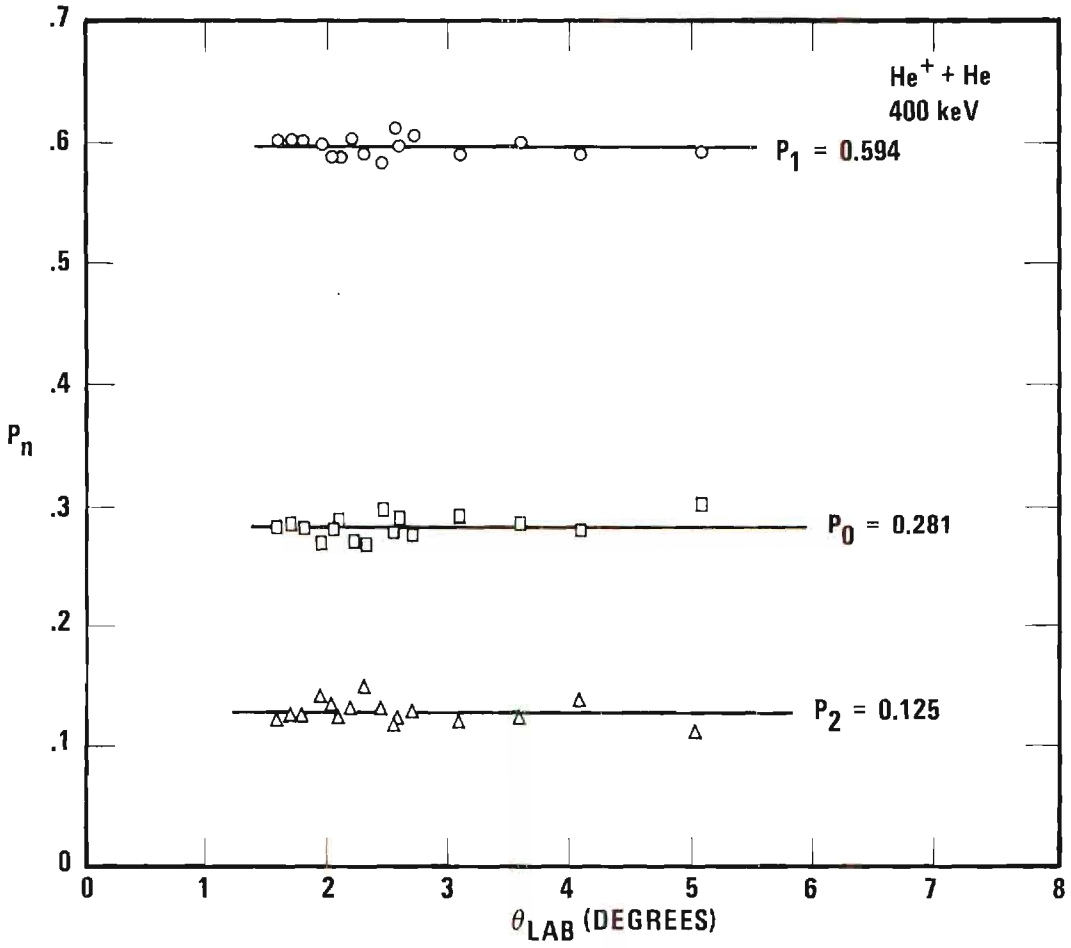

Figure 36. Fraction of Scattered Beam in Charge State n Versus Scattering Angle for He^+ + He with Incident Energy of 400 keV.

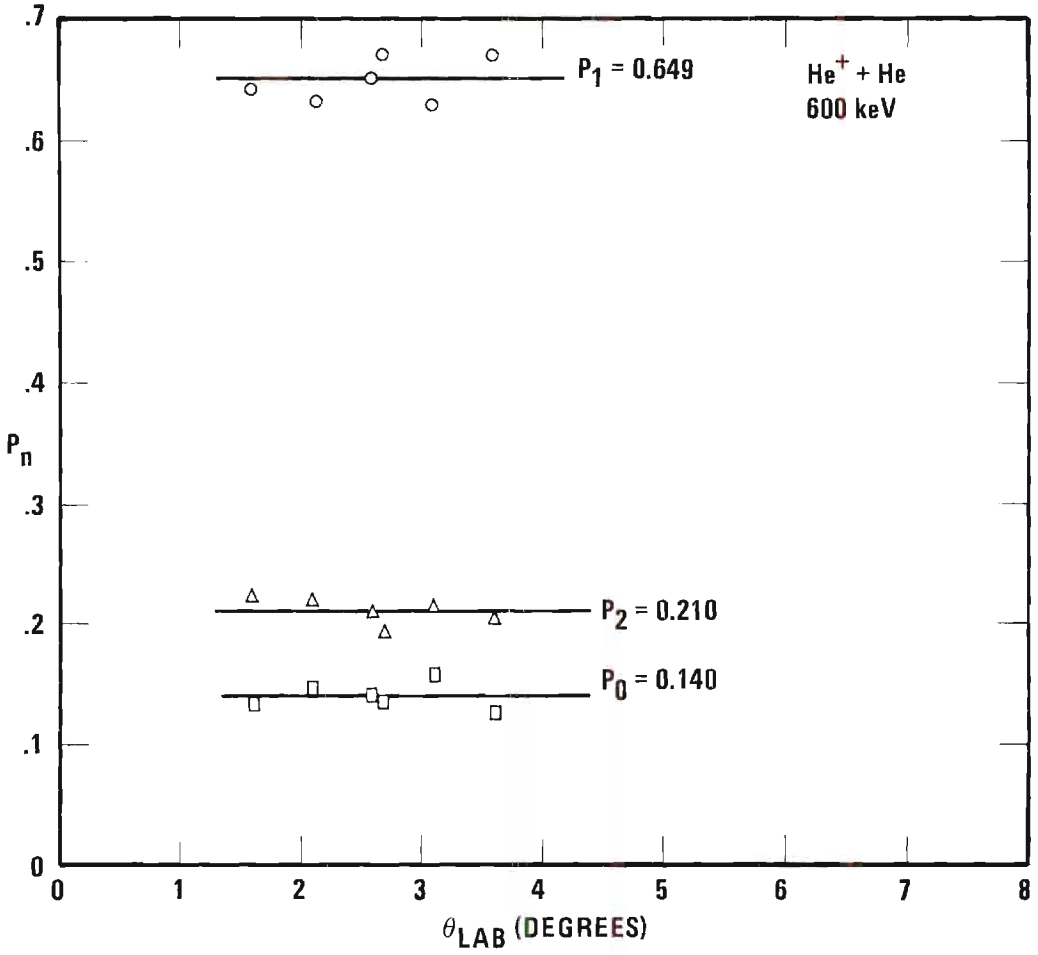

Figure 37. Fraction of Scattered Beam in Charge State n Versus Scattering Angle for He^+ + He with Incident Energy of 600 keV.

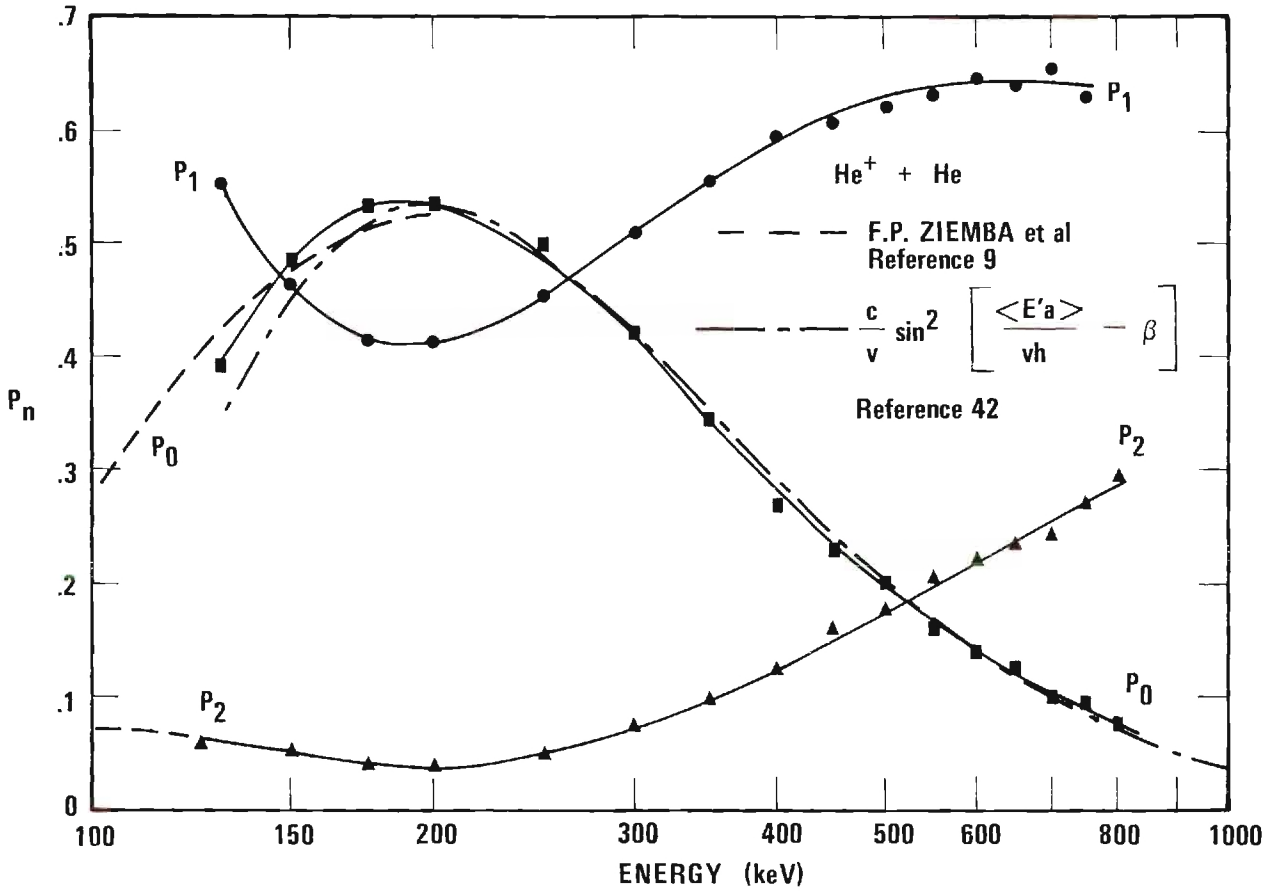

Figure 38. Fraction of Scattered Beam in Charge State n Versus Energy for $He^+ + He$.

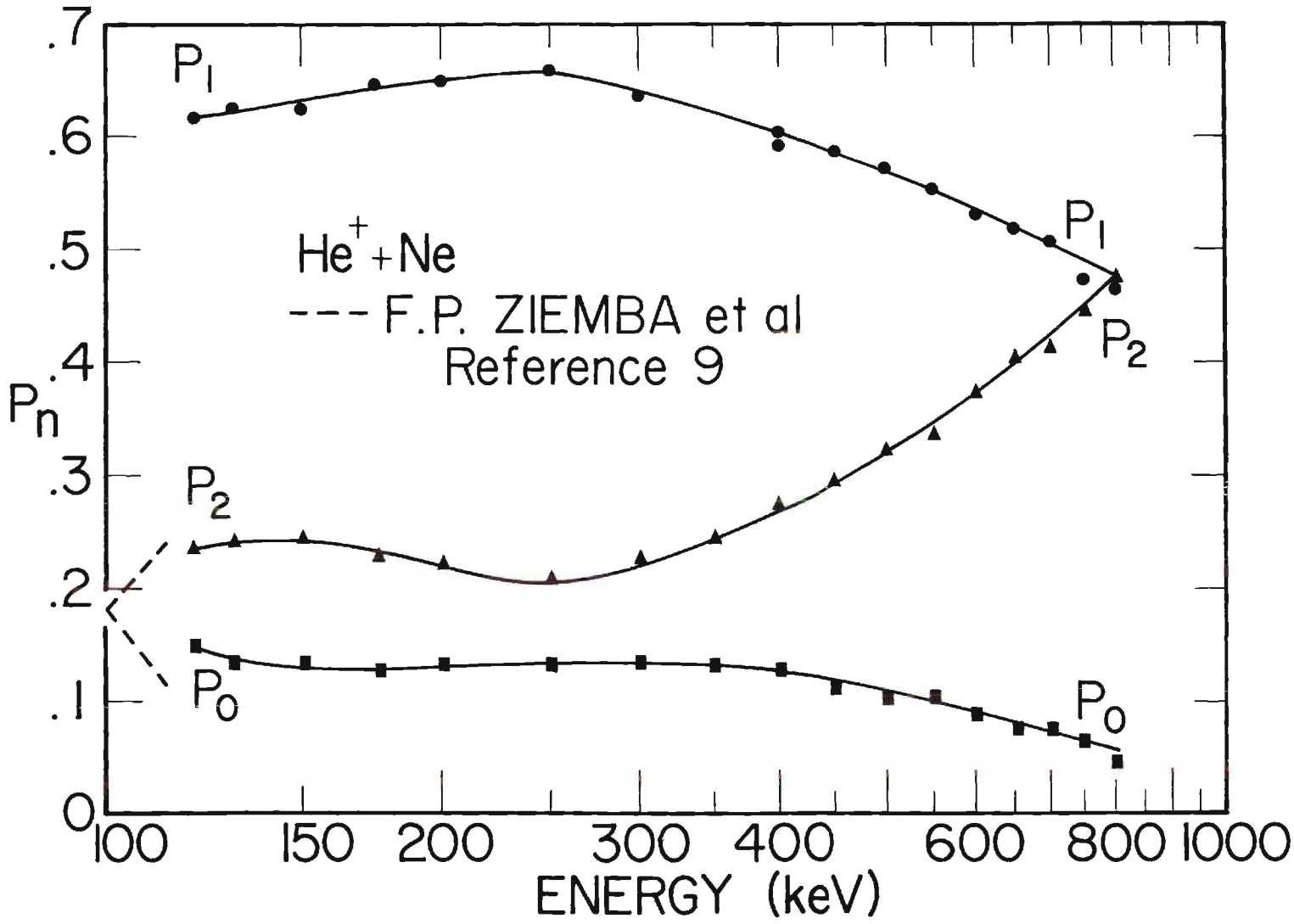

Figure 39. Fraction of Scattered Beam in Charge State n Versus Energy for He^+ + Ne.

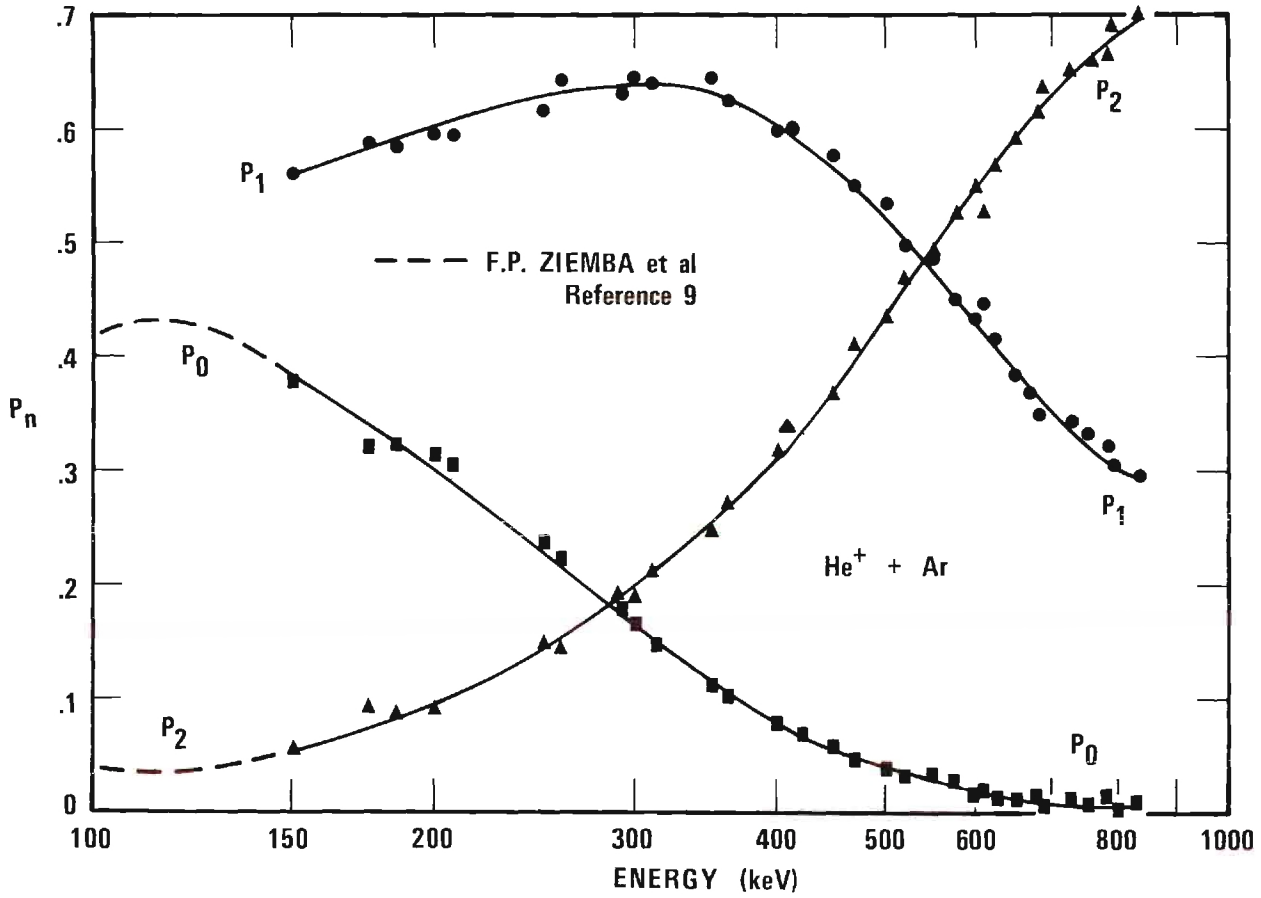

Figure 40. Fraction of Scattered Beam in Charge State n Versus Energy for He^+ + Ar.

Table 6. Energy Dependence of P_n for $He^+ + He$

E	P_0	P_1	P_2
130	0.391	0.551	0.059
150	0.488	0.464	0.049
175	0.537	0.421	0.042
200	0.538	0.420	0.041
250	0.502	0.455	0.053
300	0.412	0.515	0.073
350	0.345	0.559	0.095
400	0.281	0.594	0.125
450	0.232	0.607	0.162
500	0.202	0.621	0.181
550	0.164	0.631	0.204
600	0.140	0.649	0.212
650	0.128	0.637	0.235
700	0.101	0.654	0.245
750	0.098	0.633	0.270
800	0.076	0.633	0.293

Table 7. Energy Dependence of P_n for He^+ + Ne

E	P_0	P_1	P_2
120	0.148	0.600	0.250
130	0.134	0.627	0.240
150	0.131	0.624	0.244
175	0.127	0.647	0.226
200	0.133	0.650	0.217
250	0.132	0.659	0.208
300	0.134	0.639	0.228
350	0.131	0.620	0.248
400	0.126	0.601	0.275
450	0.110	0.589	0.297
500	0.101	0.575	0.322
550	0.105	0.557	0.338
600	0.088	0.536	0.374
650	0.078	0.519	0.404
700	0.075	0.508	0.416
750	0.066	0.478	0.449
800	0.043	0.464	0.474

Table 8. Energy Dependence of P_n for He^+ + Ar

E	P_0	P_1	P_2
158	0.375	0.560	0.055
187	0.332	0.584	0.085
208	0.306	0.594	0.100
261	0.218	0.640	0.142
292	0.180	0.630	0.190
313	0.149	0.639	0.216
351	0.112	0.639	0.346
365	0.102	0.626	0.272
400	0.082	0.600	0.317
418	0.069	0.605	0.326
450	0.060	0.575	0.365
470	0.045	0.549	0.407
501	0.040	0.530	0.432
522	0.034	0.498	0.468
551	0.030	0.483	0.487
603	0.023	0.448	0.527
653	0.016	0.383	0.593
685	0.015	0.360	0.625
734	0.010	0.342	0.648
759	0.009	0.331	0.658
781	0.013	0.321	0.665
793	0.007	0.304	0.689
830	0.008	0.295	0.697

keeping the counting rate within the limitations of the electronics. The scattering angles were varied from one and one-half degrees to three degrees while taking these data; the smaller angles were used primarily when He was the target. Some individual runs were made over the entire energy span at a single fixed angle, but these runs were weighted equally with data at other angles.

Measurements[9,41] have been reported of the energy dependence of P_n for He^+ ions incident on He from one to 200 keV, He^+ ions incident on Ne and Ar from 10 to 200 keV.[9] These data are shown by dashed lines on Figures 38, 39, and 40. There is excellent agreement between the two sets of data in all cases. Taken together, these two sets of data furnish the energy dependence of P_n over an extremely wide energy range.

For the resonant case, $He^+ + He$, Everhart predicted[87] that the last peak in the oscillation of P_o would occur at 250 keV. His data, which stop at 200 keV, seem to support the supposition; however, the present data indicate the peak in P_o to occur at approximately 190 keV. The present data and Everhart's data do not disagree outside their stated errors, although he shows a slightly different curve of best fit through his data.

The dashed line in Figure 38 shows the semi-empirical equation

$$P_o = K_o\left(\frac{1}{v}\right) + K_2\left(\frac{1}{v}\right) \sin^2 \left[\frac{\pi \langle E'a \rangle}{vh} - \beta\right]. \qquad (39)$$

K_1 and K_2 are slowly varying functions of reciprocal velocity. This equation correctly reproduces the data of Everhart.[42] For $He^+ + He$, Everhart[42] lists $\langle E'a \rangle = 102 \pm 3$ eV-Å, $\beta = (0.23 \pm 0.08)\pi$, $K_o = 0$ and $K_2 = 1$.

It has been found that this equation agrees extremely well with the present experimental data from 150 keV to 1000 keV if the same values of $\langle E'a \rangle$ and β are used, but with $K_1 = 0$ and $K_2 = 1.729 \times 10^8/v$, v being the projectile velocity in cm/sec. The curve of this equation is shown on Figure 38.

One last comparison to be made with the present data is with Russek's statistical theory.[18,19] As discussed in Chapter II, this theory was initially designed to describe heavy particle interaction and was then extended to consider interactions involving helium projectiles. This theory predicts the ordinates for the peak of each P_n curve (except P_0), and the ordinate for each $P_n \times P_m$ crossing. These predictions are presented in the form of a graph, the abscissa of the graph being a function that is indirectly relatable to the impact energy. The comparison between theory and experiment is shown in Table 9. As can be seen from examining this table, the $P_0 \times P_1$ and $P_1 \times P_2$ crossings are predicted remarkably closely; however, the prediction for the $P_0 \times P_2$ crossing and the P_1 peak are not as close.

Two values listed in the table (P_0 in Ar and $P_0 \times P_2$ in Ne) were not measured in the present experiment, but these values have been experimentally determined elsewhere[9] and are listed for comparative purposes.

Table 9. Heights of Intersections and Peaks of P_n Compared with Statistical Theory

	Target Gas			Theory[19]
	He	Ne	Ar	
P_0	0.54	-----	0.43*	----
$P_0 \times P_1$	0.46-0.47	-----	-----	0.48
$P_0 \times P_2$	0.18	0.18*	0.18	0.00
P_1	0.64	0.66	0.64	1.00
$P_1 \times P_2$	----	0.47	0.48	0.52
P_2	----	-----	-----	----

*These values taken from other experimental work.[9]

CHAPTER VI

CONCLUSIONS

The total differential scattering cross section, the differential scattering cross sections for electron capture, for electron stripping, and for scattering without change of charge have been measured for fast He^+ ions incident on the noble gases helium, neon, and argon. These cross sections were measured at several specific energies in the angular range from approximately one to eight degrees.

At each specific energy, the total differential scattering cross section (which was equal to the sum of the differential scattering cross sections for electron capture, for electron stripping, and for scattering without change of charge) agreed, within experimental errors, with the theoretically predicted cross section. The scattering is correctly predicted by classical theory where the interaction potential between the nuclei is a screened Coulomb function. The electronic screening is introduced to the Coulomb potential by an exponential factor (e^{-r/c_B}) where c_B is the screening length originally suggested by Bohr.[13] This agreement strongly supports the approximation of separating the nuclear motion from the final electronic configuration. Also, this agreement between the data and the classical scattering theory confirms Smith's suggestion of considering such high energy collisions as "quasielastic." It was not possible to distinguish elastic from inelastic collisions in this work; however, it was possible to estimate an upper limit on the

inelastic energy loss to be less than 15 percent of the incident energy. Measurements in other laboratories[11,12] indicate that actually the inelastic energy loss is less than 0.01.

The estimated error in the total differential scattering cross section is ± 23 percent. Of this total possible error, ± 13 percent is considered systematic. The differential scattering cross sections for electron capture and for electron stripping have a possible random error of approximately ± 15 percent. The random error is dependent on the energy, scattering angle, and target gas.

It is estimated that any structure in the total differential scattering cross section which might exist within the investigated energy and angular region deviates less than 12 percent from the smoothly varying cross section curve. Such structure has been reported for the same projectile-target combinations in elastic collisions at low energies[2,3]; also, it has been reported for noble gas ion-atom collisions[21] at 25 and 50 keV.

The present investigation also measured the fraction of the charge states of the projectile as a function of both angle and energy. It was found that these fractions were independent of angle within the investigated region, a conclusion which is supported both by other experiments[8] and by theory.[43]

The energy dependence of these fractions was measured at fixed angle from approximately 150 to 830 keV. In the target gases Ne and Ar, He^{2+} became the dominant charge state at the higher energies. For the He target, He^{2+} was increasing at the highest energy of the present measurement, but He^{+} was still the largest charge state component of the

scattered beam. In the range 150 to 200 keV, the present measurements agree with the work of Ziemba, et al.[9] which covers the energy region from approximately 200 keV down to 10 keV.

For the case of He^+ + He, the probability of electron transfer has previously been represented at energies below 200 keV by the semi-empirical equation[42]

$$P_o = K_o\left(\frac{1}{v}\right) + K_2\left(\frac{1}{v}\right) \sin^2 \left[\frac{\pi \langle E'a \rangle}{vh} - \beta\right] \qquad (39)$$

where $K_o = 0$ and $K_2 = 1$. $\langle E'a \rangle$ and β were determined from experimental data.[42] It was found that this expression could also describe P_o in the energy region 150 to 1000 keV if K_2 was set equal to $1.729 \times 10^8/v$ where v is the projectile velocity in cm per second.

As the projectile energy approaches one MeV, the cross sections for charge changing should be adequately described by the Born approximation. However, differential scattering cross sections for charge changing collisions have not been published for the high energy case; therefore, it is not possible at present to make these comparisons.

APPENDIX A

GEOMETRICAL FACTOR IN SCATTERING EXPERIMENT

The differential scattering cross section is given by equation (15). Before evaluating this equation, it is first necessary to calculate the geometrical factor, $G(\theta)$. As shown in Chapter II, $G(\theta)$ is the integral $\int_L \omega dx$. This integral represents the product of the average solid angle defined by the detection system and the length of beam path viewed by this solid angle. In evaluating this integral the treatment of Skalskaya[88] will be followed.

Consider a narrow parallel beam of projectiles passing through the target gas. The beam will define the x coordinate axis. Two rectangular apertures whose line of centers make an angle θ with the beam axis define the scattered projectiles which will reach the detector (see Figure 41). The origin of x is taken at the point on the beam line where it is intersected by the line of centers of the scattered-particle apertures. Second order effects, such as the finite dimensions of the beam, are ignored for the present; however, later a generalization to finite beam dimensions is made in this appendix.

The first aperture (S_1) had a width (a) and is a distance (ℓ) from the origin. The second aperture (S_2) has a width (b), a height (h), and is a distance (d) behind the first aperture. The height of this first aperture is greater than the beam diameter; only the height of the second aperture limits particles from reaching the detector. ω is the

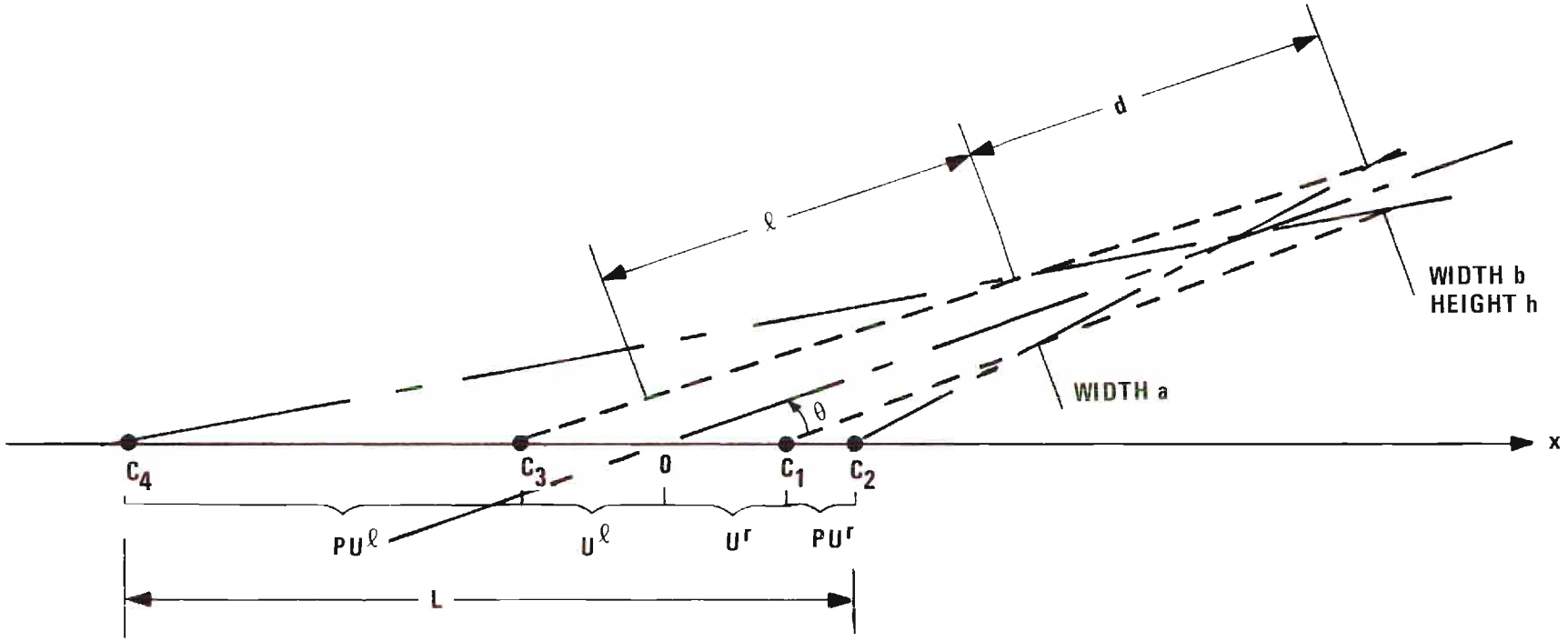

Figure 41. Umbra and Penumbra Regions in Scattering.

solid angle subtended by the bundle of all rays, from a given point (x) on the beam path, which pass through both apertures. The total length of beam path that may contribute to the scattered signal is (L), the distance from point c_4 to point c_2, in Figure 41. The points c_1 and c_3 divide the "umbra" region, in which all points of the beam can "see" the full width of aperture S_2, from the "penumbra" region in which part of the width of aperture S_2 is occluded by the edge of aperture S_1.

To simplify the calculation, divide L into four regions; the umbra and penumbra to the right of the origin, the umbra and penumbra to the left of the origin. Considering first the umbra region to the right of the origin (region U^r),

$$\omega_1(x) = \frac{b\ h}{(d + \ell - x \cos\theta)^2} \tag{43}$$

where

$$(0 \leqq x \leqq c_1) \ .$$

Using only the point-slope formula from analytical geometry, it can be shown that

$$c_1 = \frac{ad + \ell(a-b)}{2d \sin\theta + (a-b) \cos\theta} \ . \tag{44}$$

The solid angle for the penumbra regions is more difficult to compute since the aperture S_1 partially occludes aperture S_2. In the penumbra to the right of the origin (region PU^r)

$$\omega_2(x) = \left\{\frac{(a+b)\ \ell + ad - [(a+b)\cos\theta + 2d\sin\theta]\ x}{[d+\ell - x\cos\theta]^2\ (\ell - x\cos\theta)}\right\}\frac{h}{2} \qquad (45)$$

where

$$(c_1 \leqq x \leqq c_2)$$

and

$$c_2 = \frac{ad + \ell(a+b)}{2d\sin\theta + (a+b)\cos\theta} \ . \qquad (46)$$

c_2 represents the limiting point to the right of the origin from which a particle may pass through both collimators.

For the region U^{ℓ} (umbra left of origin)

$$\omega_3(x) = \frac{b\ h}{(d+\ell - x\cos\theta)^2} \qquad (47)$$

where

$$(c_3 \leqq x \leqq 0) \ .$$

Carefully observe that x is negative in this region, and

$$c_3 = -\frac{ad + \ell(a-b)}{2d\sin\theta - (a-b)\cos\theta} \ . \qquad (48)$$

In the region PU^{ℓ} (penumbra left);

$$\omega_4(x) = \left\{\frac{ad + (a+b)\ \ell + \{2d\sin\theta - (a+b)\cos\theta\}\ x}{[d+\ell - x\cos\theta]^2\ (\ell - x\cos\theta)}\right\}\frac{h}{2} \qquad (49)$$

where

$$(c_4 \leqq x \leqq c_3) \ .$$

$$c_4 = - \frac{ad + (a+b)\ \ell}{2d \sin\theta - (a+b) \cos\theta} \cdot \tag{50}$$

c_4 is the limiting point to the left of the origin from which a particle may pass through both collimators.

The total path length which will contribute to the integral will be $c_2 - c_4$ or

$$L = \frac{4d \sin\theta\ [ad + \ell(a+b)]}{(2d \sin\theta)^2 - (a+b)^2 \cos^2\theta} \cdot \tag{51}$$

The integration to be performed resolves itself into four integrals.

$$\int_L w(x)dx = \int_o^{c_1} w_1(x)dx + \int_{c_3}^{o} w_3(x)dx + \int_{c_1}^{c_2} w_2(x)dx + \int_{c_4}^{c_3} w_4(x)dx \tag{52}$$

The first two integrals represent the umbra region, the last two the penumbra. These integrations are straightforward, though lengthy.

The integral for the umbra region gives

$$\int_o^{c_1} w_1(x)dx + \int_{c_3}^{o} w_3(x)dx = \frac{bh}{d + \ell} \left\{ \frac{c_1}{d+\ell - c_1 \cos\theta} - \frac{c_3}{d+\ell - c_3 \cos\theta} \right\}. \tag{53}$$

For penumbra right,

$$\int_{c_1}^{c_2} w_2(x)dx = \frac{h}{2} [2(d+\ell) \tan\theta + b] \left\{ \frac{c_2 - c_1}{(d+\ell - c_2 \cos\theta)(d+\ell - c_1 \cos\theta)} \right\}$$

$$+ \frac{h[2\ell \tan\theta - a]}{2d \cos\theta} \ln \frac{\ell - c_2 \cos\theta}{\ell - c_1 \cos\theta} \cdot \frac{d+\ell - c_1 \cos\theta}{d+\ell - c_2 \cos\theta} \cdot \tag{54}$$

And for penumbra left

$$\int_{c_4}^{c_3} \omega_4(x)dx = + \frac{h}{2}\,[2(d+\ell)\,\tan\theta + b]\left\{\frac{c_4 - c_3}{(d+\ell - c_3\cos\theta)(d+\ell - c_4\cos\theta)}\right\}$$

$$+ \frac{h[2\ell\,\tan\theta - a]}{2d\cos\theta}\,\ln\frac{\ell - c_4\cos\theta}{\ell - c_3\cos\theta}\cdot\frac{d+\ell - c_3\cos\theta}{d+\ell - c_4\cos\theta}\,. \qquad (55)$$

Thus, the complete analytical expression for the geometrical factor is:

$$\int_L \omega(x)dx = \frac{bh}{d+\ell}\left\{\frac{c_1}{d+\ell - c_1\cos\theta} - \frac{c_3}{d+\ell - c_3\cos\theta}\right\}$$

$$+ \frac{h[2(d+\ell)\,\tan\theta + b]\,[c_2 - c_1]}{2[d+\ell - c_2\cos\theta]\,[d+\ell - c_1\cos\theta]}$$

$$+ \frac{h[2(d+\ell)\,\tan\theta + b]\,[c_4 - c_3]}{2[d+\ell - c_3\cos\theta]\,[d+\ell - c_4\cos\theta]}$$

$$+ \frac{h[2\ell\,\tan\theta - a]}{2d\cos\theta}\,\ln\frac{\ell - c_2\cos\theta}{\ell - c_1\cos\theta}\cdot\frac{d+\ell - c_1\cos\theta}{d+\ell - c_2\cos\theta}$$

$$+ \frac{h[2\ell\,\tan\theta + a]}{2d\cos\theta}\,\ln\frac{\ell - c_4\cos\theta}{\ell - c_3\cos\theta}\cdot\frac{d+\ell - c_3\cos\theta}{d+\ell - c_4\cos\theta}\,. \qquad (56)$$

This relation is very similar to the expression derived by Fillippenko,[23] which seems to contain certain errors.

This equation can be greatly simplified by substituting the expressions for the four c's; i.e., equations (44), (46), (48), and (50) into equation (56). When this is done, the first three terms exactly cancel. Also, the two ln terms may be combined giving,

$$\int_L \omega(x)dx = \frac{ah}{d\cos\theta}\,\ln\frac{2(d+\ell)\,\sin\theta + b\cos\theta}{2(d+\ell)\,\sin\theta - b\cos\theta}\,. \qquad (57)$$

This equation is identical to the expression derived by Skalskaya.[88] Upon expanding the ln term, one obtains

$$\int_L \omega(x)dx = \frac{ah}{d\cos\theta}\left\{2\zeta + \frac{2}{3}\zeta^3 + \ldots\right\} \qquad (58)$$

where

$$\zeta = \frac{b\cos\theta}{2(d+\ell)\sin\theta} \cdot$$

Keeping only the first term,

$$\int_L \omega dx \simeq \frac{abh}{d(d+\ell)}\frac{1}{\sin\theta} \cdot \qquad (59)$$

This is the Jordan-Brode equation.[89] It has been employed by all investigators measuring absolute differential scattering cross sections.[37,52,53]

Ignoring the higher order terms requires that

$$b^3\cos^3\theta \ll 12\,(d+\ell)^3\sin^3\theta \cdot$$

In this experiment this condition would be well satisfied down to angles less than 30 minutes. For example, with θ = 30 minutes, b = 0.0091 inch, and d = 5.65 inches; the inequality requires that $7.5 \times 10^{-4} \ll 1.4$.

Beam Thickness

In Chapter II it is shown that, in evaluating the differential scattering cross section $\frac{d\sigma}{d\omega}$, one actually needs to evaluate the integral $\int\omega dAdx$, where dA is a differential cross sectional area of the beam. The integral $\int\omega dx$ has been evaluated. Now we shall show that $A\int\omega dx$ is a very

good approximation for $\int \omega dA dx$, for the geometry of the present experiment.

We shall assume that the cross sectional area of the beam is square. This is a "worst case" approximation; the beam is actually circular in cross section in the present experiment. Let the scattering plane be the x - z plane. For a given x, the distance to the first aperture S_1 from points in the beam volume is much more dependent on the width z of the beam in the scattering plane than on its height y perpendicular to that plane. Hence, we need to consider only the two-dimensional "volume" of the beam, or its area in the scattering plane.

Let the origin be at the center with the beam extending to $\pm \eta/2$ along both the y and z axes, Figure 42.

$$\int \omega dA dx = \int_{-\eta/2}^{\eta/2} dy \int_{-\eta/2}^{\eta/2} dz \int_L \omega dx$$

The x integration proceeds exactly as in the development leading to equation (59) except that everywhere we must replace ℓ by $\ell - z/\sin\theta$. The result is

$$\int \omega dx \simeq \frac{abh}{d\left(d+\ell - \frac{z}{\sin\theta}\right)} \frac{1}{\sin\theta} \quad . \tag{60}$$

The y integration gives the factor η; performing the z integration, we get

$$\int \omega dA dx \simeq \frac{\eta abh}{d} \ln \frac{d+\ell + \frac{\eta}{2\sin\theta}}{d+\ell - \frac{\eta}{2\sin\theta}}$$

$$\simeq \frac{\eta abh}{d} \left(2\zeta + \tfrac{2}{3}\zeta^3 + \ldots\right) . \tag{61}$$

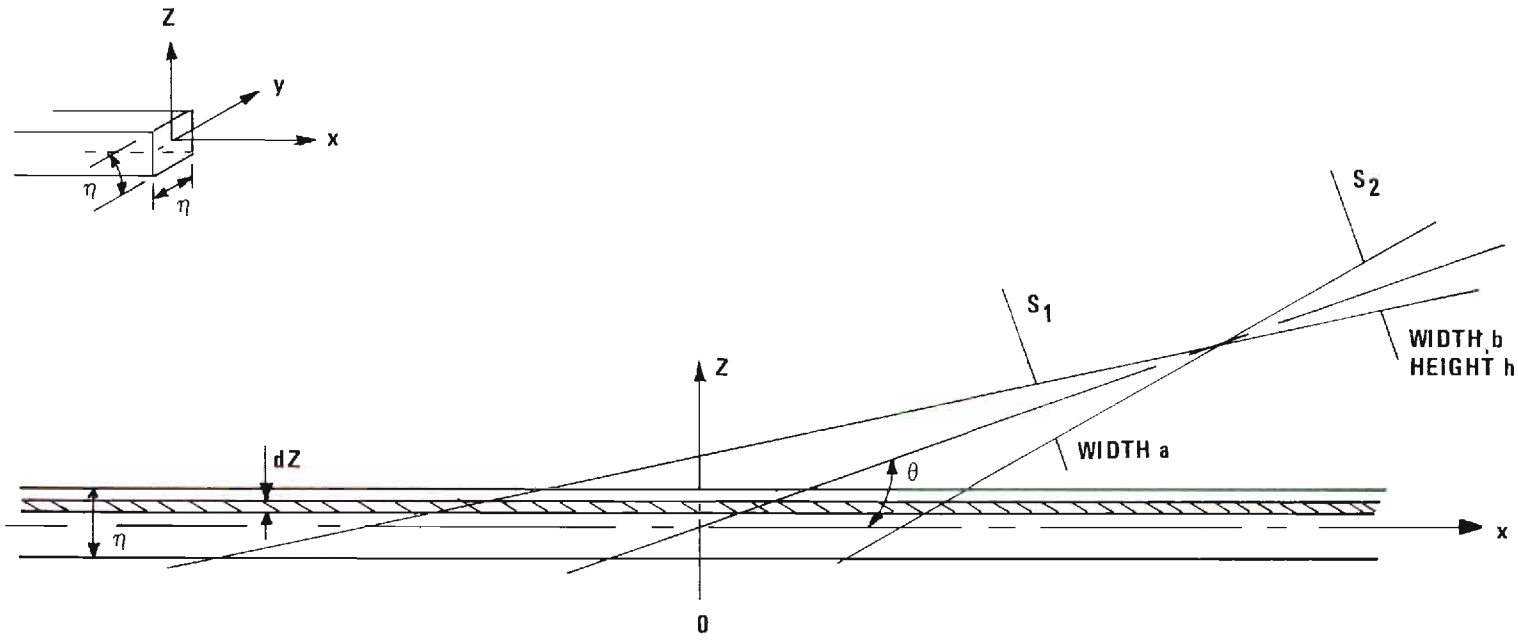

Figure 42. Finite Dimensions of Incident Beam.

where

$$\zeta = \frac{\eta}{2(d+\ell)\ \sin\ \theta} \ .$$

Keeping only the first term in the expansion

$$\int \omega dA dx \simeq \left(\frac{abh}{d(d+\ell)}\ \frac{1}{\sin\ \theta}\right) A \qquad (62)$$

where

$$A = \eta^2 \ .$$

In dropping the higher order terms, one requires that

$$\eta^3 \ll 12(d+\ell)^3\ \sin^3\ \theta \ . \qquad (63)$$

This approximation is certainly satisfied in the present experiment down to angles less than 30 minutes. The error introduced by ignoring the height of the beam is even less than this. Therefore, the finite size of the beam will not affect the present measurements.

APPENDIX B

CALIBRATION OF THE CAPACITANCE MANOMETER

The capacitance manometer was calibrated at the factory before shipment, but that calibration was at much higher gas pressures than those used in the present experiment. Since the measurement of the target gas pressure is the primary measure of the target density and the cross sections which were measured were inversely proportional to the target density, it was necessary to calibrate the capacitance manometer against a reference standard in the gas pressure range in which the present measurements were made, before the accuracy of the experimentally determined absolute differential scattering cross sections could be known.

The capacitance manometer was calibrated at Oak Ridge National Laboratory against two McLeod gauges. The gauge constants were

$$c_1 = 1.022 \times 10^{-7} \text{ Torr/mm}^2$$

$$c_2 = 2.473 \times 10^{-6} \text{ Torr/mm}^2$$

(Actually, a third gauge was also used, but its readings were consistently above the other two McLeod gauges by 13 percent; therefore, it was not used for the calibration.)

One of the McLeod gauges was refrigerated (gauge 1). This was done to reduce the streaming of mercury vapor from the McLeod gauge reservoir through connecting tubulation to cold traps in the system.[66] (This effect produces a pressure difference between the gauge and the rest of

the system, which is known as the Gaede effect.) The gas used during the calibration was hydrogen, this choice also being made to reduce the Gaede effect.

During the calibration, the refrigerated McLeod gauge was at the temperature T = 266°K, the second McLeod gauge was at room temperature, the same as the sample gas (T = 302°K), while the capacitance manometer operated at an elevated temperature (T = 324°K). (The capacitance manometer normally operates at this elevated temperature. The operating temperature of this device affects its calibration, and an elevated temperature can quite readily be stabilized by means of electrical heaters and a thermostat.) These different temperatures in various parts of the system cause different pressures to exist within the system. A correction for this effect (thermal transpiration effect) is given by[90]

$$\frac{P_1}{P_2} = \sqrt{\frac{T_1}{T_2}} \quad . \tag{64}$$

This correction increases the pressures measured by the refrigerated McLeod gauge by six percent, while the correction decreases the pressure measured with the capacitance manometer by two and one-half percent. With this correction for thermal transpiration applied to both the refrigerated McLeod gauge and the capacitance manometer, the calibration is shown in Figure 43.

This calibration covered the range from 7.5×10^{-5} Torr to 9.2×10^{-3} Torr, thus including approximately an order of magnitude on either side of the pressure range used in the cross section measurements. Below approximately one micron (10^{-3} Torr), the capacitance manometer

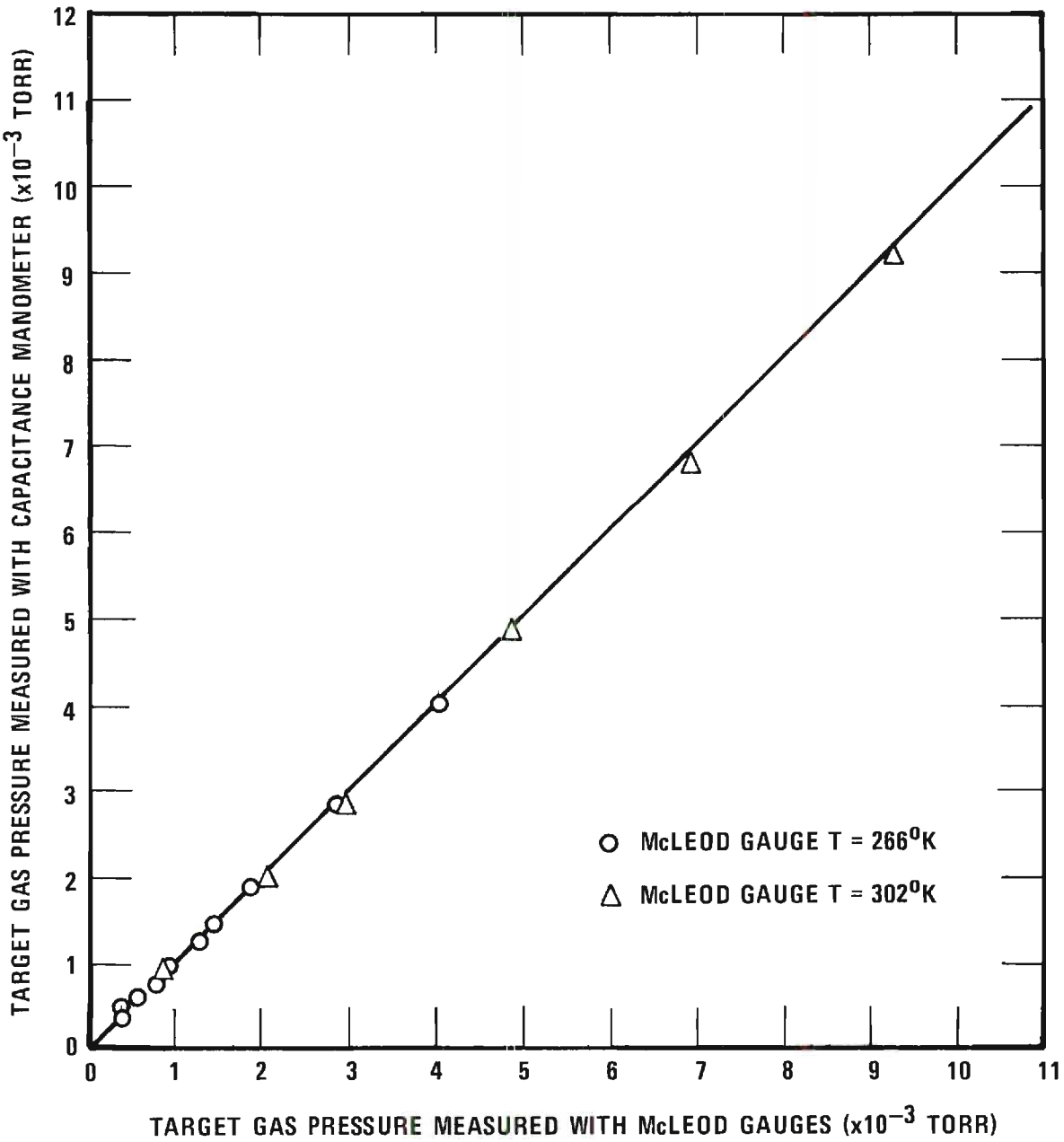

Figure 43. Calibration of Capacitance Manometer.

reading was higher than the McLeod gauge reading by approximately six percent; above one micron the two agreed to within one percent (see Figure 43).

The random error in reading the McLeod gauges was estimated to be plus or minus four percent. Many sources exist for possible systematic errors when using a McLeod gauge. The use of a refrigerated gauge and the choice of the sample gas were attempts to minimize systematic errors. The uncertainty in the gauge constants could introduce a systematic error. The accuracy of these constants was unknown; however, from the stated number of significant figures, it was estimated that the systematic error from this source would be less than one percent. It is therefore estimated that the possible systematic error in using these McLeod gauges was less than plus or minus one percent.

The possible random error in reading the capacitance manometer was estimated to be plus or minus two percent; possible systematic errors are estimated to be very small, less than 0.5 percent.

Therefore, the results from this calibration were that the capacitance manometer measures the absolute gas pressure through the pressure region used in the present experiment within plus or minus four percent. Scale reading errors are estimated to be plus or minus two percent, systematic errors are estimated to be plus or minus one percent.

BIBLIOGRAPHY*

1. F. T. Smith, Atomic Physics Proceedings of the First International Conference on Atomic Physics, June 3-7, 1968 (Plenum Press, New York, 1969), p. 353.

2. D. C. Lorents and W. Aberth, Phys. Rev. 139, A1017 (1965).

3. W. Aberth and D. C. Lorents, Phys. Rev. 144, 109 (1966).

4. V. V. Afrosimov, Yu. S. Gordeev, M. N. Panov, and N. V. Fedorenko, Zh. Eskperim. i Teor. Fiz. Pis'ma u Redaktsiyu 2, 291 (1965) [English Transl.: Soviet Phys.--JETP Letters 2, 185 (1965)].

5. P. R. Jones, T. L. Batra, and H. A. Rauga, Phys. Rev. Letters 17, 281 (1966).

6. H. H. Fleischmann and R. A. Young, Phys. Rev. Letters 19, 941 (1967).

7. P. Hoftager and G. Claussen, Sixth International Conference of the Physics of Electronic and Atomic Collisions (M.I.T. Press, Cambridge, 1969), p. 518.

8. E. N. Fuls, P. R. Jones, F. P. Ziemba, and E. Everhart, Phys. Rev. 107, 704 (1957).

9. F. P. Ziemba, G. J. Lockwood, G. H. Morgan, and E. Everhart, Phys. Rev. 118, 1552 (1960).

10. O. B. Firsov, Zh. Eksperim. i Teor. Fiz. 34, 447 (1958)[English Transl.: Soviet Phys.--JETP 34, 308 (1958)].

11. Q. C. Kessel and E. Everhart, Phys. Rev. 146, 16 (1966).

12. Q. C. Kessel, P. H. Rose, and L. Grodzins, Phys. Rev. Letters 22, 1031 (1969).

13. N. Bohr, Kgl. Danske Videnskab.Selskab, Mat.-fys. Medd. 18, No. 8 (1948).

14. D. R. Bates and R. McCarroll, Proc. Roy. Soc. (London) A245, 175 (1958).

---

*Abbreviations used herein conform to those found in the American Institute of Physics Style Manual, 1965.

BIBLIOGRAPHY (Continued)

15. E. Everhart, Phys. Rev. 132, 2083 (1963).

16. W. Lichten, Phys. Rev. 131, 229 (1963).

17. R. P. Marchi and F. T. Smith, Phys. Rev. 139, A1025 (1965).

18. A. Russek and M. T. Thomas, Phys. Rev. 109, 2015 (1958).

19. J. B. Bulman and A. Russek, Phys. Rev. 122, 506 (1961).

20. F. T. Smith, R. P. Marchi, W. Aberth, D. C. Lorents, and O. Heinz, Phys. Rev. 161, 31 (1967).

21. V. V. Afrosimov, Yu. S. Gordeev, M. N. Panov, and N. V. Fedorenko, Zh. Techn. Fiz. 36, 123 (1966)[English Transl.: Soviet Phys.--Tech. Phys. 11, 89 (1966)].

22. E. W. Thomas, Private Communications.

23. L. G. Filippenko, Zh. Techn. Fiz. 30, 57 (1960).

24. W. B. Maier, II, LASL-3972 (1968).

25. N. F. Mott and H. S. W. Massey, The Theory of Atomic Collisions (Oxford University Press, London, 1965), third edition, Chapt. V, Sec. 5.

26. E. Everhart, G. Stone, and R. J. Carbone, Phys. Rev. 99, 1287 (1955).

27. Earl W. McDaniel, Collision Phenomena in Ionized Gases (John Wiley & Sons, Inc., New York, 1964), Sections 3-10 and 4-10.

28. L. H. Thomas, Proc. Camb. Phil. Soc. 23, 542 (1927).

29. E. Fermi, Zeits. F. Physik 48, 73 (1928).

30. L. I. Schiff, Quantum Mechanics (McGraw-Hill Book Company, Inc., New York, 1955), second edition, p. 170.

31. H. Goldstein, Classical Mechanics (Addison-Wesley, Reading, Mass., 1950), Chapt. 3.

32. E. H. S. Burhop, Quantum Theory I. Elements, edited by D. R. Bates (Academic Press, Inc., New York, 1961), Chapt. 9.

33. O. B. Firsov, Zh. Eksperim. i Teor. Fiz. 24, 279 (1953).

BIBLIOGRAPHY (Continued)

34. G. H. Lane and E. Everhart, Phys. Rev. 120, 2064 (1960).

35. F. T. Smith, R. P. Marchi, and K. G. Dedrick, Phys. Rev. 150, 79 (1966).

36. Felton W. Bingham, J. Chem. Phys. 46, 2003 (1967).

37. L. I. Pivovar, M. T. Nivikov, and V. M. Tubaev, Proceedings of the Third International Conference on the Physics of Electronic and Atomic Collisions, London 1963 (North Holand Publishing Co., Amsterdam, 1964), p. 883.

38. O. B. Firsov, Zh. Eksperim. i Teor. Fiz. 33, 696 (1957)[English Transl.: Soviet Phys.--JETP 6, 534 (1958)].

39. Albert Messiah, Quantum Mechanics (John Wiley & Sons, Inc., New York, 1962), p. 618.

40. J. Lindhard, V. Nielsen, and M. Scharff, Kgl. Danske Videnskab. Selskab, Mat.-fys. Medd. 36, No. 10 (1968).

41. G. J. Lockwood, H. F. Helbig, E. Everhart, Phys. Rev. 132, 2078 (1963).

42. G. J. Lockwood and E. Everhart, Phys. Rev. 125, 567 (1962).

43. F. P. Ziemba and A. Russek, Phys. Rev. 115, 922 (1959).

44. D. R. Bates, H. S. W. Massey, and A. L. Stewart, Proc. Roy. Soc. (London) A216, 437 (1958).

45. P. E. Phillipson, Phys. Rev. 125, 1981 (1962).

46. William Lichten, Phys. Rev. 164, 131 (1967).

47. F. T. Smith, Phys. Rev. 179, 111 (1969).

48. N. F. Mott and H. S. W. Massey, Op. cit., Chapt. XIX, Sec. 7.

49. A. Russek, Phys. Rev. 132, 246 (1963).

50. Q. C. Kessel, M. P. McCaughey, and E. Everhart, Phys. Rev. Letters 16, 1189 (1966).

51. M. E. Rudd, T. Jorgensen, Jr., and D. L. Volk, Phys. Rev. 151, 28 (1966).

52. N. V. Fedorenko, Zh. Techn. Fiz. 24, 784 (1954).

BIBLIOGRAPHY (Continued)

53. E. Everhart, R. J. Carbone, and S. Stone, Phys. Rev. 98, 1945 (1955).

54. N. V. Fedorenko, V. V. Afrosimov, and D. M. Kaminker, Zh. Techn. Fiz. 26, 1929 (1956)[English Transl.: Soviet Phys.--Tech. Phys. 1, 1861 (1957)].

55. V. V. Afrosimov, Yu. S. Gordeev, M. N. Panov, and N. V. Fedorenko, Zh. Techn. Fiz. 34, 1613 (1964)[English Transl.: Soviet Phys.--Tech. Phys. 9, 1248 (1965)].

56. L. I. Pivovar, M. T. Novikov, and V. M. Tubaev, Zh. Eksperim. i Teor. Fiz. 46, 471 (1964)[English Transl.: Soviet Phys.--JETP 19, 318 (1964)].

57. L. I. Pivovar, M. T. Novikov, and A. S. Dolgov, Zh. Eksperim. i Teor. Fiz. 49, 734 (1965)[English Transl.: Soviet Phys.--JETP 22, 508 (1966)].

58. L. I. Pivovar, M. T. Novikov, and A. S. Dolgov, Zh. Eksperim. i Teor. Fiz. 50, 537 (1966)[English Transl.: Soviet Phys.--JETP 23, 357 (1966)].

59. V. V. Afrosimov, Yu. S. Gordeev, Am. M. Polyansky, and A. P. Shergin, V International Conference on the Physics of Electronic and Atomic Collisions, Leningrad, U.S.S.R., July 17-23, 1967 (Publishing House, Nauka, 1967), p. 475.

60. A. B. Whittkower and H. B. Gilbody, Proc. Phys. Soc. (London) 90, 343 (1967).

61. H. B. Gilbody, R. Browning, and G. Levy, J. Phys. B (Proc. Phys. Soc.) 2, 230 (1968).

62. D. M. Kaminker and N. V. Fedorenko, Zh. Techn. Fiz. 25, 2239 (1955).

63. N. V. Fedorenko, L. G. Filippenko, and I. P. Flaks, Zh. Techn. Fiz. 30, 49 (1960)[English Transl.: Soviet Phys.--Tech. Phys. 30, 45 (1960)].

64. R. J. Carbone, E. N. Fuls, and E. Everhart, Phys. Rev. 102, 1524 (1956).

65. M. Ya. Amus'ya, Zh. Techn. Fiz. 36, 1409 (1966)[English Transl.: Soviet Phys.--Tech. Phys. 11, 1053 (1967)].

BIBLIOGRAPHY (Continued)

66. L. J. Puckett, Absolute Total Apparent Ionization, Electron Stripping, Electron Capture, and Partial Ionization Cross Section in the Energy Range 0.15 - 1.00 MeV, Unpublished Ph.D. Thesis, Atlanta: Georgia Institute of Technology (1966).

67. J. W. Hooper, Ionization Cross Sections for Protons Incident on Helium, Neon, Argon, Hydrogen, Nitrogen, Oxygen, and Carbon Monoxide in the Energy Range 0.15 - 1.10 MeV, Unpublished Ph.D. Thesis, Atlanta: Georgia Institute of Technology (1961).

68. R. F. Taschek, H. V. Argo, A. Hemmendinger, and G. A. Jarvis, Phys. Rev. 76, 325 (1949).

69. H. A. Bethe and E. Salpeter, Quantum Mechanics of One and Two-Electron Atoms (Academic Press, Inc., New York, 1957), p. 251.

70. W. L. Wiese, M. W. Smith, and B. W. Glennon, Atomic Transition Probabilities, Vol. I Hydrogen Through Neon, National Bureau of Standards, U. S. Department of Commerce, Distributed by: Superintendent of Documents, U. S. Government Printing Office, Wash., D.C.

71. S. T. Butler and R. M. May, Phys. Rev. 137, A10 (1968).

72. N. V. Fedorenko, V. A. Ankudinov, and R. N. Il'in, Zh. Techn. Fiz. 35, 585 (1965)[English Transl.: Soviet Phys.--Tech Phys. 10, 461 (1965)].

73. M. F. A. Harrison, D. F. Dance, K. T. Dolder, and A. C. H. Smith, Rev. Sci. Instr. 36, 1443 (1965).

74. N. G. Utterback and T. Griffith, Jr., Rev. Sci. Instr. 37, 866 (1966).

75. ORTEC Catalogue 1001, Ortec, Oak Ridge, Tennessee.

76. R. D. Evans, The Atomic Nucleus (McGraw-Hill Book Company, Inc., New York, 1955), Chapt. 26.

77. Charlotte E. Moore, A Multiplet Table of Astrophysical Interest, PB151 395, Distributed by: Clearinghouse for Federal Scientific and Technical Information, National Bureau of Standards, U. S. Department of Commerce, Springfield, Va.

78. Charlotte E. Moore, An Ultraviolet Multiplet Table, National Bureau of Standards, U. S. Department of Commerce, Distributed by: Superintendent of Documents, U. S. Government Printing Office, Washington, D. C.

BIBLIOGRAPHY (Concluded)

79. Evans, op. cit., p. 750.

80. D. W. Martin, R. A. Langley, D. S. Harmer, J. W. Hooper, and E. W. McDaniel, Phys. Rev. 136A, 185 (1964).

81. F. J. DeHeer, J. Schutten, and H. Moustafa, Physica 32, 1793 (1966).

82. S. K. Allison, Rev. Mod. Phys. 30, 1137 (1958).

83. P. R. Jones, F. P. Ziemba, H. A. Moses, E. Everhart, Phys. Rev. 113, 182 (1959).

84. B. L. Moiseiwitsch, Proc. Phys. Soc. A59, 653 (1956).

85. H. Schiff, Canad. J. Phys. 32, 393 (1954).

86. J. B. Hasted, Physics of Atomic Collisions (Butterworths, London, 1964), p. 437.

87. F. P. Ziemba and E. Everhart, Phys. Rev. Letters 2, 299 (1959).

88. I. P. Skalskaya, Zh. Techn. Fiz. 24, 1912 (1954).

89. E. B. Jordan and R. B. Brode, Phys. Rev. 43, 112 (1933).

90. Saul Dushman, Scientific Foundations of Vacuum Technique (John Wiley & Sons, Inc., New York, 1962) second edition, p. 58.

VITA

George Ormsbee Taylor, Jr. was born in Memphis, Tennessee on January 13, 1937. He is the son of Mr. and Mrs. George O. Taylor. On August 22, 1958, he was married to Alice Fay Clementson of Chattanooga, Tennessee. The couple have two children: a daughter, Martha Fay, born on February 7, 1963, and a son, Douglas Edmund, born on February 17, 1966.

Mr. Taylor attended The Baylor School in Chattanooga, Tennessee. He entered the University of Chattanooga and was graduated with the Bachelor of Science degree in engineering physics in 1958. The next two years he was a graduate student in physics at Michigan State University. In 1960 he received the degree of Master of Science in physics from Michigan State University. The school year 1960 to 1961 he was employed as an Instructor of Physics by the University of Chattanooga. The next two years saw him in service in the United States Army at the rank of Lieutenant.

In 1963 he began graduate study in physics at the Georgia Institute of Technology and was employed as a graduate teaching assistant in the School of Physics. In 1964 he began work with the high energy atomic collisions group in the School of Physics.

Mr. Taylor is a member of Sigma Pi Sigma, Sigma Xi, and the American Physical Society.